UNIVERSITY OF SOUTHAMPTON

FACULTY OF ENGINEERING AND THE ENVIRONMENT

Institute of Sound and Vibration Research

Structural vibration control using multiple synchronous sources

by

Martin Dench

Thesis for the degree of Doctor of Philosophy

May 2012

Abstract

The advantages of isolating vibrating machinery from its supporting structure are that the chances of vibration induced fatigue failure of structural components are reduced, the structure becomes more inhabitable for people due to less vibration exposure and the sound radiated by the structure into the environment is reduced. This last point is especially important for machinery operating in a marine environment because low frequency sound propagates very well underwater, and the machinery induced sound radiated from a ship or submarine is a primary detection and classification mechanism for passive sonar systems.

This thesis investigates the control of vibration from an elastic support structure upon which multiple vibrating systems are passively mounted. The excitations are assumed to occur at discrete frequencies with a finite number of harmonic components and the machines are all assumed to be supplied with power from the same electrical supply. Active vibration control may be achieved by adjusting the phase of the voltage supplied to one or more of the machines, so that a minimum value of a measurable cost function is obtained. Adjusting the phase of a machine with respect to a reference machine is known as synchrophasing and is a well established technique for controlling the sound in aircraft cabins and in ducts containing axial fans. However, the use of the technique for reducing the vibration of machinery mounted on elastic structures seems to have received very little attention in the literature and would appear to be a gap in the current knowledge. This thesis aims to address that gap by investigating theoretically and experimentally how synchrophasing can be implemented as an active structural vibration control technique.

This page is intentionally left blank

Contents

This page is intentionally left blank

List of Figures

This page is intentionally left blank

List of Tables

This page is intentionally left blank

Declaration of Authorship

I, Martin Dench

declare that the thesis entitled

Structural vibration control using multiple synchronous sources

and the work presented in the thesis are both my own, and have been generated by me as the result of my own original research. I confirm that:

- this work was done wholly or mainly while in candidature for a research degree at this University;
- where any part of this thesis has previously been submitted for a degree or any other qualification at this University or any other institution, this has been clearly stated;
- where I have consulted the published work of others, this is always clearly attributed;
- where I have quoted from the work of others, the source is always given. With the exception of such quotations, this thesis is entirely my own work;
- I have acknowledged all main sources of help;
- where the thesis is based on work done by myself jointly with others, I have made clear exactly what was done by others and what I have contributed myself;
- none of this work has been published before submission.

Signed: ……..

Date:…….

This page is intentionally left blank

Acknowledgements

I would like to thank my supervisors, Prof. Mike Brennan and Dr. Neil Ferguson for their technical guidance, valuable advice, motivation and support throughout this project. Thanks also to Prof. Steve Elliott and Prof. Brian Mace for their guidance and advice during my reviews.

Thanks to all past and present colleagues from the ISVR Dynamics group for their encouragement, for the interesting discussions and for making ISVR a fascinating and enjoyable place to conduct research.

I am grateful to colleagues in the Ministry of Defence and DSTL for the financial support and technical advice provided for this project.

Special thanks are due to Marjorie and to my parents for all their love, patience, encouragement and support. It is no exaggeration to say that without them, this thesis would not have reached completion.

This page is intentionally left blank

Definitions and abbreviations

ADC	Analogue to digital converter
AVC	Active vibration control
DAC	Digital to analogue converter
FM	Flexural mode
FRF	Frequency response function
ODS	Operational deflection shape
PA	Power amplifier
PC	Personal computer
PST	Propeller Signature Theory
PVDF	Polyvinylidene fluoride
RBM	Rigid body mode
RPM	Revolutions per minute
SCA	Signal conditioning amplifier

This page is intentionally left blank

1 Introduction

1.1 Background

There are many reasons why it might be desirable to reduce the transmission of vibration from vibrating sources to the surrounding structure. Excessive vibration may accelerate fatigue failure of the machinery or of the host structure itself. Reducing the vibration levels might make the structure more inhabitable for persons or equipment and may reduce the sound radiated by the structure into the environment. This last point is especially important in a marine environment, because low frequency sound propagates very well underwater and the machinery induced sound radiated from a ship or submarine is a primary detection and classification mechanism for passive sonar systems.

The traditional approach to reducing the transmission of discrete frequency vibration from vibrating sources such as rotating and reciprocating machinery, has been to decouple the machinery from the structure by using passive isolation mounts. Machinery plants on mobile platforms such as ships traditionally employ two-stage passive isolation. For the first stage, several machines are mounted, using compliant isolators, onto a large elastic support structure or raft. Secondly, the flexible raft is further decoupled from the hull structure by passive isolation mounts. These mounts are essentially damped springs and may not be effective at all frequencies at which vibrations are occurring. Passive isolation mounts have two opposing constraints. Firstly, the mount must have sufficient stiffness to support the static load of the machine. Secondly, the mounts must have low enough dynamic stiffness such that the resonance frequency of the machine on its mounts is well below the operating frequency of the machine.

To address these opposing constraints, the vibration isolation achieved by using compliant mounts can be supplemented by other passive control techniques, such as the addition of mass to change the resonance frequencies, applying damping materials to

reduce the vibration at resonance frequencies or fitting vibration neutralisers to reduce the overall excitation experienced by the machinery raft.

An alternative strategy is to replace the passive isolation system with an entirely active system. Active control is achievable for example, by electromagnetic levitation of the machinery – active rafting. However, electromagnetic levitation is very expensive, requires a large amount of power to implement and still needs a back up system of conventional passive vibration mounts that will provide a fail safe should the active mounting system fail. The preferred option is to use a hybrid solution, which combines techniques of active vibration control such as active damping of residual vibration or active vibration control using force actuators, with a passive mounting system. However, these active components can also be expensive to install, and although they may be included in the design of a machinery raft, they are often not fitted due to their prohibitive expense.

This thesis considers the control of vibration from an elastic support structure upon which multiple vibrating systems are passively mounted, as shown in Figure 1.1. The figure depicts three machines with rotating components, which cause vibration to be transmitted to the machinery raft due to rotational imbalance. The excitations are assumed to occur at discrete frequencies with a finite number of harmonic components. A two-stage passive isolation system is employed to minimise the vibration transmitted from the machinery into the steel deck and hence into the surrounding structure. The machines are all assumed to be supplied with power from the same power supply. An example of such a structure is shown in Figure 1.2, which shows an arrangement of pumps mounted on a machinery raft.

Since the machines are driven from the same power supply, active vibration control may be achieved by adjusting the phase of the voltage supplied to one or more of the machines so that a minimum value of a measurable cost function is obtained. Adjusting the phase of a machine with respect to a reference machine is known as synchrophasing and is a well established technique for controlling the sound in aircraft cabins and in

ducts containing axial fans. However, the use of the technique for reducing the vibration of machinery mounted on elastic structures seems to have received very little attention in the literature and would appear to be a gap in the current knowledge. This thesis aims to address that gap by investigating theoretically and experimentally how synchrophasing can be implemented as an active structural vibration control technique.

1.2 Literature Review

This section describes previous work carried out in the field of structural vibration control, where vibrating machinery is the primary source of vibration excitation. The section starts by describing the advantages and limitations of traditional passive control techniques, including using compliant mounts and neutralizers. Active vibration control techniques are then described, with an overview of feedback and feedforward control, response sensors, activators and control strategies. It is shown that optimum control is achieved by adjusting both the magnitudes and the phases of the applied controlling forces when the sources are harmonic. The literature review concludes with an overview of work previously conducted into synchrophasing as a noise and vibration control technique and describes the current gaps in knowledge.

1.2.1 Overview of Passive vibration control

The usual approach taken by designers of passive machinery isolation systems has been to mount vibrating machinery on flexible isolation mounts in order to reduce the forces that the machine applies to the surrounding structure. In order to achieve the highest level of isolation, the simplest approach is to isolate each machine individually, and this is the approach usually described in the texts on the theory of vibration isolation [1-4]. However, the machinery on a large structure such as a ship rarely operates in isolation and so requires flexible interconnections between many of the machines. For example, diesel engines require coupling to gearing and propeller drive shafts, pumps require coupling to fluid systems and diesel generators supply power to many onboard electrical systems. Designing flexible connectors that can provide effective isolation and perform reliably for an extended period of time is very difficult [5, 6]. From the perspective of

machinery operation, reliability and ease of maintenance there is an advantage to grouping machinery systems together on a large machinery raft and then isolating these machinery rafts from the surrounding structure. These two-stage isolation systems are dealt with in vibration textbooks as an extension to the simple theory of vibration isolation, where the machinery raft is modelled as a rigid body structure and the force transmitted from the machinery to the surrounding structure via the two-stage isolation system is characterised by the force transmissibility [1, 2]. However, treating the machinery raft as a rigid body is not appropriate at all frequencies where vibration occurs, because ships are often equipped with lightweight flexible machinery rafts. In these cases the vibration modes of the machinery raft, the positioning of the machinery upon the raft and the positioning and number of mounts used to connect the raft to the surrounding structure are all important for minimising the force transmissibility [6-10].

Examples of other passive techniques, that are used to help to minimise the force transmission from the vibrating machinery to the surrounding structure, include careful balancing of the rotating components of machinery. Balancing minimises the transmission of vibration due to the presence of eccentric rotating masses, or the misalignment of connecting components [1, 11]. Alternatively, mass can be added or removed from the machinery raft in order to change its natural frequencies of vibration, to ensure that it does not resonate at a frequency excited by the machinery vibration [12].

An alternative technique proposed by Swinbanks [6] is to distribute the machinery raft mounting points so that they are placed at positions of high mass, each with appropriate stiffness to isolate the mass above it. This gives each mount the transmissibility characteristics of a single degree of freedom isolator.

Another alternative is to introduce a dynamic vibration absorber as described by Ormondroyd and Den Hartog [13] which reduces the vibration of the structure to which it is attached at a single frequency, and is thus most suitable for machinery operating at a constant speed. The vibration of variable speed machinery can be reduced, by using a

vibration absorber with damping, when the speed range is known. A great deal of work followed on from this paper, researching the effectiveness of vibration absorbers. This led to a class of adaptive devices called vibration neutralizers, where the dynamic stiffness of the neutralizer is adjustable, so that changes in machinery speed, and hence excitation frequency can be tracked, allowing the vibration reduction to be optimised. Examples of relevance are a method of global control of the vibrational kinetic energy of a structure using single and multiple tunable vibration neutralizers [14, 15] and a method of controlling the vibration transmitted from an aircraft engine to the fuselage using vibration absorbers [16].

Damping techniques such as constrained layer damping and viscoelastic damping mechanisms have also been suggested for reducing the vibration of lightweight machinery rafts [17].

1.2.2 Overview of Active vibration control

The concept of cancelling unwanted sound or vibration by superimposing the signal from one source onto another source with the same magnitude but with a 180° phase shift is not new. In 1878 Lord Rayleigh described sets of waves which neutralize one another to produce "points of silence" [18], which was utilising the principle of superposition and the constructive and destructive interference of two wave fields in order to cancel the total field at a point.

In 1934, the first example of actively adding a sound wave in order to control a sound field was presented, when Lueg filed a patent for the idea of capturing the sound field within a duct and generating an additional sound field further down the duct, in order to reduce or eliminate the total noise field in the duct [19]. This patent contained the essential elements of an active control system described by Fuller, Nelson and Elliott [20], namely a sensor to detect the uncontrolled sound or vibration, an electronic controlling system to manipulate and generate a controlling signal and an actuator, to produce the controlling signal to change the response of the uncontrolled system such that the total sound or vibration level is lowered.

1.2.3 Overview of Feedback vibration control

Feedback control systems are those for which the control signal obtained from the detecting sensor contains both the primary noise source and the secondary noise source. For this approach, the original primary excitation signal cannot be observed in isolation and thus cannot give *a priori* information about the primary noise source. This is shown in Figure 1.3 for the case of a single primary excitation source, a single vibration response sensor and a single actuator. An example of feedback control is the electronic sound absorber [21] presented by Olson and May, which consists of a microphone located close to a loudspeaker and an amplifier. This absorber is used to control the sound pressure in the vicinity of a microphone by driving the loudspeaker in such a way as to null the sound pressure, creating a quiet area around it. A further example of feedback control can be seen in research conducted by Balas into the active vibration control of large lightweight flexible structures such as space satellites, by using point actuators to control certain critical modes of vibration [22]. The modal control method was later refined by other researchers, for example the Independent Modal Space Control method suggested by Meirovitch for controlling the vibrations of a distributed mass system [23-25] and subsequently modified by others to minimise the effect of control spillover into unmodelled modes, such as those that are truncated in the modal formulation [26, 27] .

1.2.4 Overview of Feedforward vibration control

Feedforward control systems are those for which prior knowledge of the primary excitation signal is available. In general, there are two cases which allow this *a priori* knowledge. The first is the case where the vibration signal is propagating through a mechanical structure or through the air in the case of a sound wave, and a sensor can be used to detect the disturbance. The propagation time between the sensor and the actuator must be long enough that there is time for the control system to determine and create the signal that must be fed to the actuator. This case is especially amenable to cancellation of guided sound waves in ducts where the primary and cancellation waves have the

same direction of propagation, and a sensor can be placed far enough away from the control source to avoid any near-field effects [28-30].

The second case is when the disturbance is deterministic, such that the future excitation can be perfectly predicted from the previous behaviour. This is the case for harmonic excitation, for example, the vibration generated by rotating machinery under constant load conditions [31]. In this case, a reference signal can be derived from the primary excitation source, for example a tachometer detecting the shaft speed on a rotating machine. The phase of the secondary controlling signals can then be maintained with respect to the primary reference phase. This case is shown in Figure 1.4 for a single primary excitation source, a single response sensor and a single actuator providing the secondary excitation. The primary excitation signal is fed in parallel to the vibrating system and to the controller, where the secondary excitation waveform is generated. The secondary excitation waveform may be a different amplitude and phase when compared to the primary waveform, but because the primary signal is available, the phase of the secondary can be fixed with respect to it.

Comparison of Figures 1.3 and 1.4 show that, while the response sensors form part of the control path for feedback vibration control system, they do not form a direct part of the control path for a feedforward vibration control system. Rather they are used to adapt the response of the controller, usually with the aim of minimising the output from one or more response sensors. For a feedback control approach, as the response signal gets smaller the gain on the signal must be increased in order to provide the secondary excitation, this can lead to instabilities in the feedback control system [20, 32]. For this reason, a great deal of recent research has been concerned with feedforward control, as this is inherently stable and offers improved performance over feedback methods [33].

1.2.5 Sensors and actuators

The number, type and positioning of response sensors on the vibrating system to be controlled depends upon the control strategy chosen. Traditionally, accelerometers have been used for measurements of vibration and as error sensors for feedforward active

vibration control. Alternatives, such as polyvinylidene fluoride (PVDF) patches, long thin PVDF sensors and optical fibre sensors have also been developed for vibration control. Although they offer a distinct advantage in terms of conforming to the shape of the vibrating structure and may be shaped and placed to generate a signal only when certain modes of vibration are present, they can also be prone to electrical noise problems [34-37]. The number of sensors used depends upon the type of control which is attempted. In local control, the main focus is to minimise the error response at certain points on the vibrating system and no consideration is given to the vibration response outside these points. As such, local control requires sensors only at the points of interest. Alternatively, global control requires more sensors because minimisation of errors across the whole structure is considered.

Electromagnetic shakers have traditionally been used as actuators for active vibration control. They are very convenient as the come in a very large range of sizes and masses and so are suitable for use in systems from laboratory experiments up to large scale installations on working platforms, such as ships. For systems which can be controlled with low magnitudes of forces, then piezoelectric actuators offer a lightweight alternative [38, 39]. Piezoceramic stack actuators can be built up from layers of piezoelectric material and these are capable of providing higher control forces that are more suitable for use in larger structures [40, 41].

1.2.6 Control strategies

The feedforward vibration control strategies that are relevant to the structure described in this thesis are those controlling a thin flexible structure, such as the beam described by Brennan *et al* [42]. The wave suppression approach is achieved by considering the vibration as a wave propagating on the beam [43, 44] and is very similar to the feedforward control suggested by Lueg for controlling the sound propagating in a duct. Two other strategies that have been widely reported in the literature are those of maximizing the power absorbed by secondary actuators, dampers or damping layers [45, 46] and that of minimising the total power, or time averaged kinetic energy supplied to the structure by all vibrating sources [47, 48]. All of these techniques show

that the best control is achieved when both the amplitude and phase of the controlling forces are adaptively changed as required [49].

Brennan *et al* concluded [42] that the best overall control strategy for global control on a vibrating finite beam in flexure, was to minimize the total power supplied to the beam. This thesis will compare a global approach, where the total time averaged kinetic energy in the intermediate structure is minimised by synchrophasing, with a local approach, where point amplitude measurements of squared velocity are used as the cost function. These point amplitude measurements are made at each end of the intermediate structure, where it is connected to the host structure via vibration isolators.

1.2.7 Overview of Synchrophasing

In 1905, Mallock reduced the vibrations originating from two engines of a steam ship by making them run at the same speed, but in anti-phase to each other [50], which is the first documented example of synchrophasing. Synchrophasing differs from full active vibration control in that additional actuators to control the vibration are not usually fitted to the vibrating structure. Instead, the phases of vibrating machines that are already part of the structure are adjusted relative to a reference phase machine, the aim being to reduce the overall vibration levels. So there is no additional weight penalty due to extra components added to the structure. Synchrophasing is thus ideally suited to reducing the noise and vibration levels from rotating structures such as axial fans within a duct, aircraft propellers and ship propulsion systems. In 1940 Kalin patented a method of synchrophasing the main propulsion engines of a ship with multiple propellers, in order to reduce the vibration levels within the ship [51]. The system maintained a constant phase angle between the crank shafts by means of governors fitted to each Diesel engine. Kalin noted in the patent that the method could be applied to synchronising pump-driving engines to reduce the vibration due to machinery unbalance. Synchrophasing has become widely adopted for reducing the vibration levels of main propulsion machinery, especially for cruise ships with pod propulsion systems. Although the most usual technique is a fixed phase system, rather than an adaptive

system which is capable of changing the phases of the power supplied to each pod as operational requirements dictate.

In 1977 Harada obtained a patent for reducing the blade passage tonal noise of two fans in a duct by changing the relative angle between the two sets of fan blades [52]. This technique has been investigated experimentally and has shown that synchrophasing can reduce the sound pressure level of the blade passage frequency or harmonics by 10 dB [28]. However, since the fundamental blade passage frequency and the harmonics do not generally have the same optimum synchrophase angles, it is generally not possible to minimise the fundamental and all harmonics simultaneously.

By far the most literature on synchrophasing has been concerned with reducing the cabin noise and vibration inside propeller driven aircraft. The most important frequencies being the blade passage frequency and the lowest order harmonics. Previous research in the 1980's showed that synchrophasing could reduce the overall noise levels within the cabin of a propeller driven aircraft by approximately 10 dB [53-56]. However, the success of synchrophasing was limited at the time by the technology available. Commercial synchrophasers at the time were only capable of 25° steps, which is insufficient to cope with the changes in propeller induced cabin noise experienced during flight operations. Recent research has concentrated on active synchrophasing using microphones and accelerometers positioned throughout the aircraft, together with adaptive optimisation techniques to minimise the cabin noise and vibration over a wider range of flight conditions [57-59]. Algorithms for finding the minimum of the cabin noise sound pressure level include an exhaustive search of all the possible synchrophase angle combinations and the iterative gradient decent technique [49]. The time penalty of both of these techniques can be lessened by employing Propeller Signature Theory as described by Johnston, Donham and Guinn [60], where the individual propeller contribution at any location is called its signature at that location. So the total propeller related noise and vibration at a particular location in the aircraft cabin is determined by calculating the vector sum of the signatures from each propeller. Once the propeller contribution at each response sensor is determined, the process of finding the minimum

sound pressure level can be carried out using mathematical simulation assuming that the system has local linearity.

For propeller driven aircraft, it is not usually practical to switch off all but one engine in order to determine the signature for each propeller at each response sensor location. Johnston describes using the same number of propeller phase combinations as there are propellers, for a fully determined solution. For example, four different combinations of propeller phases for an aircraft with four propellers will enable each propeller signature to be determined. A more accurate method is to use more combinations of propeller phases than there are propellers. This enables a least squares over-determined solution to finding the signature of each propeller.

1.2.8 Current gaps in Knowledge

There are two patents by Pla [61, 62], for reducing noise and vibration from multiple rotating machines such as engines, turbines and cooling fans. Other than this, synchrophasing seems to have received very little attention in the literature for controlling the vibration of raft mounted machinery by adjusting the phase of the voltage supplied to the machinery.

To the author's knowledge, no work has been reported using Propeller Signature Theory to determine the signature between vibrating machinery mounted on a thin compliantly mounted elastic raft and error sensors placed on the raft, with the aim of minimising a cost function by synchrophasing, based upon the machinery signatures.

1.3 Thesis Objectives

This thesis aims to address some gaps in the current knowledge, of the effectiveness of synchrophasing, when applied to the vibration control of compliantly mounted machinery rafts, by presenting a theoretical and an experimental model of synchrophasing on a laboratory scale.

Propeller Signature Theory is used in the theoretical and experimental models to find the minimum of a cost function by synchrophasing. The results obtained by simulation using the theoretical model are compared to those obtained experimentally and the time taken to perform an exhaustive full search is compared to the time taken to determine the minimum by calculating the machinery signatures and using these in a simulated full search using Propeller Signature Theory.

The objectives of this thesis are to:

- develop a receptance based analytical model to study the vibration of an elastic structure due to forces generated by the vibrating machinery mounted on it.
- analyse the interactions between multiple vibrating harmonic sources when mounted on a common elastic structure and acting at the same frequency.
- design a method to adapt synchrophasing from an active sound control technique to an active structural vibration control technique.
- investigate the use of Propeller Signature Theory - a technique developed for measuring and reducing aircraft propeller noise - in minimising the vibration of machinery mounted on an elastic platform.
- design and build an experimental system to represent the machinery mounted on an elastic structure.
- design and build an experimental synchrophasing system, to optimize the control of the structural vibration of a simple structure, using different search methods to minimize the cost function.
- verify the predictions obtained from the analytical model by conducting a series of experiments using the laboratory based experimental synchrophasing system.
- present theoretical and experimental results to show the vibration reduction that is achievable by using synchrophasing.
- determine the practical requirements for implementing a simple synchrophasing system to control the transmission of vibration to the surrounding structure.

1.4 Contributions of the Thesis

The work presented in this thesis, builds on the body of work of synchrophasing reported for controlling the sound and vibration within an aircraft cabin. The techniques are developed in the design of an adaptive synchrophasing system that can be applied to a compliantly mounted machinery raft, upon which vibrating machinery is the source of vibration.

The contributions of this thesis are as follows:

- The importance of controlling the rigid body modes of a thin, flexible beam is shown, when using the total time averaged kinetic energy as the cost function in structural vibration control. Of particular importance is the position of the node of the rotational rigid body mode, which depends upon the positions of the machinery on the support structure.

- It is shown theoretically and experimentally that the techniques developed for Propeller Signature Theory can be applied for structural vibration control of a flexible machinery raft, and is an effective means of control.

- It is shown theoretically and experimentally that the total time averaged kinetic energy in the support structure and the sum of the magnitude squared of the velocity over each mount point, can both be used as effective global and local cost functions respectively. The best cost function to use – in terms of achievable reduction – depends upon the frequency of excitation and the positions of the machinery upon the supporting raft with respect to the nodes of the dominant modes of the machinery raft that are excited at the frequency of interest. Global control requires knowledge of the transfer mobilities between the machinery and the masses of the machinery and the supporting structure. Local control only requires vibration at the mount points of the supporting structure to be measured, and so is more suitable to implement and retro-fit onto an existing machinery raft.

- It is shown analytically and with simulations that when only two vibrating sources are present on a generalised elastic structure, then a simple expression can be obtained for the optimum synchrophase angle of the control machine, with respect to the phase of the reference machine. This angle is often just either in phase or in anti-phase with the reference, and depends upon the positions of the vibrating sources on the structure, the positions of the nodes of the dominant modes and the magnitude of the modal forces.

- It is shown analytically and with simulations that when a generalised structure contains more than two vibrating sources (one reference and P control sources) then interaction terms exist between the control sources. These interaction terms can work against each other, the result being that there may not be a unique minimum of the cost function. In this situation it is necessary to perform a search over the whole cost function surface in order to find a global minimum and the best synchrophase angles.

1.5 Thesis outline

This section describes the layout and content of the rest of the thesis. Chapter 2 introduces an abstraction of the problem that is investigated in this thesis - the vibration control of a machinery raft - to a generalised one dimensional structure. A model based upon the point and transfer receptances of the constituent components is described and used to predict the displacement at any point on the generalised structure due to local vibration, for example that caused by machinery unbalance. Expressions for the vibration response due to two vibrating sources and then multiple vibrating sources are introduced and analysed.

Chapter 3 discusses the idea that, for the types of generalised structures of interest in this thesis, it will not be possible to alter the magnitude of the unbalance forces caused by the vibrating sources. This is because the vibrations are generated by machinery,

which is required to run at a predetermined speed (RPM). Hence control can only be attempted by altering the phases of the unbalanced forces with respect to a reference source.

To quantify the effect of the control, cost functions are derived for the overall time averaged kinetic energy of the structure and for the sum of the squares of the magnitude of the velocities over each mount point. The latter cost function is simpler to implement from a practical point of view and could easily be retro-fitted to existing machinery rafts.

Two methods of finding the minimum of these cost functions are then described and compared for ease of application and the ability to find the overall global minimum. These two methods involve a full search conducted over all phase angles and a method of determining the transfer function between each machine and each vibration sensor based upon Propeller Signature Theory. The latter method enables a full search to be simulated, using the transfer functions, which represents a considerable time saving over having to step through each angle individually. The chapter concludes by describing a fundamental difference between synchrophase control when only two vibrating sources are present and that when more than two are present.

The experimental investigations of synchrophasing as a noise control technique and supporting numerical simulations are presented in Chapter 4. The chapter begins with a description of a physical model which was used to investigate control by synchrophasing. The sources of vibration were electromagnetic shakers which applied a force to the supporting beam as a result of the reaction against an attached mass load.

Methods of measuring the time averaged kinetic energy, using a laser vibrometer and also measuring the sum of the squares of the magnitude of the velocity at each end of the beam are described. A method of automating the calculation of the cost function, in response to changes in the phase angles of the applied harmonic excitations is described and implemented in LABVIEW® and MATLAB®. The experimental determination of

the synchrophase angles demonstrates the power of the propeller signature theory technique and enables much faster calculation of the optimum angles for each of the vibrating sources. The results obtained are discussed and compared to simulations.

Chapter 5 presents the conclusions of the thesis and draws together the major findings and ideas from the previous chapters. Recommendations for future studies and extensions of synchrophasing are also provided.

1.6 Figures

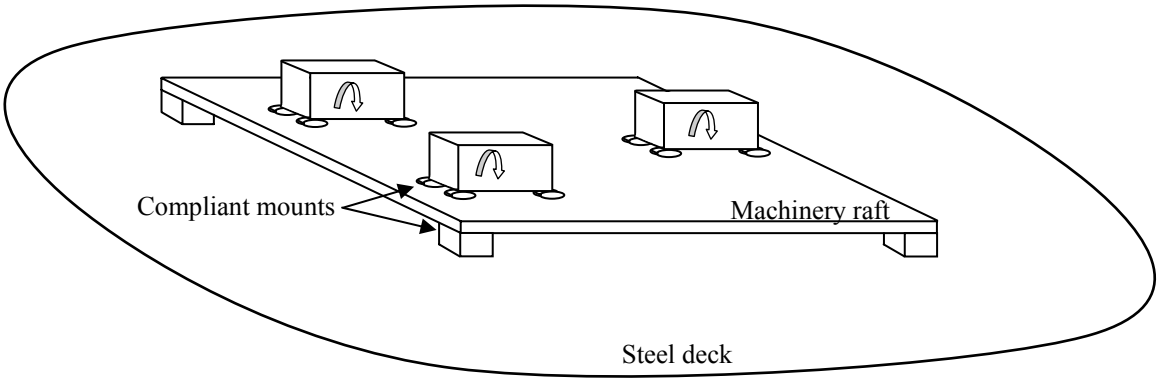

Figure 1.1. A representation of machinery with rotating components mounted on an elastic machinery raft. The system utilises two-stage passive isolation so the machinery and the machinery raft are all supported by compliant mounts.

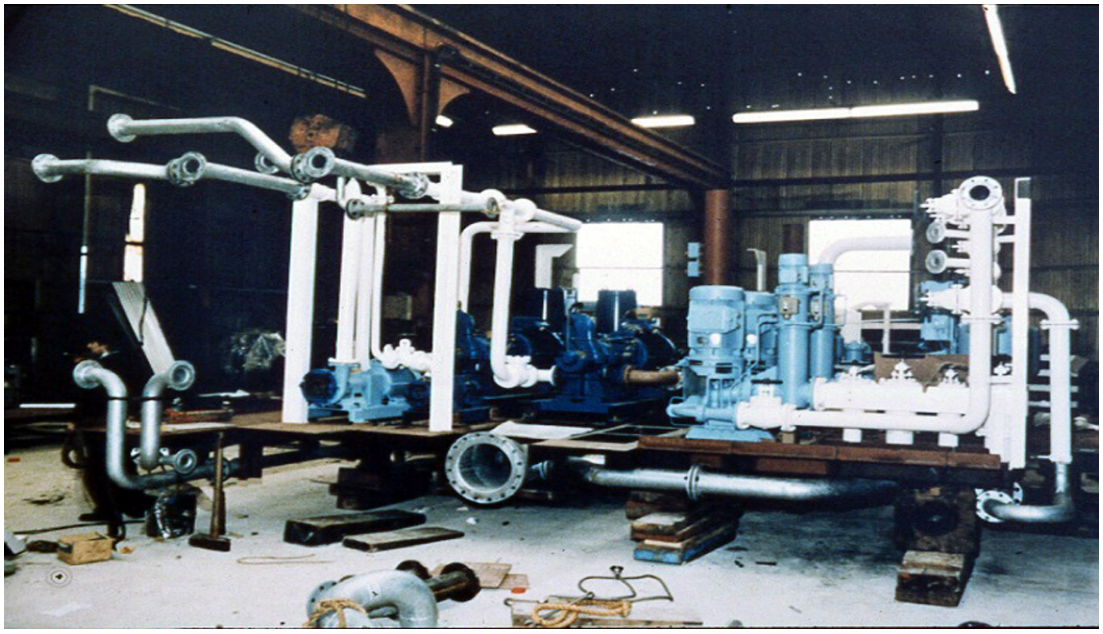

Figure 1.2. Part of a machinery raft with rotating components mounted on a thin elastic base. Courtesy of Shipbuilding Pictures Database NSnet.com.

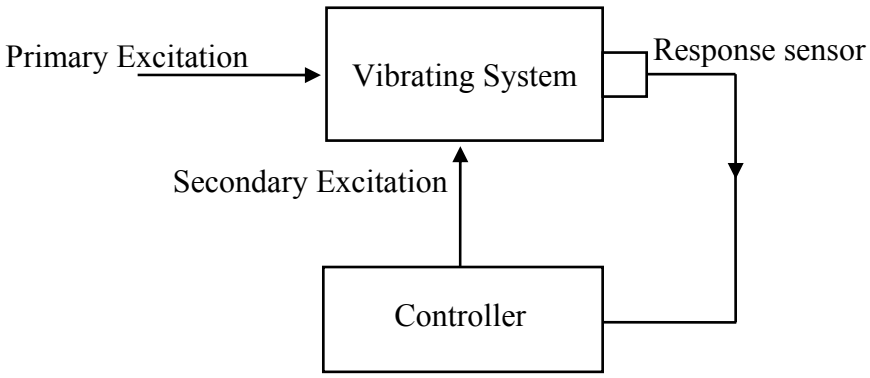

Figure 1.3. An example of feedback vibration control

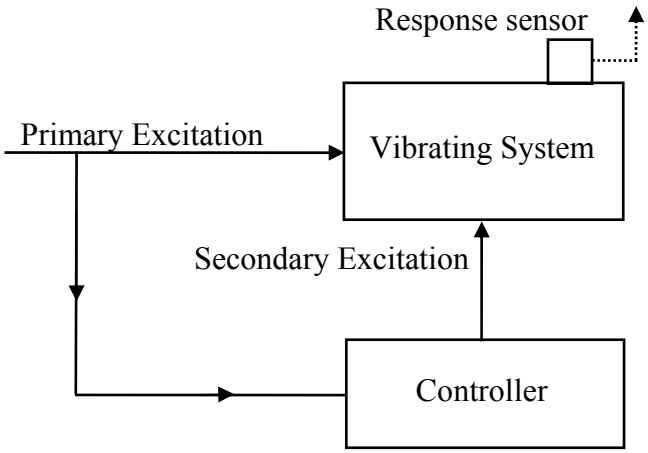

Figure 1.4. An example of feedforward vibration control

2 Development of an analytical and a physical model of a general elastic structure

2.1 Introduction

This chapter describes the development of two models of a generalised elastic structure that are used to investigate the effectiveness of synchrophasing as an active structural vibration control technique. A receptance approach is adopted for the analytical modelling. Receptance techniques have been used for many years to study mechanical systems involving lumped parameter and distributed parameter components [63]. It was decided to use a receptance based model because the point and transfer receptances of the constituent components can easily be measured experimentally without requiring detailed knowledge of the system mode shapes.

The analytical model can be used to determine the displacement at any point on the generalised structure caused by vibration due to machinery unbalance forces acting upon the structure, and can be used to investigate synchrophasing. Expressions for the displacement due to multiple vibrating sources are derived and introduced.

The receptance based analytical model is also used to guide the design and development of a physical laboratory model. This physical model is used to validate the theoretical predictions, to understand the practical limitations of implementing a synchrophasing system on an existing structure and to provide a technology demonstrator.

2.2 Development of a Receptance based model

Figure 2.1 shows the generalised structure that is used to investigate the effectiveness of synchrophasing as an active structural vibration control technique. In the physical model, electromagnetic shakers are used to represent the extra masses of machinery vibrating on a thin elastic support raft. The generalised structure consists of a compliantly mounted thin elastic beam upon which $P+1$ shakers are mounted. This allows for one shaker to be used as a reference phase source and P shakers to be used

for synchrophasing control, where the phase of the voltage supplied to each shaker can be varied with respect to the phase of the voltage applied to the reference shaker. Since low frequency vibration is the most problematic vibration source for large machinery installations [7, 33, 64], this thesis is concerned with situations where the flexural wavelength is large compared to the thickness of the elastic beam, so the effects of shear deformation and rotary inertia can be ignored [65]. Without loss of generality, the models developed for this thesis use Euler-Bernoulli beam theory [1] to represent the thin elastic support raft as a one-dimensional thin beam.

Figure 2.2 shows the coordinate system and variables used in modelling the generalised structure, which is a composite system consisting of discrete components such as the masses of the shakers and the stiffness of the supporting mounts, and a thin elastic beam which is a distributed parameter element. The uniform box section beam is supported at each end by mounts of stiffness k_1 at coordinate $x_{s1} = 0$ and k_2 at coordinate $x_{s2} = L$, where L is the length of the beam. k_1 and k_2 are complex due to damping in the mounts. The shakers are considered to be point masses of mass $m_r, m_1, m_2 \ldots m_P$. The positions of the shakers on the beam are given by the coordinates $x_r, x_1, x_2 \ldots x_P$ respectively. Forces f_r to f_P act on the beam as a result of the reaction against each shaker mass load.

2.2.1 The receptance approach

The displacement w of the generalised elastic structure at any point x on the structure can be determined if the point and transfer receptance of the components of the composite system are known [66, 74]. The composite system is decomposed, such that the receptance of the components are known either as simple functions, or in terms of analytical expressions. The subdivision used in this analysis is to split the composite system into a subsystem of discrete components, consisting of the external masses and springs and a subsystem of continuous components consisting of the uniform thin beam with free-free end conditions, as shown in Figure 2.3. The excitation and response of the system are assumed to be harmonic at a single frequency.

For clarity of deriving the system equations, the external components that are attached to the beam at positions $x_r \ldots x_P$, x_{s1}, x_{s2} are given a single letter subscript $x_a, x_b \ldots x_f$ as shown in Figure 2.3, where four external masses mounted on the beam have been assumed.

For the beam subsystem, the displacement of the beam at positions $x_a, x_b \ldots x_f$ where the external components are attached can be represented by

$$\begin{bmatrix} w(x_a) \\ w(x_b) \\ w(x_c) \\ w(x_d) \\ w(x_e) \\ w(x_f) \end{bmatrix} = \begin{bmatrix} \beta_{aa} & \beta_{ab} & \beta_{ac} & \beta_{ad} & \beta_{ae} & \beta_{af} \\ \beta_{ba} & \beta_{bb} & \beta_{bc} & \beta_{bd} & \beta_{be} & \beta_{bf} \\ \beta_{ca} & \beta_{cb} & \beta_{cc} & \beta_{cd} & \beta_{ce} & \beta_{cf} \\ \beta_{da} & \beta_{db} & \beta_{dc} & \beta_{dd} & \beta_{de} & \beta_{df} \\ \beta_{ea} & \beta_{eb} & \beta_{ec} & \beta_{ed} & \beta_{ee} & \beta_{ef} \\ \beta_{fa} & \beta_{fb} & \beta_{fc} & \beta_{fd} & \beta_{fe} & \beta_{ff} \end{bmatrix} \begin{bmatrix} f_a \\ f_b \\ f_c \\ f_d \\ f_e \\ f_f \end{bmatrix} \tag{2.1}$$

where β_{ij} is the receptance of the free-free Euler-Bernoulli beam, i.e. the displacement at position x_i due to a force attached to the beam at position x_j. f_i is the force on the uniform free-free beam at position x_i. This can written in vector-matrix form as

$$\mathbf{w}_{\mathbf{dis}} = \mathbf{B}_{\mathbf{dis}} \mathbf{f}_{\mathbf{beam}} \tag{2.2}$$

where the subscript **dis** is used to emphasise that the displacement vector $\mathbf{w}_{\mathbf{dis}}$ and receptance matrix $\mathbf{B}_{\mathbf{dis}}$ refer to points on the beam where the external **dis**crete components are attached. $\mathbf{f}_{\mathbf{beam}}$ is the vector of forces on the beam at the locations of the attached external components. By using a 'compatibility condition' [66] which requires the displacement of the external components to be the same as that of the beam at the point where the external components are attached, the displacement of the external components at positions $x_a, x_b \ldots x_f$ can be represented by

$$\begin{bmatrix} w(x_a) \\ w(x_b) \\ w(x_c) \\ w(x_d) \\ w(x_e) \\ w(x_f) \end{bmatrix} = \begin{bmatrix} \gamma_{aa} & 0 & 0 & 0 & 0 & 0 \\ 0 & \gamma_{bb} & 0 & 0 & 0 & 0 \\ 0 & 0 & \gamma_{cc} & 0 & 0 & 0 \\ 0 & 0 & 0 & \gamma_{dd} & 0 & 0 \\ 0 & 0 & 0 & 0 & \gamma_{ee} & 0 \\ 0 & 0 & 0 & 0 & 0 & \gamma_{ff} \end{bmatrix} \begin{bmatrix} f_r \\ f_1 \\ f_2 \\ f_P \\ f_{s1} \\ f_{s2} \end{bmatrix} \tag{2.3}$$

where γ_{ii} is the receptance of the attached mass or spring at position x_i, f_i is the force on the point mass at position x_i and f_{si} is the force on the spring mounts at x_i. This can written in vector-matrix form as

$$\mathbf{w}_{\mathbf{dis}} = \boldsymbol{\Gamma}\mathbf{f}_{\mathbf{c}} \tag{2.4}$$

where the vector $\mathbf{f_c}$ represents the forces acting upon the attached masses and springs and $\boldsymbol{\Gamma}$ is the receptance matrix for the attached components. Using the compatibility condition, Equations (2.2) and (2.4) can be combined to give

$$\mathbf{B}_{\mathbf{dis}}\mathbf{f}_{\mathbf{beam}} = \boldsymbol{\Gamma}\mathbf{f}_{\mathbf{c}} \tag{2.5}$$

If the composite system is acted upon by external forces $f_1\ f_2 \ldots f_P$, then

$$\mathbf{f}_{\mathbf{beam}} + \mathbf{f}_{\mathbf{c}} = \mathbf{f}_{\mathbf{ext}} \tag{2.6}$$

where, for external forces applied to the masses (shakers) as shown in Figure 2.3, the vector of external forces is given by

$$\mathbf{f_{ext}} = \begin{bmatrix} f_r \\ f_1 \\ \vdots \\ f_P \\ 0 \\ 0 \end{bmatrix} \tag{2.7}$$

where the last two elements are zero because no external forces are applied to the spring mounts.

Combining Equations (2.5) and (2.6) gives $\mathbf{B_{dis}}\mathbf{f_{beam}} = \mathbf{\Gamma}(\mathbf{f_{ext}} - \mathbf{f_{beam}})$. From which

$$\mathbf{f_{beam}} = \left(\mathbf{B_{dis}} + \mathbf{\Gamma}\right)^{-1}\mathbf{\Gamma}\mathbf{f_{ext}} \tag{2.8}$$

Equation (2.8) gives the forces on the uniform thin beam with free-free end conditions at the locations of the attached external components, in terms of the external forces applied to the shakers – or any other external forces if required. From this, the displacement of the composite system at any arbitrary position x on the beam can be calculated by

$$w(x) = \begin{bmatrix} \beta_{x,x_r} & \beta_{x,x_1} & \beta_{x,x_2} & \cdots & \beta_{x,x_P} & \beta_{x,x_{s1}} & \beta_{x,x_{s2}} \end{bmatrix}\mathbf{f_{beam}} \tag{2.9}$$

where $\beta_{x,j}$ is the receptance of the free-free Euler-Bernoulli beam, i.e. the response at an arbitrary position x, due to a force at x_j i.e. $\beta_{x,j} = \dfrac{w(x)}{f_j}$. Substituting Equation (2.8) into Equation (2.9) gives

$$w(x) = \begin{bmatrix} \beta_{x,x_r} & \beta_{x,x_1} & \beta_{x,x_2} & \cdots & \beta_{x,x_P} & \beta_{x,x_{s1}} & \beta_{x,x_{s2}} \end{bmatrix}\left(\mathbf{B_{dis}} + \mathbf{\Gamma}\right)^{-1}\mathbf{\Gamma}\mathbf{f_{ext}} \tag{2.10}$$

which can be written as

$$w(x) = \mathbf{A}_x \mathbf{f}_{\mathbf{ext}} \tag{2.11}$$

where the composite system receptance for an arbitrary response position x due to external forces and attached masses and springs is given by

$$\mathbf{A}_x = \begin{bmatrix} \beta_{x,x_r} & \beta_{x,x_1} & \beta_{x,x_2} & \cdots & \beta_{x,x_P} & \beta_{x,x_{s1}} & \beta_{x,x_{s2}} \end{bmatrix} \left(\mathbf{B}_{\mathbf{dis}} + \mathbf{\Gamma}\right)^{-1} \mathbf{\Gamma} \tag{2.12}$$

Equation (2.11) is used to calculate the lateral displacement at a finite number of points along the beam and can be used to simulate the measurement of the displacement at a finite number of points along the length of the structure. This result is used in Chapters 3 and 4 to simulate vibration control by synchrophasing. In this chapter it is used to help to design an experimental structure that can be used to demonstrate synchrophasing practically.

If the system is vibrating freely then the external forces acting upon the composite system are given by $\mathbf{f}_{\mathbf{ext}} = \mathbf{0}$, hence from Equation (2.6)

$$\mathbf{f}_{\mathbf{beam}} + \mathbf{f}_{\mathbf{c}} = \mathbf{0} \tag{2.13}$$

This can be substituted into Equation (2.5) to give

$$\left(\mathbf{B}_{\mathbf{dis}} + \mathbf{\Gamma}\right)\mathbf{f}_{\mathbf{beam}} = \mathbf{0} \tag{2.14}$$

Hence the natural frequencies of the composite system can be determined by the solutions of

$$\left|\mathbf{B}_{\mathbf{dis}} + \mathbf{\Gamma}\right| = 0 \tag{2.15}$$

using an eigenvalue routine. The natural frequencies obtained from the analytical model were compared with the natural frequencies obtained experimentally by impact testing of the physical model, as part of the validation process.

2.2.2 Time averaged kinetic energy of the composite beam system

In previous work [67], a discretised model of a thin beam with free ends was developed. This was used to calculate the total time averaged kinetic energy by determining the lateral displacement at a finite number of discrete points along the beam. It was reported that this model was representative of an experimental determination of the kinetic energy, where the lateral displacement along the beam is measured at discrete points, using for example, a laser vibrometer. This method does not require knowledge of the mode shapes of the composite system. The model that was developed can be extended to give the total time averaged kinetic energy of a composite beam system. Figure 2.4 shows how the composite beam model can be discretised into N_m discrete beam elements, allowing for the possibility of up to N_m external masses and/or springs. The external masses are represented as point masses m_i which can be zero for the elements where no additional mass is attached to the beam. For the i^{th} small element, the time averaged kinetic energy is given by [67]

$$\langle T_i(\omega)\rangle_t = \frac{\omega^2}{4}(\rho A\Delta x + m_i)\left|w(x_i)\right|^2 \tag{2.16}$$

where $\Delta x = L/N_m$ and represents the length of a small beam segment. The total time averaged kinetic energy of the beam, composed of N_m discrete beam elements and external masses can be written as

$$\langle T(\omega)\rangle_t = \frac{\omega^2}{4}\mathbf{w}^H\mathbf{M}_{\Delta}\mathbf{w} \tag{2.17}$$

where $\mathbf{w}$ is a column vector of length N_m containing the lateral displacement of each element, the superscript H indicates the Hermitian transpose of vector $\mathbf{w}$ and $\mathbf{M}_{\Delta}$ is the total mass matrix given by

$$\mathbf{M}_{\Delta} = \begin{bmatrix} \frac{\rho AL}{N_m} + m_1 & 0 & 0 & 0 & 0 \\ 0 & \frac{\rho AL}{N_m} + m_2 & 0 & 0 & 0 \\ 0 & 0 & \ddots & 0 & 0 \\ 0 & 0 & 0 & \frac{\rho AL}{N_m} + m_{N-1} & 0 \\ 0 & 0 & 0 & 0 & \frac{\rho AL}{N_m} + m_{N_m} \end{bmatrix} \tag{2.18}$$

Equation (2.17) can be used to determine the total time averaged kinetic energy of the generalised structure experimentally by measuring the displacement vector **w**. To determine the total time averaged kinetic energy analytically, the displacement vector **w** is obtained using the receptance approach described previously, where the receptance of the free-free beam β_{ij} at excitation frequency ω is given by

$$\beta_{ij}(\omega) = \frac{1}{-m\omega^2} + \frac{3(1-2\frac{x_i}{l})(1-2\frac{x_j}{l})}{-m\omega^2} + \sum_{k=1}^{\infty} \frac{W_k(x_i)W_k(x_j)}{m_{m,k}(\omega_k^2(1+i\eta)-\omega^2)} \tag{2.19}$$

where the first two terms of Equation (2.19) are rigid body modes, $m_{m,k}$ is the k^{th} modal mass, m is the mass of the beam, ω_k is the circular natural frequency of the k^{th} mode, η is the modal structural loss factor which is assumed to be constant for all modes and $W_k(x)$ is the mode shape of the k^{th} flexural mode of the free-free beam, normalised so that

$$\int_0^L W_k(x)W_k(x)\,dx = L \qquad k = 1, 2, 3 \ldots \tag{2.20}$$

For practical purposes, the infinite series of receptances given by Equation (2.19) is truncated to N terms. The two rigid-body modes and the first three flexural modes of the thin beam with free end conditions are shown in Figure 2.5.

2.3 Design and testing of the physical model

In order to investigate synchrophasing experimentally, it is necessary to have a laboratory scale model of the generalised elastic structure, so that the practical limitations of synchrophasing can be appreciated and a practical working synchrophasing system be designed and demonstrated.

The requirements of the physical model were that the thin elastic beam should be stiff but light, as this results in a system where the rigid-body modes of the beam on its compliant end mounts are well separated in frequency from the flexural bending modes. This facilitates an active control strategy of controlling the rigid body modes and minimising their contribution to the overall cost function, as previous work [68] has indicated that a large proportion of the total time averaged kinetic energy for a thin beam with free end conditions is in the rigid body modes at frequencies at and below the first flexural mode. To this end, it was decided to use a box section beam, as the box section provides the stiffness required to support the additional masses in the form of shakers, but is lighter than a solid beam. The properties of the extruded box section beam used are shown in Table 2.1 below.

Two variants of the RLF compliant mounts were tested for their suitability for use in the physical model, each with a different stiffness. The RLF Type 2 mounts had an experimentally determined stiffness of $k=9\times10^{3}\,\mathrm{Nm}^{-1}$ and the RLF Type 3 a stiffness of $k=17.4\times10^{3}\,\mathrm{Nm}^{-1}$.

The most suitable compliant mounts were RLF Type 2 mounts, which provided a large deflection under load and were designed for shock protection of delicate instruments. The stiffness of these mounts was determined experimentally by measuring the static deflection under load and is given in Table 2.1.

It was necessary to use two mounts at each end of the beam in order to provide a stable platform upon which to mount the shakers. The compliant mounts have screw threads at the top and bottom for ease of mounting to the beam and to the supporting base.

Beam	Material	Aluminium 6063-T6 Extruded Box section	Units
	Length	1.2	m
	Width	101.6	mm
	Height	25.4	mm
	Thickness	3.2512	mm
	Young's Modulus[1]	6.7×10^{10}	Pa
	Density[1]	2710	kgm^{-3}
Shaker	Make	Ling Dynamic Systems	
	Model	V101	
	Mass	0.91	kg
	Load mass on shaker	0.178	kg
Mounts	Make	RLF[3] High deflection rubber	
	Type	2	
	Stiffness[2]	9×10^{3}	Nm^{-1}

1 From manufacturer's data sheets
2 Measured by static loading
3 Purchased from antivibrationmethods.co.uk

Table 2.1. Physical properties of the experimental structure

Figure 2.6 shows simulations of the time averaged kinetic energy of the beam without shakers on, when each variant of mount is used, to show the effect of the stiffness of the supporting mounts on the time averaged kinetic energy of the beam. Also shown is the case where no end mounts are used. The figure shows that the effect of adding the springs at $x/l=0$ and $x/l=1$ is to increase the frequencies at which the rigid body modes occur from 0 Hz when no end mounts are present, to 18 Hz and 33 Hz for the RLF Type 2 mounts, and 24 Hz and 44 Hz for the RLF Type 3 mounts. This is in concordance with the equations for the natural frequencies of vibration when the compliantly mounted beam is considered as a two degree of freedom system, given by [1]

$$f_1 = \frac{1}{2\pi}\sqrt{\frac{k}{m}} \tag{2.21}$$

$$f_2 = \frac{1}{2\pi}\sqrt{\frac{3k}{m}} = \sqrt{3} f_1 \tag{2.22}$$

which shows that f_1, the natural frequency of the translational rigid body mode, and f_2, the natural frequency of the rotational rigid body mode of the structure, are both proportional to the square root of the stiffness, where k is the total stiffness and m is the total mass.

The RLF Type 2 mounts were chosen for the physical model because they provided a greater separation between the rigid body modes and the flexural modes. To provide a steady supporting base for the beam, another section of extruded aluminium box section beam was used, to which the compliant mounts were attached. Weights were attached inside the box section base to give it sufficient mass to remain stationary during the vibration testing. The experimental beam, compliant mounts and support base are shown in Figure 2.7.

A suitable length of beam for the physical model was determined by using the analytical model to calculate the natural frequencies of the composite system with different lengths of beam. It was decided that three flexural modes would be sufficiently representative of a real machinery raft, because the most problematic vibrations occur on machinery rafts at low frequencies. The physical model was constructed so that the first three flexural modes occurred at frequencies less than 1 kHz. This upper frequency limit ensured that sufficient flexural modes could be excited and analysed within the limitations of the experimental equipment available.

Once the physical model was constructed, the natural frequencies of the experimental beam without shakers were determined, by using an instrumented hammer to excite the structure, and measuring the acceleration of the beam to obtain the frequency response

function [69]. The results of the hammer excitation tests are shown in Figure 2.8 which shows the translational rigid body mode (RBM 1), the rotational rigid body mode (RBM 2) and the first two flexural modes (FM 1) and (FM 2) of the beam. It can be seen in Figure 2.8 that the rigid-body modes are well separated from the flexural modes, as was determined in the experimental design. The measured natural frequencies are compared to those obtained using Equation (2.15) from the analytical receptance model in Table 2.2 below.

Mode	Experimental Natural Frequency / Hz	Analytical Natural Frequency / Hz	Difference / Hz	Percentage Difference / %
Translational Rigid body mode	19	18	1	5
Rotational Rigid body mode	33	33	0	0
First Flexural mode	130	134	4	3
Second Flexural mode	330	356	26	8

Table 2.2. Comparison of the natural frequencies obtained experimentally with those predicted using the analytical receptance model for the first four modes of the beam.

For the two rigid-body modes and the first flexural mode there is good agreement between the analytical receptance model and the experimental physical model. There is a difference of 26 Hz (8%) for the second flexural mode. This level of agreement gives confidence in the analytical model, and shows that the physical model is well represented by Euler-Bernoulli beam theory, i.e. the physical model behaves as a one-dimensional beam at the frequencies of interest in this thesis.

Ling Dynamic Systems LDS V101 shakers were used to provide the external masses on the beam and to generate the forces applied to the beam by vibrating a 178g load mass as shown in Figure 2.9. An accelerometer was mounted on the load mass to measure the acceleration and hence determine the applied force. During the experimental set-up phase, the acceleration measured on the load mass was compared to the acceleration

measured on an accelerometer on the beam adjacent to the shaker as shown in Figure 2.9. This gave confidence that measuring the acceleration of the load mass was a valid method by which to infer the forces applied to the beam by the shaker. The mass of the shaker armature is 6.5g [73], this was ignored in the calculation of the applied force.

Figure 2.10 shows simulations which compare the time averaged kinetic energy of the structure when three LDS V101 shakers are mounted on the beam, to the time averaged kinetic energy when no external masses are present. This is to show the effect of the extra mass of the three shakers on the beam. In both cases, the beam is excited by point forces of the same magnitude and phase at positions $x/l = 0.08$, $x/l = 0.33$ and $x/l = 0.66$. As can be seen from Figure 2.10, the effect of the external masses is to lower the natural frequencies of the structure. This is in concordance with the equations for the natural frequencies of vibration of the two degree of freedom system given in Equations (2.21) and (2.22), which showed that the translational and rotational rigid-body modes are inversely proportional to the square root of the mass m. Also the natural frequencies of the thin beam in flexure are given by [1]

$$f_n = \frac{1}{2\pi}\beta_n^2\sqrt{\frac{E_y I}{\rho A}} \tag{2.23}$$

where f_n is the frequency of the n^{th} flexural mode, E_y is the Young's modulus, I is the second moment of area of the beam cross section about the neutral axis (the z axis using the coordinate system of Figure 2.2), ρ is the density of the beam, A is the cross sectional area of the beam and β_n is the n^{th} flexural wave number. It can be seen from Equation (2.23), that the frequencies at which the flexural modes occur are proportional to the square root of the bending stiffness $E_y I$ [70] and inversely proportional to the square root of the mass per unit length ρA.

Since each shaker is 0.91 kg and the static mass of the beam is 2.54 kg, the additional 2.73 kg mass of three shakers represents a significant increase to the mass of the generic

structure. This is representative of a real machinery installation, where the mass of the machinery is of the same order as the mass of the supporting raft structure.

2.4 Conclusions

This chapter has described the development of two models of a generalised one-dimensional elastic structure that were used to investigate synchrophasing as an active structural vibration control technique. One of these models is an analytical model and the other is a physical model.

Expressions for the displacement at any point on the structure, due to multiple vibrating sources that are attached to the structure, were derived by developing a receptance based analytical model, where the composite structure was considered as lumped parameter and distributed parameter components.

The receptance based analytical model was used to guide the design and development of a physical laboratory scale model, by simulating the effect on the overall time averaged kinetic energy of the structure, when the material and dimensions of the thin beam are changed, when the stiffness of the compliant mounts is changed and when the masses of the external components that are attached to the beam are changed. This enabled a physical model to be constructed where the rigid-body modes are well separated from the flexural modes and the first three flexural modes occurred at frequencies below 1 kHz.

After construction of the physical model, impact tests were performed to determine the natural frequencies of vibration, these showed good agreement when compared to the natural frequencies predicted using the analytical model. This gave confidence in the analytical modelling technique and showed that the physical model was behaving as a one-dimensional Euler-Bernoulli beam at the frequencies of interest in this thesis. The physical model was used during the experimental investigations into synchrophasing, which are described in Chapter 4. The analytical model was also used in Chapter 4 to validate the experimental results.

2.5 Figures

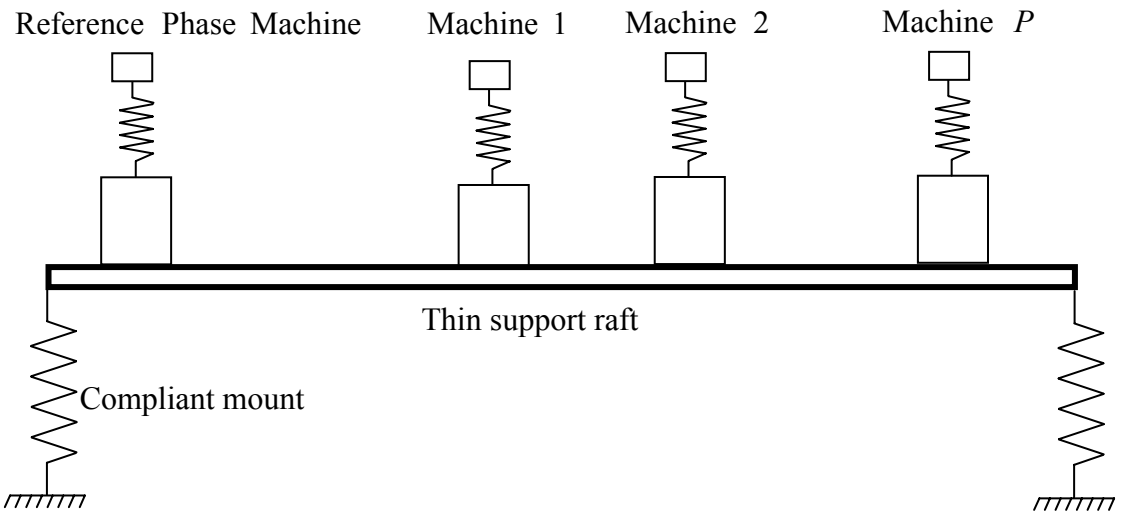

Figure 2.1. A diagram of the generalised structure. $P+1$ machines are mounted on a thin support raft, such that the phase of the voltage applied to the P control machines can be adjusted relative to the phase of the voltage applied to the reference machine. In the diagram P=3.

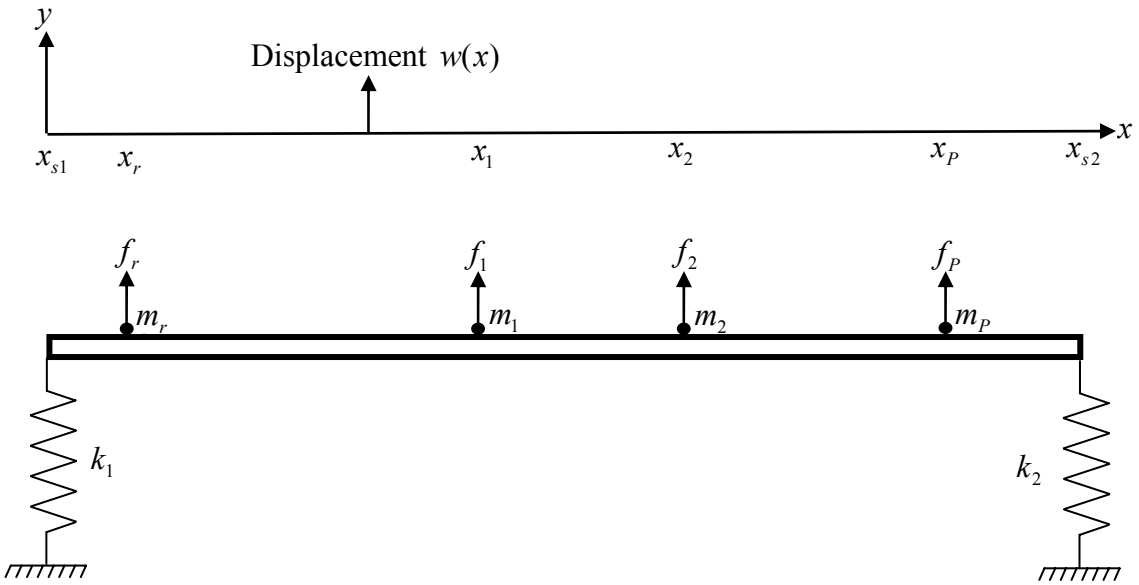

Figure 2.2. The coordinate system and variables used in modelling the generalised structure. The uniform box section beam is supported at each end by mounts of stiffness k_1 and k_2, which are complex due to damping in the mounts. The shakers are considered to be point masses of mass $m_r, m_1, m_2 \ldots m_P$. The positions of the shakers on the beam are given by the coordinates $x_r, x_1, x_2 \ldots x_P$ respectively. Forces f_r to f_P act on the beam as a result of the reaction against each shaker mass load.

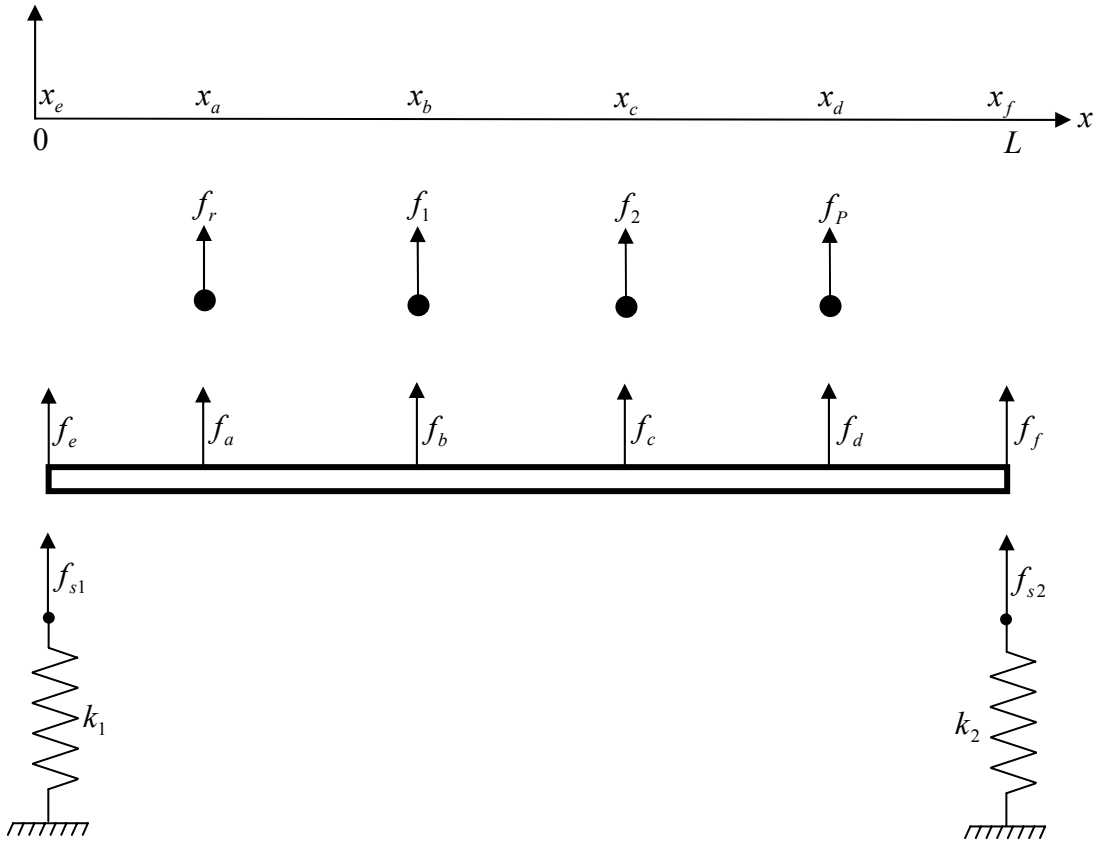

Figure 2.3. Subdivision of the composite system when $P+1$ shakers are mounted on the beam which is compliantly mounted on two springs of stiffness k_1 and k_2. For clarity, the external components attached to the beam at positions $x_r \ldots x_P$, x_{s1}, x_{s2} are given a single letter subscript $x_a, x_b \ldots x_f$.

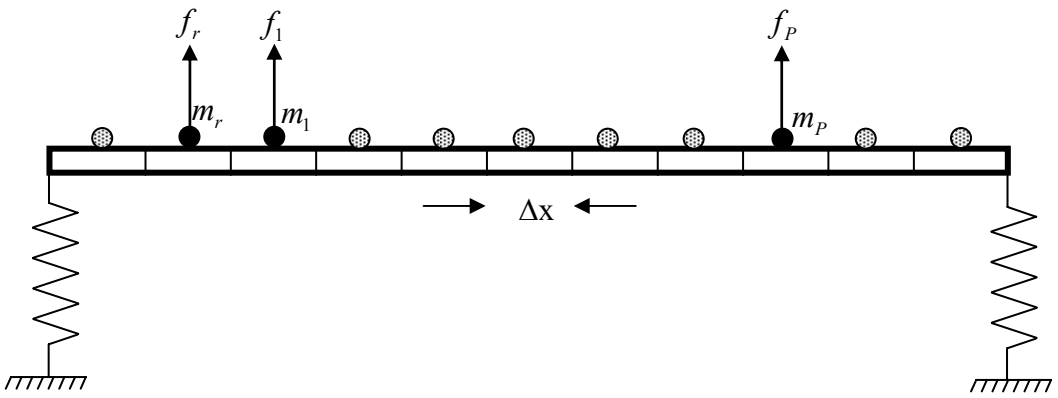

Figure 2.4. Discretisation of the composite system into N_m small elements, each of length Δx. Each small element has an additional mass m_i which can be set to zero at the positions where there is no shaker attached.

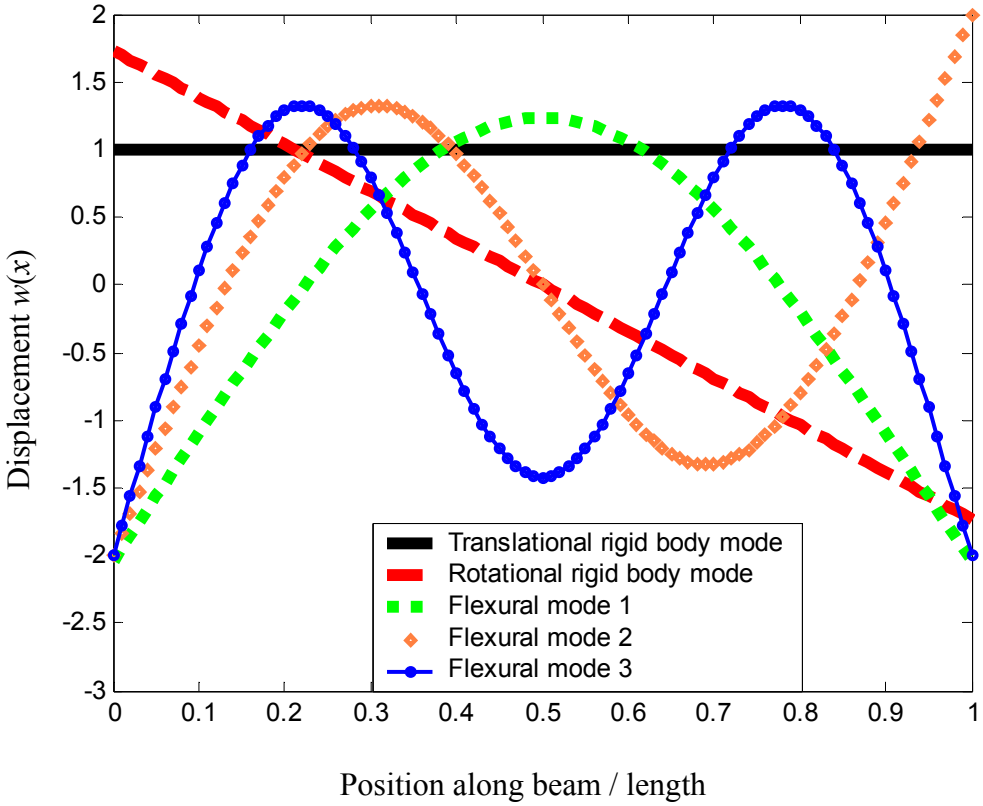

Figure 2.5. The rigid-body modes and the first three flexural modes of a thin beam with free ends.

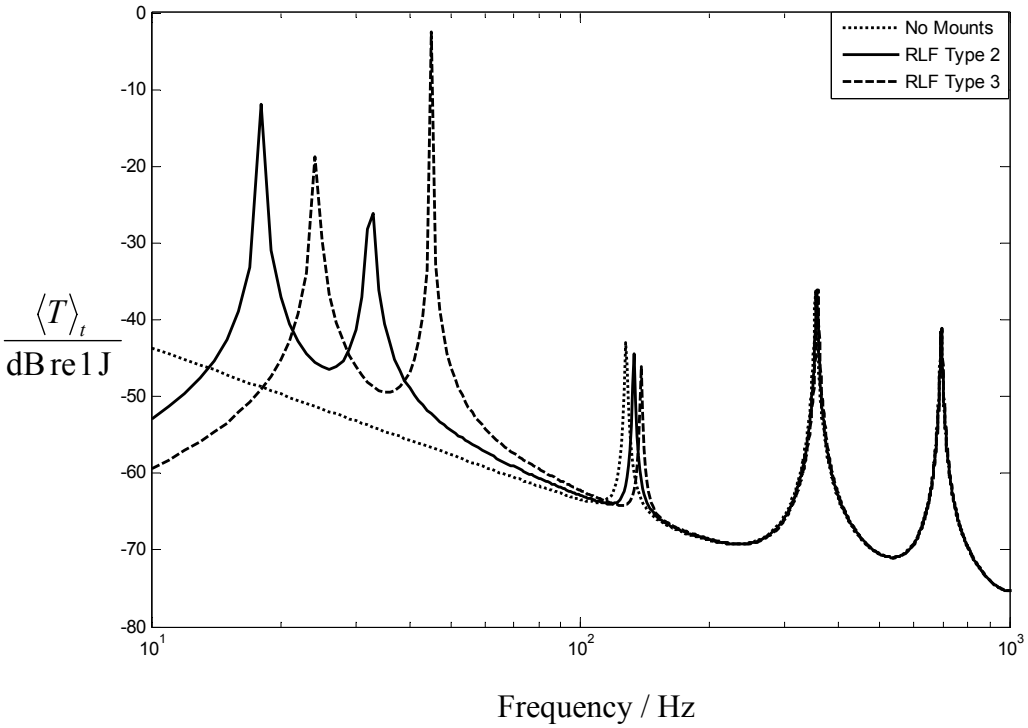

Figure 2.6. Simulations of the time averaged kinetic energy of the beam without shakers on, to show the effect of the stiffness of the supporting mounts. The beam is driven by a single point force at $x/l = 0.25$. For the dotted line no mounts were used in the receptance model (k=0 Nm^{-1}), the solid line used the stiffness of the RLF Type 2 mounts determined experimentally (k=9×10^3 Nm^{-1} for each mount) in the receptance model and the dashed line represents the case when the experimentally determined stiffness for the RLF Type 3 mounts (k=17.4×10^3 Nm^{-1} for each mount) is used in the model.

(a)

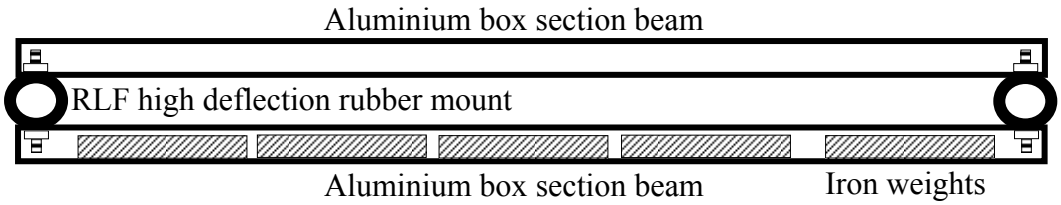

(b)

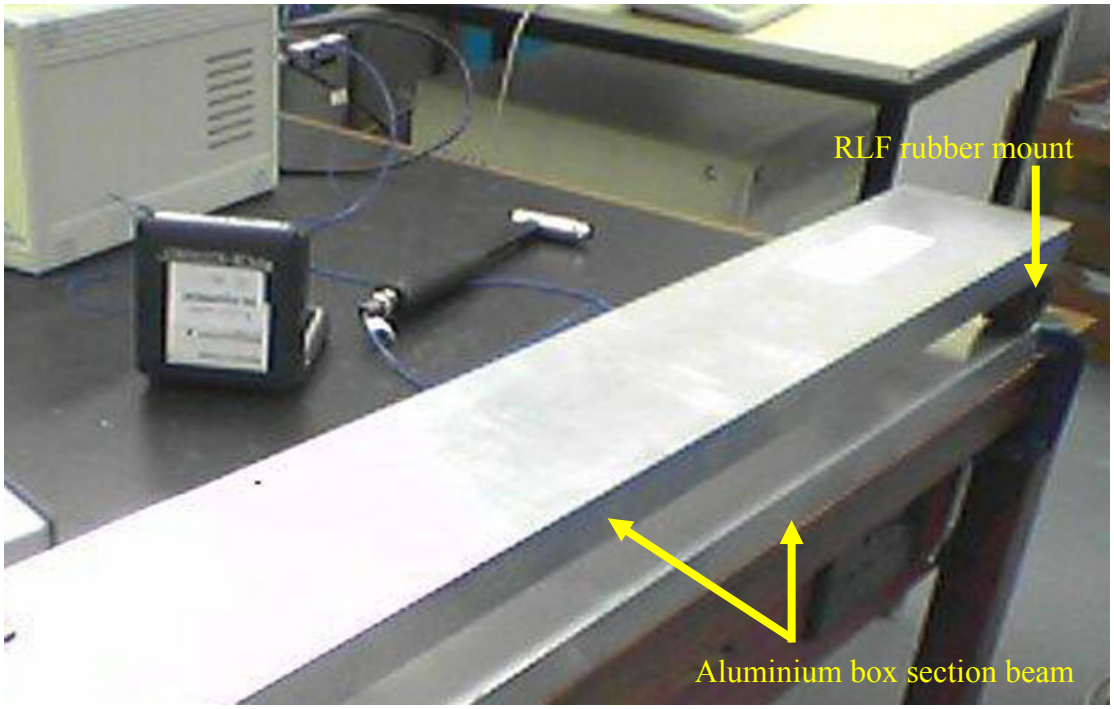

Figure 2.7. A diagram (a) and a photograph (b) of the experimental beam used to validate the analytical model and to assess the practical limitations of synchrophasing.

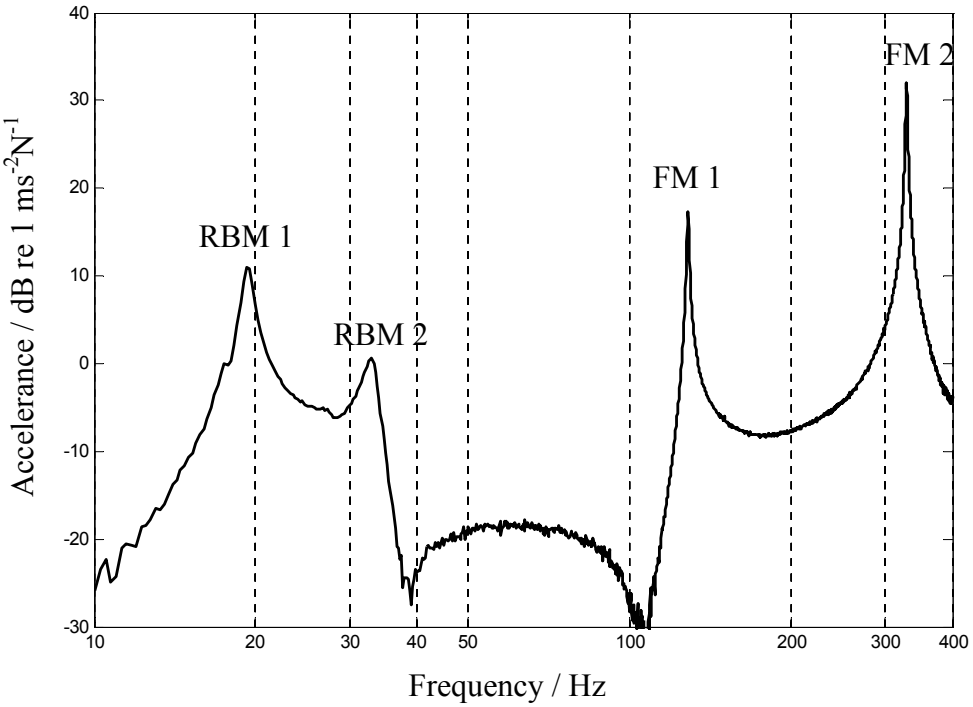

Figure 2.8. Measured Frequency Response Function of the experimental beam without shakers. An instrumented hammer was used to excite the structure and the acceleration was measured using an accelerometer mounted on the beam. The figure shows the translational rigid body mode (RBM 1), the rotational rigid body mode (RBM 2) and the first two flexural modes (FM1 and FM2).

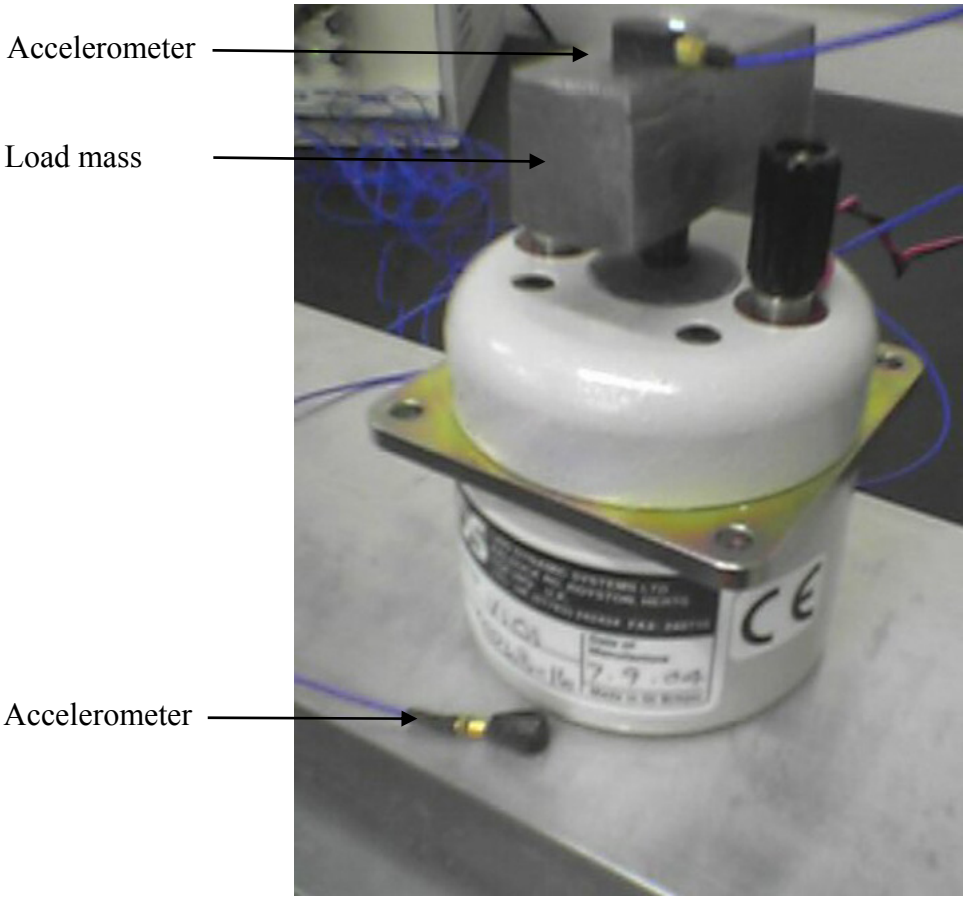

Figure 2.9. Ling Dynamic Systems V101 shaker with a load mass of 178g. An accelerometer was mounted on the load mass to measure the acceleration of the load mass. During the experimental set-up phase, another accelerometer was positioned on the beam adjacent to the shaker and was used as a comparison with the accelerometer on the load mass.

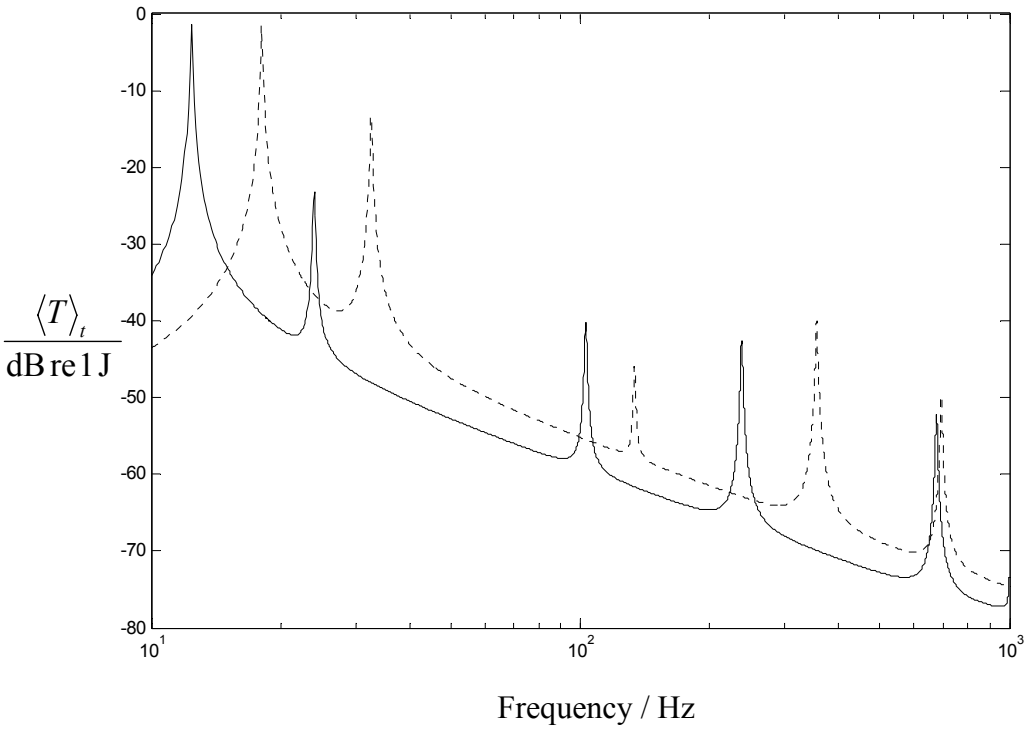

Figure 2.10. Simulations of the time averaged kinetic energy of the beam showing the effect of the extra mass due to the shakers. The beam is driven by three point forces of the same magnitude and phase at $x/l = 0.08$, $x/l = 0.33$ and $x/l = 0.66$. The solid line is a simulation using external masses equivalent to Ling Dynamic System V101 shakers where each mass = 0.91 kg. The dotted line is a simulation where no external masses are present on the beam.

3 Control by synchrophasing

3.1 Introduction

This chapter elaborates on the requirement that, for the types of generalised elastic structures of interest in this thesis, it is not be possible to alter the magnitude of the unbalance forces due to any harmonic vibrating sources that are applied to the structure. Hence control can only be achieved by altering the phases of the unbalanced forces with respect to each other.

The aim of this chapter is to derive expressions for a measureable quantity, whose magnitude changes in response to changes in the phases of the unbalance forces. Methods of finding the minimum of that quantity are then developed and described.

In order to quantify the effectiveness of control, two cost functions are introduced. Expressions are derived for these cost functions, the first of which determines the overall time averaged kinetic energy of the structure, and the second of which is the sum of the squares of the magnitudes of the velocity of the structure over each resilient mounting point. Two methods of determining the minimum of these cost functions are then described and compared. Their ease of application and ability to find the overall global minimum are considered. The chapter concludes by describing the fundamental difference between control when only two vibrating sources are present and control when more than two sources are present.

3.2 Choice of Cost Function to minimise

It is necessary to choose a system parameter that can be adjusted in order to provide a measure of the effect of the applied control. Suitable parameters should be real and any time dependence averaged over a cycle. It is possible to optimise the performance of the control system to either control the global vibration of the structure, in which case vibration at all points on the structure are regarded as equally important, or the control can be localised to certain important points on the structure. An example of such

positions would be where the structure is attached to its surroundings, as this would be expected to be an important path for vibration. A suitable quantity for investigating global control is the time averaged kinetic energy of the structure. The vibrational energy E of a structure vibrating in flexure is the sum of the elastic strain energy U due to the structure flexing, and the kinetic energy T due to the velocity response of the structure, given by

$$E = U + T \tag{3.1}$$

Without loss of generality, the specific example of a thin beam as described in Chapter 2 is considered. It lies along the x axis between x=0 and x=L and flexes in a direction parallel to the y axis. The instantaneous elastic strain energy for such a beam in flexure is given by [65]

$$U = \frac{1}{2}\int_0^L E_y I(x)\left(\frac{\partial^2 w(x,t)}{\partial x^2}\right)^2 dx \tag{3.2}$$

where E_y is the Youngs modulus and $I(x)$ is the second moment of area of the beam cross section about the neutral axis. The instantaneous kinetic energy T is given by [1, 65]

$$T = \frac{1}{2}\int_0^L \rho A(x)\left(\frac{\partial w(x,t)}{\partial t}\right)^2 dx \tag{3.3}$$

Where ρ and $A(x)$ are the mass density and the cross sectional area of the beam respectively. Since the instantaneous strain energy shown in Equation (3.2) contains the second partial derivative of the flexural displacement $w(x,t)$ with respect to x, U does not contain any contributions from the rigid-body modes of the structure. This is because displacement in the rigid body does not involve any flexure of the beam. Previous work [7] has shown that rigid-body modes are often an important source of

vibration for raft mounted machinery. Equation (3.3) shows that the kinetic energy depends upon the first partial derivative of the flexural displacement $w(x,t)$ with respect to t, so the kinetic energy does include contributions from the rigid-body modes. Thus the time averaged kinetic energy of the structure is considered to be a suitable cost function for investigating global vibration control.

To investigate the effect of local control, an alternative cost function is necessary. This cost function is the sum of the squares of the magnitudes of the velocities at the structure mounting points. The rationale for this choice is that, these points are where the vibrating structure is attached to any external structure and so this would be the path of vibration from the structure into the surroundings.

3.2.1 Minimising the time averaged kinetic energy of the structure

For a structure comprising $P+1$ machines, operating at identical speeds and causing harmonic vibration at angular frequency ω. The phases of P control machines at arbitrary positions given by $x_1 \cdots x_P$ can be adjusted relative to a reference machine at arbitrary position x_r as shown in Figure 3.1. The time averaged kinetic energy $\langle T(\omega) \rangle_t$ is given by [49]

$$\langle T(\omega) \rangle_t = \frac{\omega^2}{4} \left[\mathbf{q}_r f_r + \mathbf{Q}_c \mathbf{f}_c \right]^H \mathbf{M}_\mathbf{m} \left[\mathbf{q}_r f_r + \mathbf{Q}_c \mathbf{f}_c \right] \tag{3.4}$$

where the superscript H indicates the Hermitian transpose and $\mathbf{q}_r$ is the vector of modal amplitudes due to the machine for which the phase is not varied – the reference phase machine. For the n^{th} natural frequency ω_n of the structure to which the machines are attached, the modal amplitude due to a source at position x_r has the form

$$q_{r,n}(\omega) = \frac{W_n(x_r)}{m_{m,n}(\omega_n^2(1+j\eta) - \omega^2)} \tag{3.5}$$

where η is the structural loss factor of the beam, which is assumed to be constant across all of the modes, and W_n is the n^{th} mode shape of the beam at the position of the reference machine x_r. $\mathbf{M_m}$ is a square matrix of inertia coefficients, the n^{th} modal mass being given by $m_{m,n}$. $\mathbf{Q}_c$ is a rectangular (*N* modes x *P* sources) matrix of terms of the form

$$q_{n,p}(\omega) = \frac{W_n(x_p)}{m_{m,n}(\omega_n^2(1+j\eta)-\omega^2)} \tag{3.6}$$

which are proportional to the modal force contributions due to the control machine at position x_p and $\mathbf{f}_c$ is a vector of control forces given by

$$\mathbf{f}_c = f_r \begin{bmatrix} \lambda_1 e^{j\phi_1} \\ \lambda_2 e^{j\phi_2} \\ \vdots \\ \lambda_P e^{j\phi_P} \end{bmatrix} \tag{3.7}$$

where the magnitude and phase of the p^{th} control force, relative to the reference force f_r is given by $f_r\lambda_p e^{j\phi_p}$ where λ_p is a positive real number. The position of the reference force is given by coordinate x_r and the position of the p^{th} control force is at coordinate x_p for $p = 1 \ldots P$.

Equation (3.4) can be expanded so that the total time averaged kinetic energy of the system, considered as a sum over *N* modes, is given by

$$\left\langle T(\omega)\right\rangle_t = \frac{\omega^2\left|f_r\right|^2}{4}\left[\sum_{n=1}^{N}\frac{W_n^2(x_r)}{m_{m,n}\left|(\omega_n^2(1+j\eta)-\omega^2)\right|^2}+\sum_{p=1}^{P}\sum_{n=1}^{N}\frac{\lambda_p^2 W_n^2(x_p)}{m_{m,n}\left|(\omega_n^2(1+j\eta)-\omega^2)\right|^2}\right.$$

$$\cdots+2\sum_{p=1}^{P}\lambda_p\cos\phi_p\sum_{n=1}^{N}\frac{W_n(x_r)W_n(x_p)}{m_{m,n}\left|(\omega_n^2(1+j\eta)-\omega^2)\right|^2} \tag{3.8}$$

$$\left.\cdots+\sum_{t=1}^{P}\sum_{s=1}^{P}\lambda_t\lambda_s\cos(\phi_t-\phi_s)\sum_{n=1}^{N}\frac{W_n(x_s)W_n(x_t)}{m_{m,n}\left|(\omega_n^2(1+j\eta)-\omega^2)\right|^2}\quad \text{where}\,(s\neq t)\right]$$

The terms in the square bracket on the first line of Equation (3.8) are terms representing the time averaged kinetic energy if each machine alone is forcing the structure. As there is no phase dependence within these terms, their contribution to the total time averaged kinetic energy cannot be altered unless the magnitudes of the forces are changed.

The terms on the second line are phase dependent interaction terms between the reference machine and each of the P control machines. As each of these terms depend upon only one phase angle ϕ_p, they are decoupled from each other. As a consequence, the phase angle of each control machine can be independently adjusted to minimise the contribution made to the total time averaged kinetic energy from each term on the second line.

For the case of a single control machine $P=1$, and any single mode n, then using Equations (3.5) and (3.6), the phase dependent term on the second line can be written as $2\lambda_1\cos\phi_1\ q_{r,n}^*(\omega)\,q_{n,1}(\omega)$. Since $q_{r,n}^*(\omega)\,q_{n,1}(\omega)$ is real and can be either positive or negative, then the time averaged kinetic energy is minimised when $\cos\phi_1 = -1$ if $q_{r,n}^*(\omega)\,q_{n,1}(\omega)$ is positive and $\cos\phi_1 = 1$ if $q_{r,n}^*(\omega)\,q_{n,1}(\omega)$ is negative. From which the optimum control source phase angle is either $\phi_1=\pi$ or $\phi_1=0$ respectively.

The terms on the third line are interaction terms between the control machines. These terms can be seen to depend upon the difference between the phases of combinations of the pairs of the control machines (ϕ_t - ϕ_s) and the product of the magnitudes of the forces from the control machines (λ_t λ_s). In minimising the kinetic energy in each of the decoupled terms on the second line, the kinetic energy in the coupled terms on the third line may be increased.

A more practical method of calculating the time averaged kinetic energy - which does not require knowledge of the structural mode shapes - is to divide the structure into N_m mass 'elements' as shown in Figure 3.2. Each mass element comprises a proportion of the mass of the elastic structure and some elements contain a proportion of the mass of additional supported machinery. This formulation of the problem leads to a more practically useful form of Equation (3.4) given by

$$\langle T(\omega) \rangle_t = \frac{1}{4} \left(\mathbf{y}_r f_r + \mathbf{Y}_c \mathbf{f}_c \right)^H \mathbf{M} \left(\mathbf{y}_r f_r + \mathbf{Y}_c \mathbf{f}_c \right) \tag{3.9}$$

Where $\mathbf{y}_r$ is an $N_m \times 1$ vector of transfer mobilities between the reference machine and each of the mass elements shown in Figure 3.2 and given by

$$\mathbf{y}_r = \begin{bmatrix} y_{1,r} \\ \vdots \\ y_{n,r} \end{bmatrix} \tag{3.10}$$

where $y_{i,r}$ is the transfer mobility between the reference machine and the i^{th} mass element given by

$$y_{i,r} = \frac{\dot{w}_i}{f_r} \tag{3.11}$$

$\mathbf{Y}_c$ is an $N_m \times P$ matrix of transfer mobilities between the P control machines and the N_m mass elements. In this case $\mathbf{M}$ is an $N_m \times N_m$ diagonal matrix containing the mass of each element on the leading diagonal given by

$$\mathbf{M} = \begin{bmatrix} m_1 + \Delta M_p & 0 & 0 & 0 & 0 \\ 0 & m_2 + \Delta M_p & 0 & 0 & 0 \\ 0 & 0 & \ddots & 0 & 0 \\ 0 & 0 & 0 & m_{N_m-1} + \Delta M_p & 0 \\ 0 & 0 & 0 & 0 & m_{N_m} + \Delta M_p \end{bmatrix} \tag{3.12}$$

where $m_1 \cdots m_{N_m}$ represents the mass of each element of the elastic supporting structure and a proportion of the mass of each additional machine ΔM_p is included but can be equal to zero for some elements. Hence for the experimental determination of the time averaged kinetic energy, the transfer mobilities and the element masses must be known. Knowledge of the mode shapes of the structure is not required.

Simulations of the time averaged kinetic energy using Equation (3.9) were calculated using different numbers of element masses N_m and testing for convergence. This showed that at least five mass elements per flexural wavelength at the highest frequency were required to accurately determine the time averaged kinetic energy.

3.2.2 Expressions for minimising the sum of the moduli of the velocities squared over the mounting points

An alternative cost function which minimises the sum of the squares of the modulus of the velocity at S sensor positions over the mounting points given by $x_{s1} \cdots x_{sS}$ upon the thin beam structure is given by

$$J = \dot{\mathbf{w}}^H \dot{\mathbf{w}} \tag{3.13}$$

where $\dot{\mathbf{w}}$ is a vector of velocities at *S* positions on the structure given by

$$\dot{\mathbf{w}} = \begin{bmatrix} \dot{w}(x_{s1}) \\ \vdots \\ \dot{w}(x_{sS}) \end{bmatrix} \tag{3.14}$$

where the velocity at a general point upon the beam, given by *x*, takes the form

$$\dot{w}(x,\omega) = j\omega \sum_{n=1}^{N} W_n(x) \frac{f_r W_n(x_r) + \sum_{p=1}^{P} f_p W_n(x_p)}{m_{m,n}(\omega_n^2(1+j\eta) - \omega^2)} \tag{3.15}$$

Hence the velocity at each mounting point contains a contribution from each of the vibrating sources on the structure. Typically the velocity at each mounting point can be determined experimentally by placing accelerometers upon the structure at these points.

By re-writing $\dot{\mathbf{w}}$ in terms of the transfer mobilities and the applied forces

$$\dot{\mathbf{w}} = \begin{bmatrix} y_{1,r} \\ y_{2,r} \\ \vdots \\ y_{S-1,r} \\ y_{S,r} \end{bmatrix} f_r + \begin{bmatrix} y_{1,1} & y_{1,2} & \cdots & y_{1,P-1} & y_{1,P} \\ y_{2,1} & y_{2,2} & \cdots & y_{2,P-1} & y_{2,P} \\ \vdots & \vdots & \ddots & \vdots & \vdots \\ y_{S-1,1} & y_{S-1,2} & \cdots & y_{S-1,P-1} & y_{S-1,P} \\ y_{S,1} & y_{S,2} & \cdots & y_{S,P-1} & y_{S,P} \end{bmatrix} \begin{bmatrix} f_1 \\ f_2 \\ \vdots \\ f_{P-1} \\ f_P \end{bmatrix} = f_r \mathbf{y}_r + \mathbf{Y}\mathbf{f}_c \tag{3.16}$$

where $\mathbf{f}_c$ is given in Equation (3.7). Hence the cost function becomes

$$J = \left(\mathbf{y}_r f_r + \mathbf{Y}_c \mathbf{f}_c\right)^H \left(\mathbf{y}_r f_r + \mathbf{Y}_c \mathbf{f}_c\right) \tag{3.17}$$

It can be seen that both the cost functions defined by Equations (3.9) and (3.17) have the same form. The difference being that Equation (3.9) provides a mechanism for global control because all N_m mass elements of the structure are included, whilst Equation (3.17) provides local control at the *S* mounting points.

Synchrophasing control is achieved by adjusting the phase angles $\phi_1 \cdots \phi_P$ in the expression for $\mathbf{f}_c$ in Equation (3.7).

3.3 Methods of finding the minimum of the cost function

This section discusses methods of finding the control phases required to obtain the minimum value of the cost function. The cost function given in Equation (3.13) can be written as

$$J = \dot{\mathbf{w}}^H \dot{\mathbf{w}} = \sum_{s=1}^{S} \dot{w}_s^* \dot{w}_s \tag{3.18}$$

where $\dot{w}_s$ from Equation (3.15) is given by

$$\dot{w}_s = y_{s,r} f_r + \sum_{p=1}^{P} y_{s,p} f_p \tag{3.19}$$

Expanding Equation (3.18) and using $f_p = f_r \lambda_p e^{j\phi_p}$ gives

$$J = J_1 + J_2 + J_3 \tag{3.20}$$

where

$$J_1 = |f_r|^2 \sum_{s=1}^{S} \left[|y_{s,r}|^2 + \sum_{p=1}^{P} \lambda_p^2 |y_{s,p}|^2 \right] \tag{3.21}$$

$$J_2 = 2|f_r|^2 \sum_{s=1}^{S} \mathrm{Re}\left\{ y_{s,r} \sum_{p=1}^{P} \lambda_p y_{s,p}^* e^{-j\phi_p} \right\} \tag{3.22}$$

$$J_3 = 2|f_r|^2 \sum_{s=1}^{S} \left[\mathrm{Re}\left\{ \sum_{q=1}^{P-1} \lambda_q \sum_{p=q+1}^{P} \lambda_p y_{s,q}^* y_{s,p} e^{j(\phi_p - \phi_q)} \right\} \right]_{If\ P \neq 1} \tag{3.23}$$

Equation (3.23) is only included in the cost function when more than one control machine is present, i.e. $P > 1$. When $P = 1$ there are no interaction terms between the

phases of the control machines. The cost function defined in Equation (3.20) has stationary points when each of its P partial derivatives with respect to phase angles $\phi_1 \cdots \phi_P$ are equal to zero. These are given by

$$\frac{\partial J}{\partial \phi_p} = -2\left|f_r\right|^2 \lambda_p \sum_{s=1}^{S} \mathrm{Re}\left\{y_{s,r} y_{s,p}^* j e^{-j\phi_p}\right\} + \cdots$$
$$\cdots - \left[2\left|f_r\right|^2 \sum_{s=1}^{S}\sum_{q=1}^{P} \lambda_p \lambda_q \,\mathrm{Im}\left\{y_{s,q}^* y_{s,p} e^{j(\phi_p - \phi_q)}\right\}\right]_{\text{for q}\neq\text{p}} \tag{3.24}$$

Equation (3.24) shows that the stationary points for each ϕ_p depend upon the phase of the voltage supplied to each of the other $P-1$ control machines.

3.3.1 Synchrophasing with one control machine *P*=1

When synchrophasing with only one control machine such that P=1, Equation (3.20) becomes

$$J = J_1 + J_2 \tag{3.25}$$

where

$$J_1 = \left|f_r\right|^2 \sum_{s=1}^{S}\left[\left|y_{s,r}\right|^2 + \lambda_1^2 \left|y_{s,1}\right|^2\right] \tag{3.26}$$

and

$$J_2 = 2\left|f_r\right|^2 \lambda_1 \sum_{s=1}^{S}\left[\mathrm{Re}\left\{y_{s,r} y_{s,1}^* e^{-j\phi_1}\right\}\right] \tag{3.27}$$

Altering the phase of the single control machine ϕ_1 only affects the term J_2 of Equation (3.27). Hence the problem becomes one of minimising Equation (3.27). If $y_{s,r} y_{s,1}^*$ is written in terms of a magnitude and phase angle θ_s such that

$$y_{s,r} y_{s,1}^* = R_s e^{j\theta_s} \tag{3.28}$$

then the equation for J_2 can be written as

$$J_2 = 2\left|f_r\right|^2 \lambda_1 \sum_{s=1}^{S} R_s \cos(\theta_s - \phi_1) \tag{3.29}$$

It can be seen that to minimise the contribution to the cost function at each sensor requires $\cos(\theta_s - \phi_1) = -1$. Implying that $\theta_s - \phi_1 = (2n+1)\pi$ for $n = 0,1,2,3....$

However, the cost function is formed from the sum of the contributions from each sensor. Equation (3.27) can be written as

$$J_2 = 2\left|f_r\right|^2 \lambda_1 \mathrm{Re}\left\{\mathbf{y}_1^H \mathbf{y}_r e^{-j\phi_1}\right\} \tag{3.30}$$

where $\mathbf{y}_r$ is a vector of transfer mobilities between the reference machine and each sensor and $\mathbf{y}_1$ is a vector of transfer mobilities between the control machine and each sensor. These vectors are given by

$$\mathbf{y}_r = \begin{bmatrix} y_{1,r} \\ \vdots \\ y_{S,r} \end{bmatrix} \text{ and } \mathbf{y}_1 = \begin{bmatrix} y_{1,1} \\ \vdots \\ y_{S,1} \end{bmatrix} \tag{3.31}$$

If $\mathbf{y}_1^H \mathbf{y}_r$ is written in terms of a magnitude and phase in a similar way to Equation (3.28) so that

$$\mathbf{y}_1^H \mathbf{y}_r = R_1 e^{j\theta_1} \tag{3.32}$$

then the equation for J_2 can be written as

$$J_2 = 2\left|f_r\right|^2 \lambda_1 R_1 \cos(\theta_1 - \phi_1) \tag{3.33}$$

Hence to minimise J_2 across all sensors requires $\cos(\theta_1 - \phi_1) = -1$, implying that the minimising phase angle $\phi_{\min}$ is given by

$$\theta_1 - \phi_{\min} = (2n+1)\pi \text{ for } n = 0,1,2,3.... \tag{3.34}$$

The data that are required to achieve the minimisation are the transfer mobilities between each machine and each sensor. If these are obtainable, then θ_1 is known, hence the value of ϕ_1 corresponding to $\phi_{\min}$ can be calculated.

Also, the phase to maximise J_2 across all sensors requires $\cos(\theta_1 - \phi_1) = 1$. The value of ϕ_1 corresponding to $\phi_{\max}$ is given by

$$\theta_1 - \phi_{\max} = 2n\pi \text{ for } n = 0,1,2,3.... \tag{3.35}$$

Subtracting Equation (3.35) from Equation (3.34) gives

$$\phi_{\max} - \phi_{\min} = \pi \text{ for } n = 0,1,2,3.... \tag{3.36}$$

Equation (3.36) shows that the difference between the phase angle required to minimise the cost function and maximise it is 180°.

Figures 3.3 to 3.9 show simulations of synchrophasing with two vibrating sources mounted on the beam. The system properties used for the simulations are given in Table 3.1 below.

Beam	Length	1.2	m
	Width	101.6	mm
	Height	25.4	mm
	Thickness	3.2512	mm
	Young's Modulus	6.7×10^{10}	Pa
	Density	2710	kgm^{-3}
	Assumed flexural mode damping	5	%
Vibration Source	Mass	0.91	kg
Mounts	Stiffness	9×10^{3}	Nm^{-1}

Table 3.1. System properties used for simulations

For these simulations the reference phase source is positioned at $x/L = 0.08$ and the control source at $x/L = 0.33$. The magnitude of each force was the same and the minimum and maximum of the cost function was found by using a full search of all the angles.

Figure 3.3 shows a simulation of synchrophasing using the time averaged kinetic energy given in Equation (3.9) as the cost function to be minimised. For this cost function, the beam was considered to be split into twelve mass elements. The dotted line is the maximum time averaged kinetic energy of the beam and the solid line is the minimum. Figure 3.3 shows the two rigid-body modes - RBM 1 is the translational and RBM 2 is the rotational rigid-body mode respectively - and the first three flexural modes given by Equation (3.5) and labelled FM1-FM3 respectively. As can be seen from Figure 3.3, the time averaged kinetic energy in the first rigid body mode is reduced by approximately 30 dB by synchrophasing and the first flexural mode is reduced by approximately 25 dB. Figure 3.3 shows that the rotational rigid body mode is not well controlled for this configuration of sources. This is because the control source is positioned close to the node of the operational deflection shape at the frequency corresponding to the rotational rigid-body mode, so provides very little control. This is shown in Figure 3.5b where the control force f_1 is close to the node at $x/L = 0.32$.

Figure 3.4 shows the phase angle ϕ_1 of the control machine required to minimise the cost function shown in Figure 3.3. This figure shows that the optimum phase for minimising the cost function is usually either a 0° phase shift, so that the sources are vibrating in phase, or a 180° phase shift, so that the sources are vibrating in anti-phase. This is in agreement with Equation (3.34). Figure 3.3 also shows that no control is achieved at 80 Hz and Figure 3.4 shows that this is the frequency where the optimum phase for minimising the cost function changes from a 180° phase angle to a 0° phase angle with respect to the reference phase. This can be understood by considering the rigid body and flexural modes of a beam with free ends. Previous work on the rigid body modes of a thin beam with free end conditions [67, 68] has shown that for a force

applied to the beam on either of the intervals $\frac{x_r}{L} \leq \frac{1}{3}$ or $\frac{x_r}{L} \geq \frac{2}{3}$ then a node exists on the beam, so that application of a controlling force at or near that node will not be effective at reducing the overall cost function.

Figure 3.5a and Figure 3.5b show the translational and rotational rigid-body operational deflection shapes respectively for the compliantly mounted thin beam with two shakers on. The figures also show the positions of the reference and control forces at $x/L = 0.08$ and $x/L = 0.33$ respectively, which were used in the simulations. Figure 3.4 showed that to minimise the magnitude of vibration for the translational rigid body mode at 13 Hz, the control force is 180° out of phase with the reference force and this is shown by the direction of the arrow at $x/L = 0.33$ in Figure 3.5a. Figure 3.4 also showed that the control force is in phase with the reference force when minimising the magnitude of vibration of the rotational rigid body mode at 26.6 Hz, shown in Figure 3.5b. This is because there is a node of the mode shape at $x/L = 0.32$ which is between the two forces. If the two applied forces had been on the same side of the node, then the most effective phase for controlling vibration would be a 180° phase angle with respect to the reference phase. The rotational rigid body mode is not well controlled because the control source is very close to the node, so the time averaged kinetic energy is not greatly reduced at any control phase angle. The first flexural mode at 103 Hz is shown in Figure 3.5c and has nodes at $x/L = 0.2$ and $x/L = 0.725$ so there is a node of the first flexural mode between the two sources. To most effectively control this mode the control force should be in phase with the reference force, as is shown in Figure 3.4.

Figure 3.4 shows that for frequencies up to 70 Hz, the main modes excited are the rigid body modes and the optimum phase for the control force to reduce the cost function is 180° out of phase with the reference force. Above 80 Hz the first flexural mode becomes the most important and the most effective control is achieved with the control force in phase with the reference force. Between 70 Hz and 80 Hz the two main modes excited are the rotational rigid body mode and the first flexural mode. The cost function

reduction obtained by minimising one of these modes is cancelled out by a cost function increase in the other mode, so that the cost function is not significantly altered as can be seen in Figure 3.3.

Figure 3.6 shows a simulation of synchrophasing using Equation (3.17) as the cost function. This cost function minimises the sum of the magnitudes of the velocity squared at each end of the beam. The sources were in the same simulated positions as for Figure 3.3 and the figure shows that the translational rigid-body mode and the first flexural mode are well controlled by this cost function while the rotational rigid-body mode is not well controlled. The two cost functions are very similar in the effectiveness of their control at frequencies below the second flexural mode. Figure 3.7 shows the phase of the control machine required to minimise the cost function shown in Figure 3.6. This figure shows that the optimum phase for minimising the cost function is usually either a 0° phase shift, so that the sources are vibrating in phase, or a 180° phase shift, so that the sources are vibrating in anti-phase. This is in agreement with Equation (3.34).

Figure 3.7 shows that between 40 Hz and 70 Hz, the optimum phase angle changes from 180° to 0° in a smooth transition. Over this frequency range, the dominant mode is the rotational rigid body mode, although there is also some beam bending due to the first flexural mode. Figure 3.8 shows the simulated operational deflection shapes for the beam at 51 Hz when a phase shift is applied to the control source f_1. When both sources are in phase, as shown in Figure 3.8a, then the rotational rigid body mode is the dominant mode. The influence of the first flexural mode can be seen in Figures 3.8b to 3.8d, when the control source is phase shifted with respect to the reference source, as it causes a curve in the operational deflection shape. The cost function used in the simulations shown in Figures 3.6 and 3.7, minimised the sum of the magnitudes of the velocity squared at *each end* of the beam only, so the flexing can be used to minimise the velocity at each end of the beam. For the simulations shown in Figure 3.8 at 51 Hz, the cost function was minimised at 270°. Because only the ends of the beam are considered in the minimisation, comparison of Figures 3.8a and 3.8d, shows that the

displacement at the left hand end ($x = 0$ m) has decreased, whilst the displacement at the right hand end ($x = 1.2$ m) has increased, when the control source phase has a 270° shift with respect to the reference phase. In this case, the sum of the magnitude of the velocity squared at each end of the beam is lower for the 270° control source phase angle shown in Figure 3.8d.

The two cost functions are compared in Figure 3.9. The main difference between them is at frequencies above the second flexural mode. The figure shows that the cost function which minimises the sum of the magnitudes of the velocity squared – J in the figure and Equation (3.17) - more closely resembles the time averaged kinetic energy cost function as the number of sensor points along the beam increases. Both the cost functions have a very similar form, as shown in Equations (3.9) and (3.17). So as the number of sensor positions included in the determination of the cost function increases, so the cost function for local control more closely resembles the cost function for global control.

3.3.2 Synchrophasing with two control machines *P*=2

When $P = 2$, such that control is achieved by adjusting the two phase angles ϕ_1 and ϕ_2, Equation (3.20) becomes

$$J = J_1 + J_2 \tag{3.37}$$

where

$$J_1 = |f_r|^2 \sum_{s=1}^{S} \left[|y_{s,r}|^2 + \lambda_1^2 |y_{s,1}|^2 + \lambda_2^2 |y_{s,2}|^2 \right] \tag{3.38}$$

and

$$J_2 = 2|f_r|^2 \sum_{s=1}^{S} \left[\mathrm{Re}\left\{ y_{s,r} \lambda_1 y_{s,1}^* e^{-j\phi_1} + y_{s,r} \lambda_p y_{s,2}^* e^{-j\phi_2} \right\} + \mathrm{Re}\left\{ \lambda_1 \lambda_2 y_{s,1}^* y_{s,2} e^{j(\phi_2 - \phi_1)} \right\} \right] \tag{3.39}$$

It can be seen that Equation (3.38) is independent of the two control phases ϕ_1 and ϕ_2, so the control problem becomes one of minimising Equation (3.39) by adjusting phase

angles ϕ_1 and ϕ_2. The partial derivatives of Equation (3.39) with respect to ϕ_1 and ϕ_2 are given by

$$\frac{\partial J_2}{\partial \phi_1} = -2\left|f_r\right|^2 \sum_{s=1}^{S}\left[\mathrm{Re}\left\{\lambda_1 y_{s,r} y_{s,1}^* j e^{-j\phi_1}\right\} + \mathrm{Im}\left\{\lambda_1\lambda_2 y_{s,2}^* y_{s,1} e^{j(\phi_1-\phi_2)}\right\}\right] \tag{3.40}$$

$$\frac{\partial J_2}{\partial \phi_2} = -2\left|f_r\right|^2 \sum_{s=1}^{S}\left[\mathrm{Re}\left\{\lambda_2 y_{s,r} y_{s,2}^* j e^{-j\phi_2}\right\} + \mathrm{Im}\left\{\lambda_1\lambda_2 y_{s,1}^* y_{s,2} e^{j(\phi_2-\phi_1)}\right\}\right] \tag{3.41}$$

Using a similar notation to Equation (3.32), which is repeated here for convenience

$$\mathbf{y}_1^H \mathbf{y}_r = R_1 e^{j\theta_1} \tag{3.32}$$

The magnitude and phase of the vector products $\mathbf{y}_2^H \mathbf{y}_r$ and $\mathbf{y}_1^H \mathbf{y}_2$ are given by

$$\mathbf{y}_2^H \mathbf{y}_r = R_2 e^{j\theta_2} \tag{3.42}$$

$$\mathbf{y}_1^H \mathbf{y}_2 = R_3 e^{j\theta_3} \tag{3.43}$$

Hence the expressions for the derivatives become

$$\frac{\partial J_2}{\partial \phi_1} = 2\left|f_r\right|^2\left[\lambda_1 R_1 \sin(\theta_1 - \phi_1) + \lambda_1\lambda_2 R_3 \sin(\theta_3 + \phi_2 - \phi_1)\right] \tag{3.44}$$

$$\frac{\partial J_2}{\partial \phi_2} = 2\left|f_r\right|^2\left[\lambda_2 R_2 \sin(\theta_2 - \phi_2) - \lambda_1\lambda_2 R_3 \sin(\theta_3 + \phi_2 - \phi_1)\right] \tag{3.45}$$

Equations (3.44) and (3.45) show that the value of the partial derivatives, which define the way in which the cost function is minimised with respect to a particular control machine phase angle, depends not only upon that control phase angle, but also on the phase angle of the other control machine.

For $P>1$ there is no simple expression which relates the transfer mobilities between the structure mounted machinery and the sensors to the optimum choice of control phase angle, as there was when $P=1$ in Equations (3.33) and (3.34). This is because of the interaction terms which exist between the phases of the control machines, as shown in Equation (3.23) and the last expression in Equation (3.39). Instead, it is necessary to resort to a strategy which searches through a range of phase angles for each control machine, and calculates the optimum values of the control phases, by finding the global minimum of the *P* dimensional function, if one exists.

Figure 3.10 shows a cost function surface obtained by calculating the time averaged kinetic energy of the beam when 3 vibrating sources are present (*P*=2), as shown in Equations (3.38) and (3.39). Control is achieved by altering the phases of the two control sources ϕ_1 and ϕ_2. For this simulation the reference source was at $x_r/L=0.16$ and the two control sources were at $x_1/L=0.08$ and $x_2/L=0.33$ respectively. The frequency chosen was 100 Hz, which is close to the first flexural mode of the beam. Figure 3.10 shows that there is a clear minimum in the cost function, in this case when ϕ_1 and ϕ_2 are both 180° with respect to the reference phase machine.

A single clear minimum in the cost function is not always obtained. Figure 3.11 shows a simulation of the time averaged kinetic energy cost function surface for a different frequency and configuration of the sources. In this figure the reference source was at $x_r/L=0.33$ and the two control sources were at $x_1/L=0.08$ and $x_2/L=0.75$ respectively. The frequency was 10 Hz (*kl*=1.35). Figure 3.11 shows that more than one clear local minimum can exist in the cost function surface and that the optimum phase angles for the control sources are not always 0° or 180°. In this case there is symmetry in surface of the cost function through the plane $\phi_1=\phi_2$. This symmetry was investigated experimentally and is discussed further in Chapter 4. The cost function surface minimum in this simulation was given by $\phi_1=228^\circ$ and $\phi_2=118^\circ$.

3.3.3 Full Search

The simplest search strategy is that of stepping through the phase of each control source from 0° to 360° in suitable steps for each operating frequency of interest. This type of searching in a practical implementation of synchrophasing, can be very time consuming, as it is necessary to adjust the phase of one control machine, let the vibration settle to its steady state, then calculate the cost function *J,* repeating this process over a range of angles.

The number of measurements required at each frequency is $(360/N)^P$ for an N° step size and P control machines. Even a crude search over 10° steps of two control machines would take 1296 measurements. As the number of control machines P increases, the number of measurements required increases as 36^P for a step size of 10°.

For some situations, the time required may not be an important factor, and a full search might be the best and simplest option. A full search will detect the global minimum in cost function surfaces where there is more than one local minimum. But for other situations, for example an adaptive synchrophasing system where the phase of the control machinery changes in response to varying the machine loads, then the time to obtain the optimum phase angles may be more important.

A partial search strategy for $P=2$, based upon Equations (3.44) and (3.45) can be derived by noting that, at the global minimum, the partial derivatives given by Equations (3.44) and (3.45) are both equal to zero. It should be noted that they are also zero at other stationary points, such as maxima and saddle points. Summing Equations (3.44) and (3.45) gives

$$2|f_r|^2\left[\lambda_1 R_1 \sin(\theta_1-\phi_1)+\lambda_2 R_2 \sin(\theta_2-\phi_2)\right]=0 \tag{3.46}$$

from which

$$\sin(\theta_1-\phi_1)=-\frac{\lambda_2 R_2}{\lambda_1 R_1}\sin(\theta_2-\phi_2) \tag{3.47}$$

Since $\lambda_2 R_2 / \lambda_1 R_1$ is real and positive and θ_1 and θ_2 are constant whilst the machinery load remains constant, then for each step of ϕ_2, there are two corresponding values of ϕ_1 which satisfy Equation (3.47) and at which the value of the cost function can be calculated to search for the minimum. Hence, if $\lambda_2 R_2 / \lambda_1 R_1$, θ_1 and θ_2 are measurable quantities, the number of measurements of the cost function J required, reduces to $P \times 360/N$, for an N° step size, which is 2×36 for a step size of 10° with two control machines.

3.3.4 Application of Propeller Signature Theory

The time consuming part of the full search strategy is the time required to physically adjust the phase of each control machine, allow a suitable period of settling and then to make a measurement of the cost function. An alternative strategy, called Propeller Signature Theory [60] has been adopted in aircraft propeller noise and vibration studies [53-59, 61, 62, 71, 72]. It is based upon determining the transfer function between each machine on the elastic structure and each control sensor by physical measurement, and then using the transfer function data to run simulations of the effect of changing the phase angles on the value of the cost function. Instead of writing the vector of velocities at each sensor in terms of the transfer mobilities as shown in Equation (3.16) and given by

$$\dot{\mathbf{w}} = \begin{bmatrix} y_{1,r} & y_{1,1} & \cdots & y_{1,P} \\ y_{2,r} & y_{2,1} & \cdots & y_{2,P} \\ \vdots & \vdots & \ddots & \vdots \\ y_{S,r} & y_{S,1} & \cdots & y_{S,P} \end{bmatrix} \begin{bmatrix} f_r \\ f_1 \\ \vdots \\ f_P \end{bmatrix} \tag{3.48}$$

the mobility terms $y_{s,p}$ and the magnitudes of the forces applied by each vibrating machine source $|f_p|$ are incorporated into a term representing the transfer function between the vibrating machine and the control sensors, so that

$$\dot{\mathbf{w}} = f_r \begin{bmatrix} y_{1,r} & y_{1,1} & \cdots & y_{1,P} \\ y_{2,r} & y_{2,1} & \cdots & y_{2,P} \\ \vdots & \vdots & \ddots & \vdots \\ y_{S,r} & y_{S,1} & \cdots & y_{S,P} \end{bmatrix} \begin{bmatrix} 1 & 0 & 0 & 0 \\ 0 & \lambda_1 & 0 & 0 \\ 0 & 0 & \ddots & \vdots \\ 0 & 0 & \cdots & \lambda_P \end{bmatrix} \begin{bmatrix} 1 \\ e^{j\phi_1} \\ \vdots \\ e^{j\phi_P} \end{bmatrix} \tag{3.49}$$

becomes

$$\dot{\mathbf{w}} = \begin{bmatrix} \gamma_{1,r} & \gamma_{1,1} & \cdots & \gamma_{1,P} \\ \gamma_{2,r} & \gamma_{2,1} & \cdots & \gamma_{2,P} \\ \vdots & \vdots & \ddots & \vdots \\ \gamma_{S,r} & \gamma_{S,1} & \cdots & \gamma_{S,P} \end{bmatrix} \begin{bmatrix} 1 \\ e^{j\phi_1} \\ \vdots \\ e^{j\phi_P} \end{bmatrix} = \boldsymbol{\Gamma}\boldsymbol{\varphi} \tag{3.50}$$

where

$$\boldsymbol{\Gamma} = f_r \begin{bmatrix} y_{1,r} & y_{1,1} & \cdots & y_{1,P} \\ y_{2,r} & y_{2,1} & \cdots & y_{2,P} \\ \vdots & \vdots & \ddots & \vdots \\ y_{S,r} & y_{S,1} & \cdots & y_{S,P} \end{bmatrix} \begin{bmatrix} 1 & 0 & 0 & 0 \\ 0 & \lambda_1 & 0 & 0 \\ 0 & 0 & \ddots & \vdots \\ 0 & 0 & \cdots & \lambda_P \end{bmatrix} \tag{3.51}$$

The simplest way of determining the coefficients in the transfer function matrix $\boldsymbol{\Gamma}$ is to switch all of the machines off, and then switch each on in turn, which will give the contribution at each control sensor from each machine. As a consequence the columns of the transfer function matrix $\boldsymbol{\Gamma}$ are determined.

There are many situations where the machinery is critical and cannot be switched off in this fashion. In this case, the transfer function can be determined by introducing a known phase shift ψ onto each control machine in turn and obtaining a vector of velocities at each sensor position for each independent angle ψ. This is given by

$$\begin{bmatrix} \dot{w}_1(x_1) & \dot{w}_2(x_1) & \cdots & \dot{w}_{P+1}(x_1) \\ \dot{w}_1(x_2) & \dot{w}_2(x_2) & \cdots & \dot{w}_{P+1}(x_2) \\ \vdots & \vdots & \ddots & \vdots \\ \dot{w}_1(x_S) & \dot{w}_2(x_S) & \cdots & \dot{w}_{P+1}(x_S) \end{bmatrix} = \begin{bmatrix} \gamma_{1,r} & \gamma_{1,1} & \cdots & \gamma_{1,P} \\ \gamma_{2,r} & \gamma_{2,1} & \cdots & \gamma_{2,P} \\ \vdots & \vdots & \ddots & \vdots \\ \gamma_{S,r} & \gamma_{S,1} & \cdots & \gamma_{S,P} \end{bmatrix} \begin{bmatrix} 1 & 1 & 1 & 1 \\ 1 & e^{j\psi_1} & 1 & 1 \\ 1 & 1 & \ddots & 1 \\ 1 & 1 & 1 & e^{j\psi_P} \end{bmatrix} \quad (3.52)$$

$S \times (P+1)$ $\quad$ $S \times (P+1)$ $\quad$ $(P+1) \times (P+1)$

where $\psi_1 \cdots \psi_P$ are the known phase shifts applied to each control machine in turn. Equation (3.52) can be written using matrix notation as

$$\dot{\mathbf{W}} = \mathbf{\Gamma\Psi} \quad (3.53)$$

For a fully determined solution on a system comprising P control machines and one reference machine, (P+1) physical measurements of the vector of velocities $\dot{\mathbf{w}}$ at independent phase angles are required. These measurements form the columns of the matrix $\dot{\mathbf{W}}$ in Equation (3.52). If more measurements are made at independent phase angles than there are control machines, then a least squares determination of $\mathbf{\Gamma}$ can be obtained by

$$\mathbf{\Gamma} = \dot{\mathbf{W}}\mathbf{\Psi}^T \left[\mathbf{\Psi}\mathbf{\Psi}^T\right]^{-1} \quad (3.54)$$

Once the transfer function matrix $\mathbf{\Gamma}$ has been determined, its elements are independent of the phase angle chosen for the control machines. As long as the machine loads do not change, $\mathbf{\Gamma}$ can be regarded as a constant matrix. This allows the determination of the optimum synchrophase angles for each of the control machines to be achieved by simulation, using the elements determined for the transfer function matrix $\mathbf{\Gamma}$ in a full search, using a mathematical package such as MATLAB®. Hence only P changes of phase angle are required, as the first measurement is likely to be with none of the phases altered, as is shown in the first column of matrix $\mathbf{\Psi}$ in Equation (3.52). The cost function can then be expressed in terms of the transfer function matrix and the vector of phases of the sources as

$$J = \dot{\mathbf{w}}^H \dot{\mathbf{w}} = \boldsymbol{\varphi}^H \boldsymbol{\Gamma}^H \boldsymbol{\Gamma} \boldsymbol{\varphi} \tag{3.55}$$

This method is considerably faster than a full search because only P changes of phase angle are required. So only 2 phase changes are necessary rather than the 1296 in the full search example given in subsection 3.3.3.

3.4 Conclusions

This chapter has developed expressions for two cost functions, which were used to provide a measure of the effectiveness of vibration control when the phase angles of the forces applied to a thin beam were adjusted. The two cost functions used were

- Global control by considering the time averaged kinetic energy of the structure.

- Local control by considering the sum of the squares of the magnitudes of the velocities at the structure mounting points.

As the number of sensor positions included in the local control cost function increases, so it more closely resembles the cost function for global control.

When only two vibrating sources are present on the structure, vibration control can be achieved by altering the phase of the single control machine. The best phase angle for the control machine is often just either in phase, or in anti-phase with respect to the reference machine, depending upon the positions of the machines upon the structure, the positions of the nodes of the dominant modes of vibration that are excited at the frequency of interest and the magnitude of the modal forces.

For a structure supporting more than two vibrating machines, the coupled interaction terms that contribute to the cost function can work ‘against each other’ depending upon their magnitudes, so that no simple analytical expression for the optimum synchrophase angles exists. The optimum phase angle for each control machine to take, in order to

minimise the cost function, is not as intuitive as the two machine case. A single well defined minimum of the cost function may not always be obtained because local minima or symmetric minima may exist on the cost function surface.

Two methods of finding the minimum of the cost function have been discussed. Both methods require a stepped search through all of the phase angles, but while one method physically steps through the phase of each machine whilst it is running, the other method simulates stepping through the angles using phase independent transfer functions that are determined by measurements. The former method, although simplistic, can be very time consuming as it is required to physically adjust the phase of each control machine, allow a suitable period of settling and then to make a measurement of the cost function. The latter method, also known as Propeller Signature Theory only requires the same number of independent phase changes as there are control machines. These phase changes are used to calculate the phase independent transfer function between each machine and each sensor position. A simulation is then run using the transfer functions to step through all of the phase angles to determine the minimum of the cost function. This was shown to be much faster than the Full Search method. This calculation of transfer function needs to be performed at each operating speed and hence frequency for which synchrophasing is to be applied.

3.5 Figures

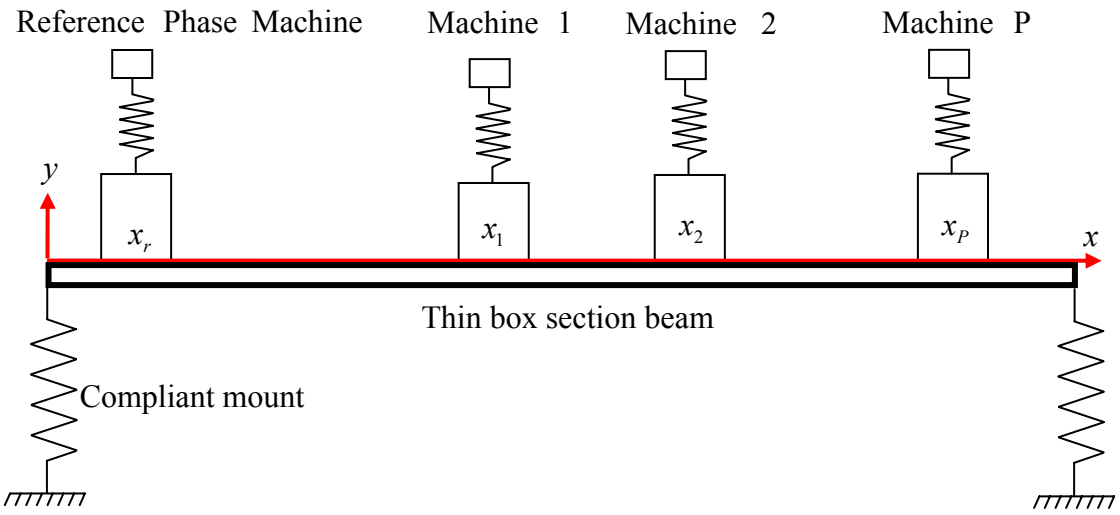

Figure 3.1. A thin box section beam supporting $P+1$ machines such that the phases of P control machines are adjusted relative to a reference machine. In the diagram P=3.

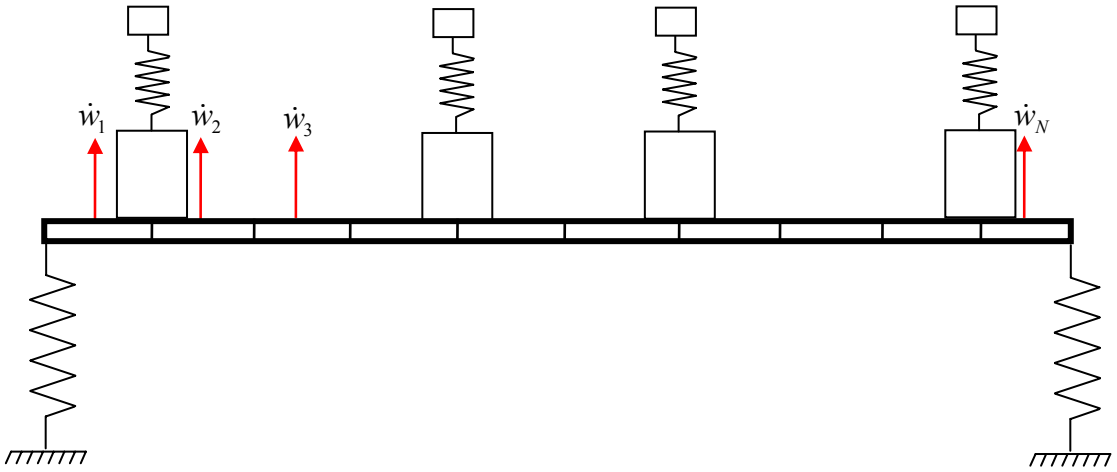

Figure 3.2. The elastic beam divided into N_m mass 'elements' some of which include a proportion of mass due to additional machinery. The velocity of each mass element is measured to calculate the time averaged kinetic energy.

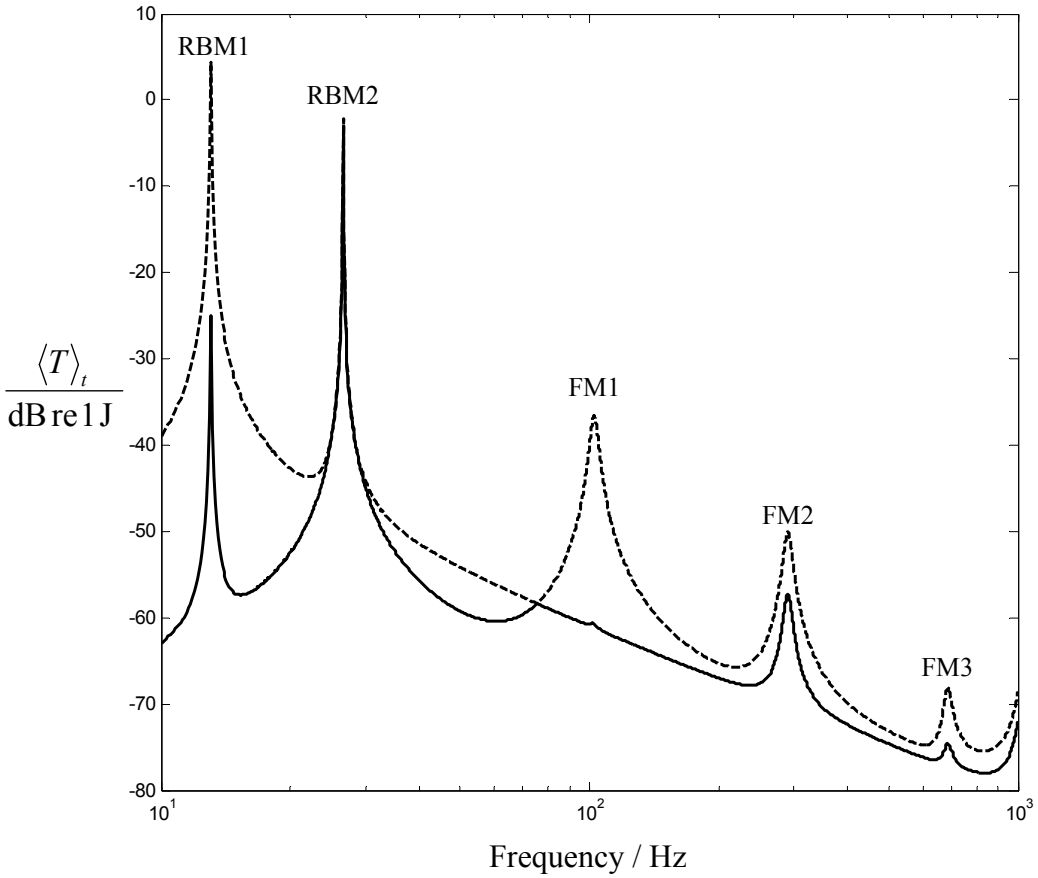

Figure 3.3. Simulations of synchrophasing using the time averaged kinetic energy as the cost function. For the simulations two vibrating sources were mounted on the beam, one reference source at $x_r/L = 0.08$ and one control source at $x_1/L = 0.33$. The figure shows the maximum kinetic energy of the beam (dotted) and the minimum kinetic energy of the beam (solid) achieved by synchrophasing one control source. RBM1 is the translational and RBM2 is the rotational rigid body mode respectively. The first three flexural modes are labelled FM1-FM3 respectively.

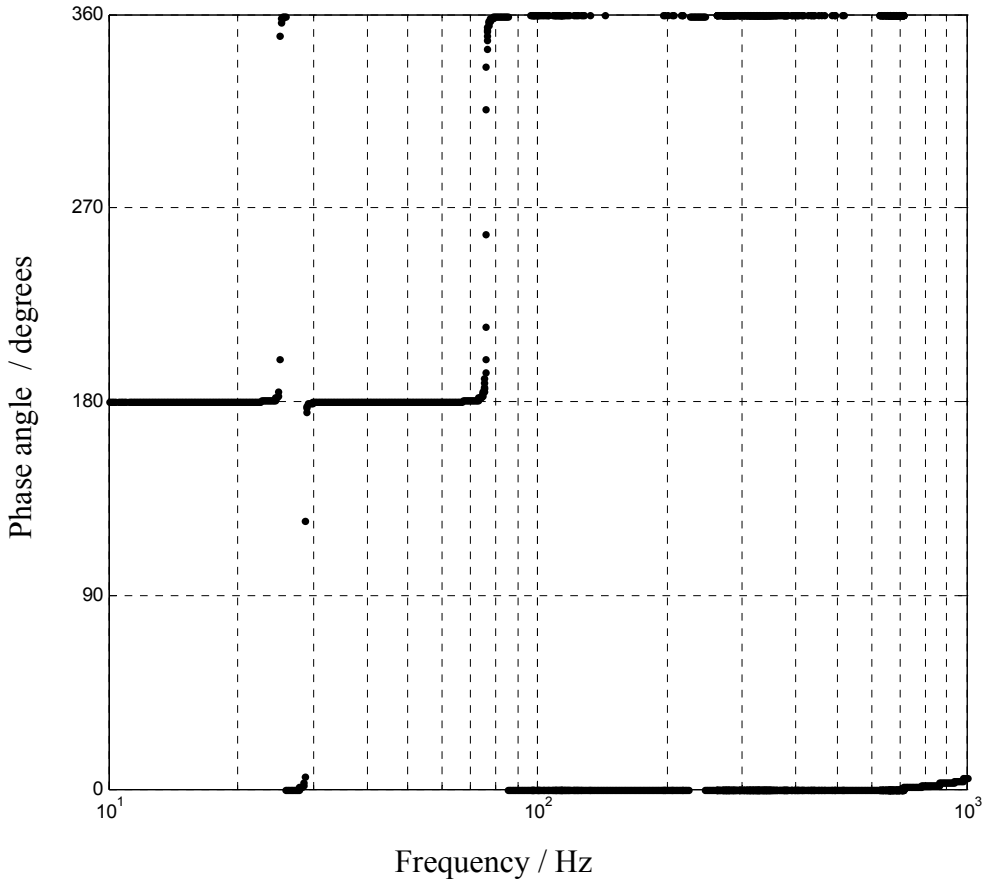

Figure 3.4. Phase ϕ_1 of the control machine required to minimise the time averaged kinetic energy. For the simulation, two vibrating sources were mounted on the beam, one reference source at $x_r/L = 0.08$ and one control source at $x_1/L = 0.33$.

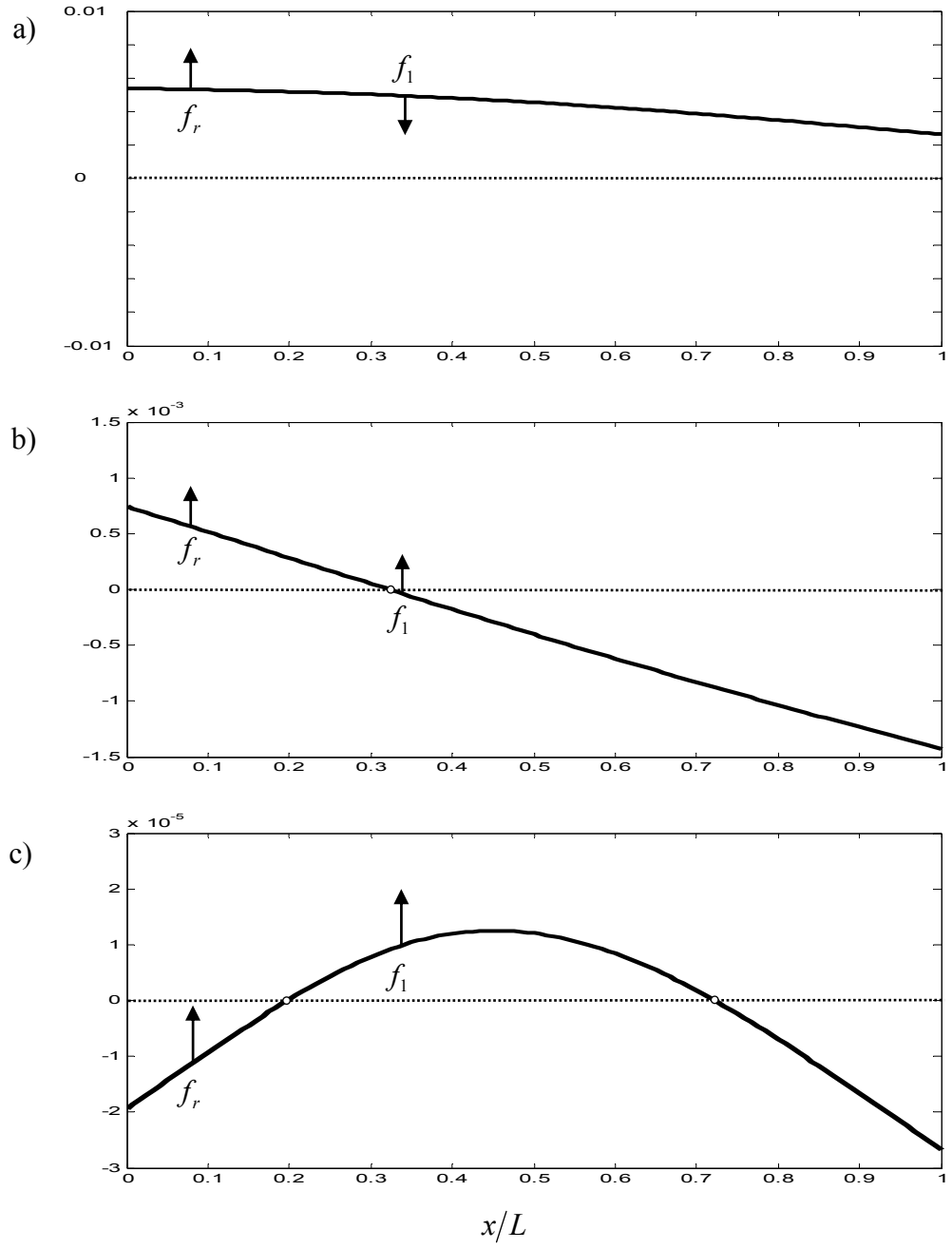

Figure 3.5. The first three simulated operational deflection shapes for the compliantly mounted thin beam with two shakers on. a) translational rigid-body modeshape, b) rotational rigid-body modeshape with a node at $x/L = 0.32$ and c) first flexural modeshape with nodes at $x/L = 0.2$ and $x/L = 0.725$. The positions of the reference source at $x/L = 0.08$ and the control source at $x/L = 0.33$ used in generating the simulations are shown on the modeshapes.

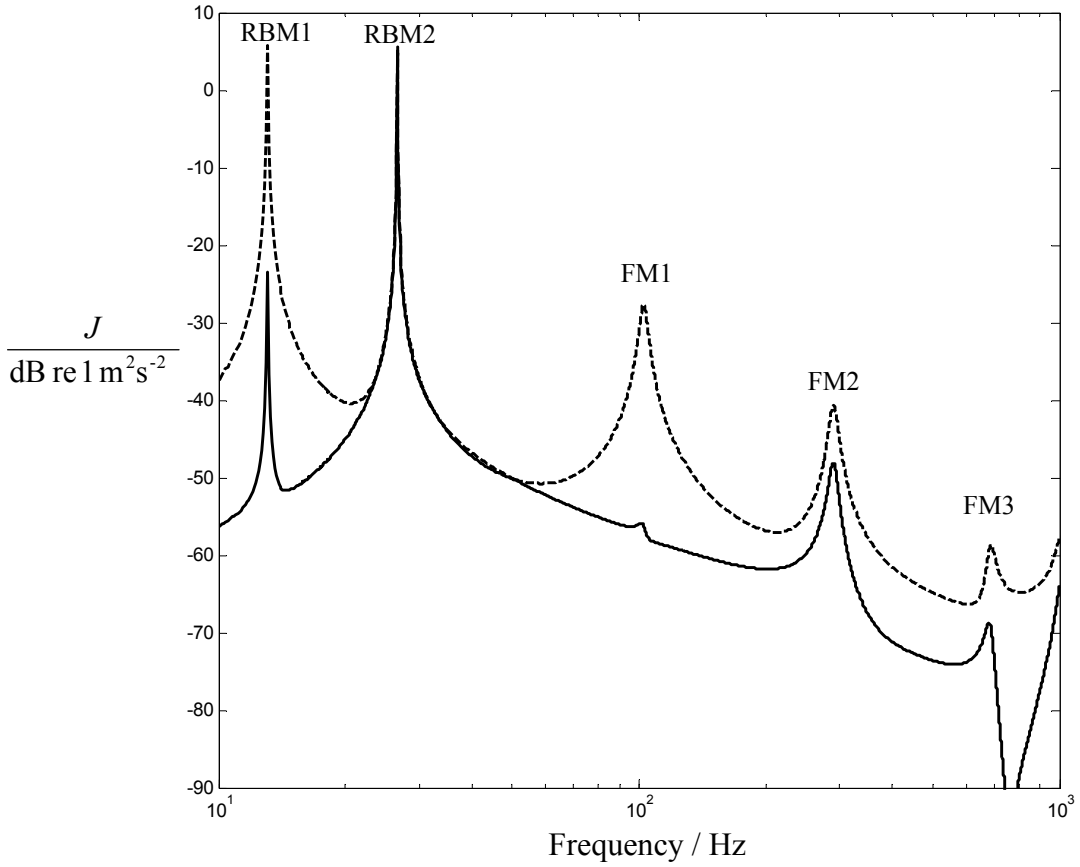

Figure 3.6. Simulations of synchrophasing using the sum of the magnitudes of the velocity squared at each end of the beam as the cost function. For the simulations two vibrating sources were mounted on the beam, one reference source at $x_r/L = 0.08$ and one control source at $x_1/L = 0.33$. The figure shows the maximum cost function (dotted) and the minimum (solid) achieved by synchrophasing one control source. RBM1 is the translational and RBM2 is the rotational rigid body mode respectively. The first three flexural modes are labelled FM1-FM3 respectively.

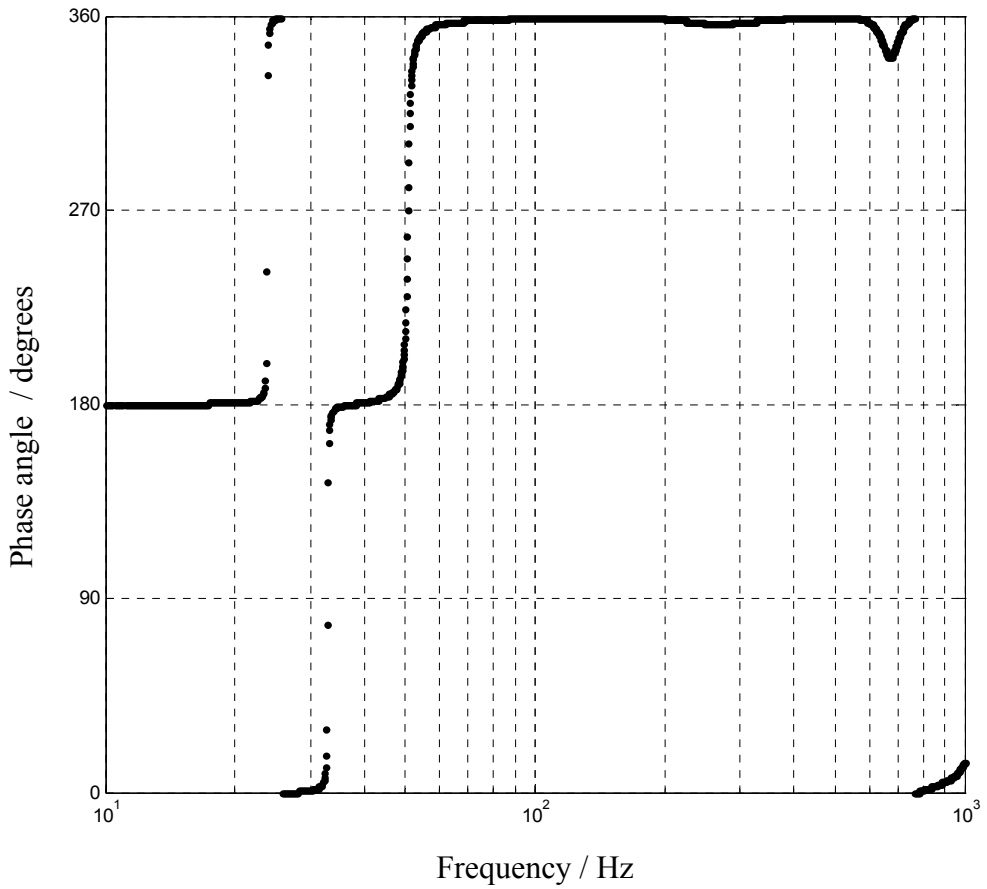

Figure 3.7. Phase ϕ_1 of the control machine required to minimise the sum of the magnitudes of the squared velocities at each end of the beam as the cost function. For the simulation, two vibrating sources were mounted on the beam, one reference source at $x_r/L = 0.08$ and one control source at $x_1/L = 0.33$.

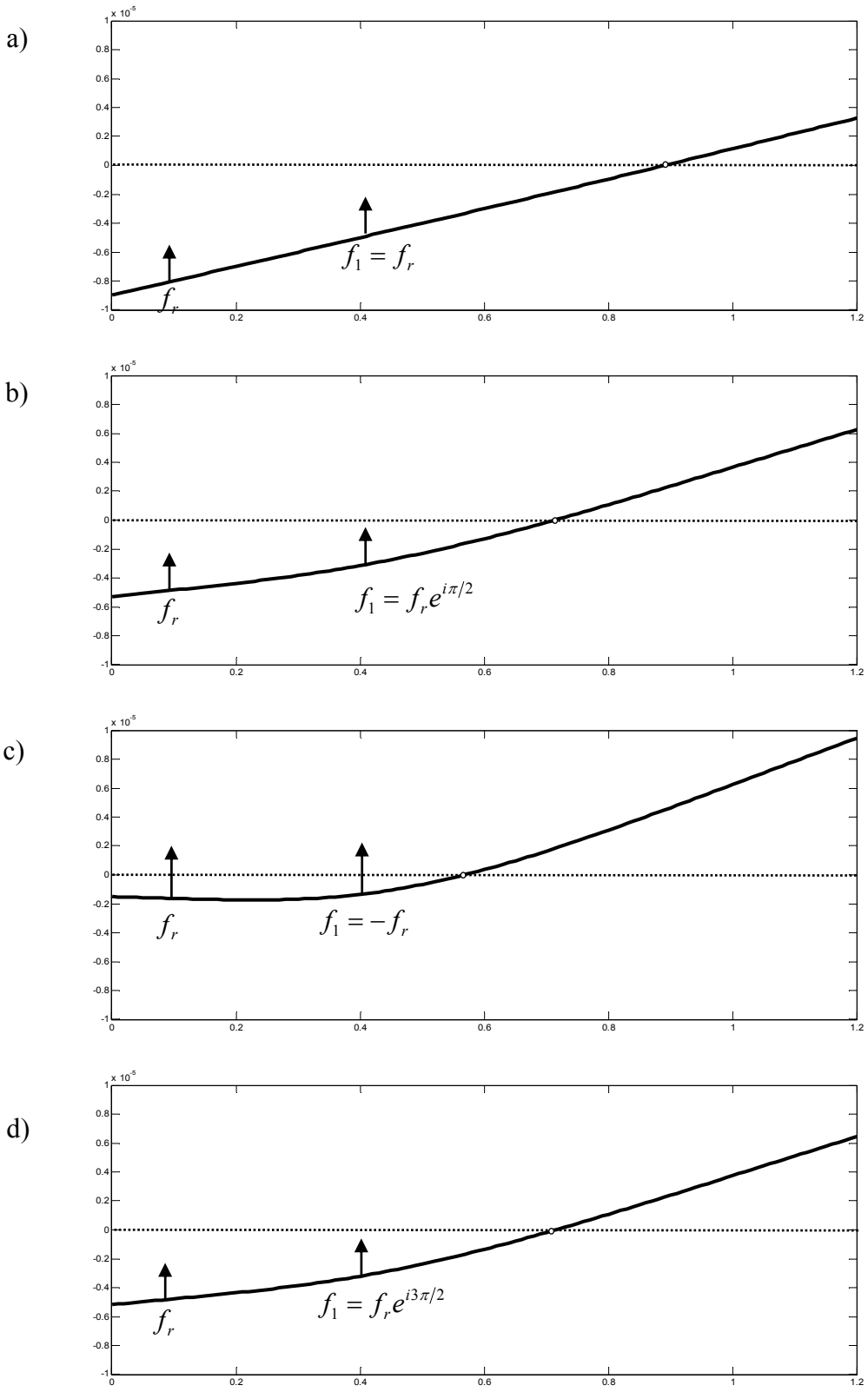

Figure 3.8. Simulated operational deflection shapes at 51 Hz. The control source f_1 has a phase shift of a) 0° b) 90° c) 180° d) 270° with respect to the reference phase f_r

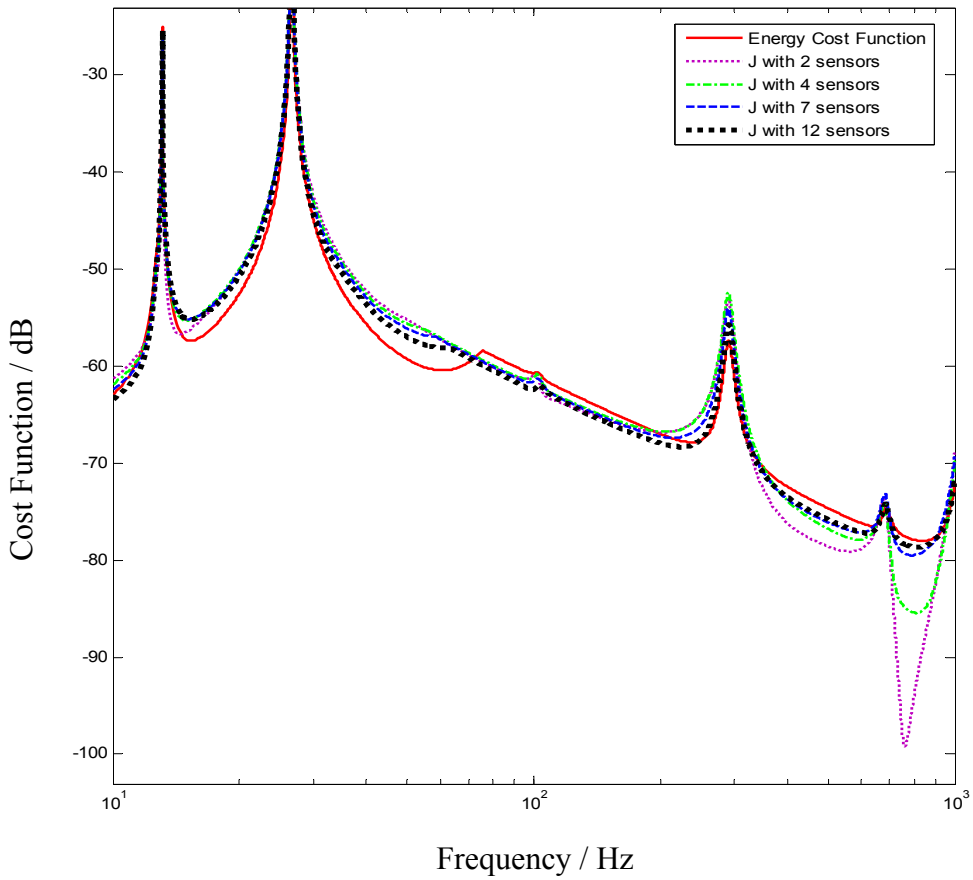

Figure 3.9. Comparison of the cost functions which minimise the time averaged kinetic energy and the sum of the magnitude of the velocity squared *J*, at selected points along the beam. The number of points selected is adjusted from one at each end of the beam then 4, 7 and 12 equi-spaced points. For the simulation two vibrating sources were mounted on the beam, one reference source at $x_r/L = 0.08$ and one control source at $x_1/L = 0.33$.

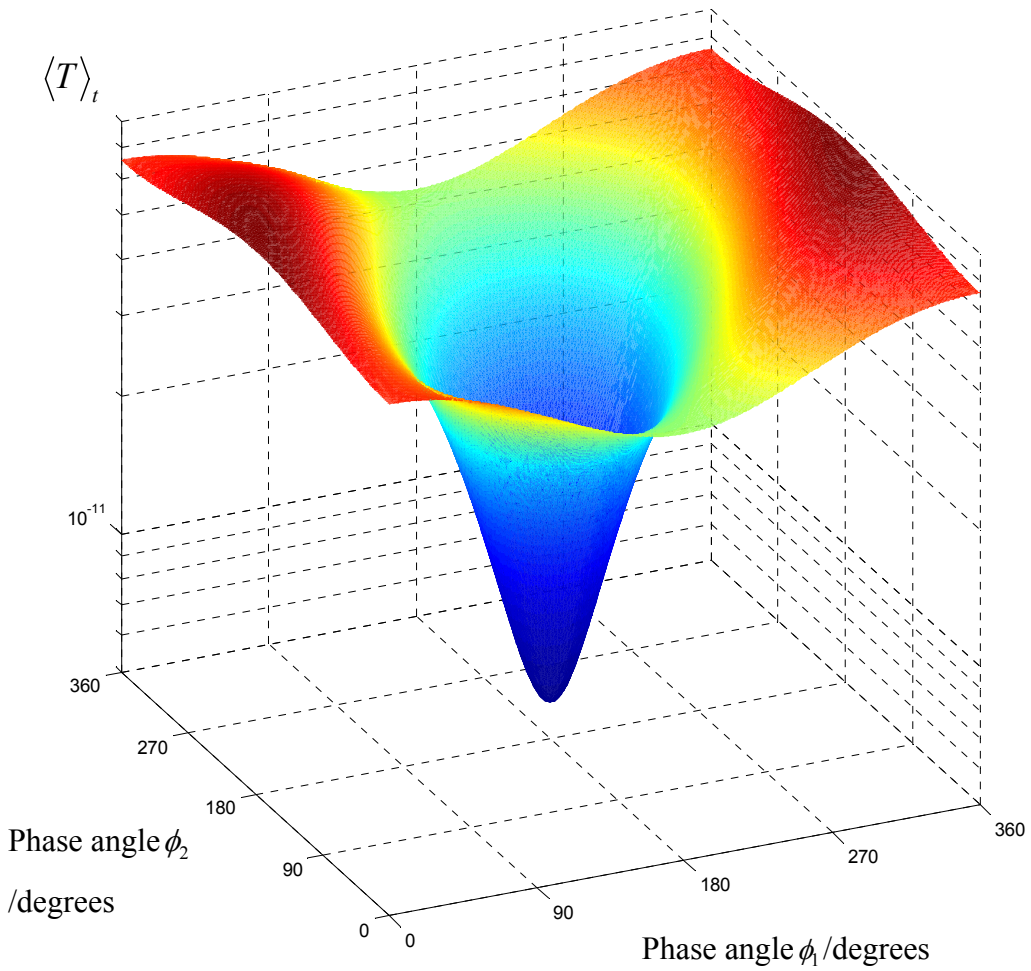

Figure 3.10. Cost function surface obtained using the time averaged kinetic energy of the beam as the cost function, with 3 vibrating sources on the beam (P=2). The plot was generated from a simulation, where the reference source was at $x_r/L = 0.16$ and the two control sources were at $x_1/L = 0.08$ and $x_2/L = 0.33$ respectively and the frequency was 100 Hz (kl=4.2).

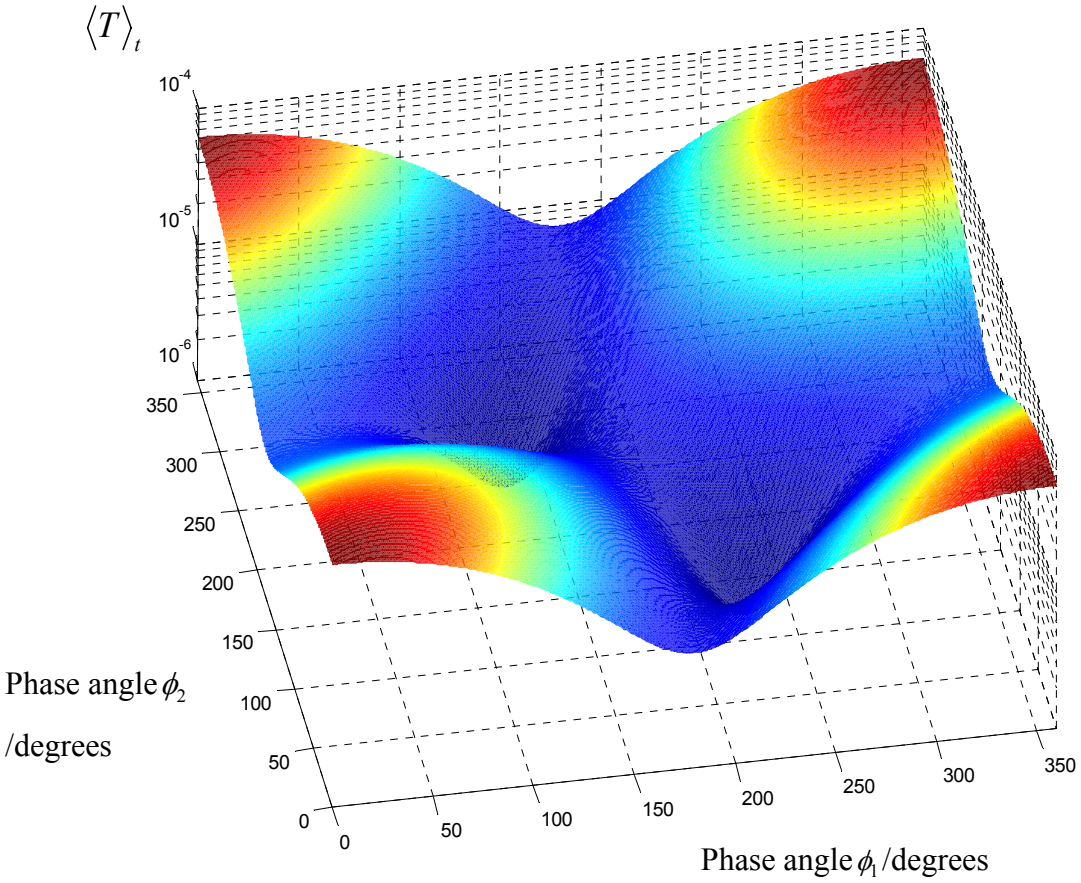

Figure 3.11. Cost function surface obtained using the time averaged kinetic energy of the beam as the cost function, with 3 vibrating sources on the beam (P=2). The plot was generated from a simulation, where the reference source was at $x_r/L = 0.33$ and the two control sources were at $x_1/L = 0.08$ and $x_2/L = 0.75$ respectively and the frequency was 10 Hz (kl=1.35).

4 Experimental validation of synchrophasing

4.1 Introduction

The aim of this chapter is to describe the experimental work conducted to validate the numerical simulations and subsequent conclusions presented in Chapter 3. The chapter begins with a description of a physical beam model which was used to investigate control of an elastic structure by synchrophasing. The vibration sources used in the experiments were electromagnetic shakers. Each shaker applied a force to the supporting beam as a result of a reaction against an attached mass load.

In order to assess the effectiveness of control, two cost functions were investigated experimentally. The cost functions were the measurement of the time averaged kinetic energy of the elastic structure, and the measurement of the sum of the squares of the magnitudes of the velocities at the structural mounting points of the beam. These cost functions were investigated using simulations in Chapter 3.

For the initial experiments with two electromagnetic shakers, both cost functions were investigated. For later experiments, only the cost function of minimising the sum of the squares of the magnitudes of the velocities at the beam support positions was used, as this was easier to implement experimentally. It would also be easier to fit into a practical synchrophasing scheme as it does not require any information regarding the mass distribution of the structure.

Methods for measuring the time averaged kinetic energy using a scanning laser vibrometer, and measuring the sum of the squares of the magnitude of the velocity at each end of the structure are described. A method for automating the calculation of the cost function in response to changes in the phase angles of the applied voltages is described and implemented using the software packages LABVIEW® and MATLAB®.

The experimental determination of the synchrophase angles revealed the power of the propeller signature theory technique. It enabled much faster calculation of the optimum

control angles for each of the vibrating sources. The results obtained are discussed and compared to those obtained from simulations.

4.2 Experimental Set-up

Figure 4.1 shows the system configuration used to investigate synchrophasing when two vibrating sources are mounted on an elastic platform. The physical properties of the system are given in Table 4.1.

Beam	Material	Aluminium 6063-T6 Extruded Box section	Units
	Length	1.2	m
	Width	101.6	mm
	Height	25.4	mm
	Thickness	3.2512	mm
	Young's Modulus[1]	6.7×10^{10}	Pa
	Density[1]	2710	kgm^{-3}
Shaker	Make	Ling Dynamic Systems	
	Model	V101	
	Mass	0.91	kg
	Load mass on shaker	0.178	kg
Mounts	Make	RLF High deflection rubber	
	Type	2	
	Stiffness[2]	9×10^{3}	Nm^{-1}

1 From manufacturer's data sheets
2 Measured by static loading

Table 4.1. Physical properties of experimental system

An aluminium box section beam was used as the flexible mounting platform. Its dimensions were chosen to provide separation between the two rigid-body modes of the system and the flexible modes of the beam. An initial modal analysis of the beam without

any shakers mounted on it was conducted using an instrumented hammer to excite the structure. This revealed rigid body modes at 19 Hz and 33 Hz, and the first two flexural modes at 130 Hz and 330 Hz. The beam was compliantly mounted at each corner using flexible rubber mounts.

A Polytec PSV400 scanning laser vibrometer was used to measure the velocity over a grid of positions covering the beam, as shown in Figure 4.2. The grid extended over 12 equispaced positions along the length of the beam and 3 positions across the width of the beam. The choice of the number of measurement positions along the length of the beam ensured that at least five points were measured per flexural wavelength at the highest frequency of interest, which was 1 kHz. Using the Euler-Bernoulli beam equation, also known as thin beam theory [1, 65] the bending wavelength λ_b is given by

$$\lambda_b = \frac{2\pi}{\sqrt{\omega}} \sqrt[4]{\frac{EI}{\rho A}} \tag{4.1}$$

where E is Young's modulus, I is the second moment of area of the beam cross-section about the neutral axis, ρ is the density, A is the cross sectional area and ω is the angular frequency of vibration. Using the data in Table 4.1 for the physical properties of the beam, for 1 kHz, $\lambda_b = 0.57$ m, so a grid spaced 0.1m apart was suitable.

For the comparison of cost functions, the 36 measured velocities were stored individually and post-processed using MATLAB®. The three positions across the beam were averaged, to try to reduce any contribution in the measured vibration due to the beam twisting, as only flexural vibration was of interest and included in the analytical model.

Figure 4.3 shows the experimental system configuration used to investigate synchrophasing when three vibrating sources are mounted on the elastic platform. The beam and mounts were the same as described previously and shown in Table 4.1. The cost function used for the experiments with three vibrating sources was to minimise the

sum of the squares of the magnitudes of the velocities over the mount points at each end of the structure. As a result, only the acceleration at each end was required. This was measured using accelerometers shown as A4 and A5. This cost function is more practically achievable in a real situation than the cost function which minimises the time averaged kinetic energy, because the structure doesn't need to be considered as a set of mass elements or as a distributed continuous system.

4.2.1 Electromagnetic shakers as vibrating sources

Ling Dynamic Systems V101 shakers were placed on the beam and used to vibrate test load masses. Thus a reaction inertial force was applied to the beam by each shaker. Accelerometers were used to measure the acceleration on the load masses; these are shown in Figures 4.1 and 4.3. These accelerations were used to infer the forces applied to the beam, this assumes that the acceleration measured by the accelerometer on the load mass is the same magnitude as that applied to the beam, i.e. that the shaker and load mass system resonance is out of the measurement range. The resonant frequency of the single degree of freedom, shaker load mass system is given by

$$f_r = \frac{1}{2\pi}\sqrt{\frac{k}{m}} \tag{4.2}$$

where k is the suspension axial stiffness of the electrodynamic shaker [73] $k = 3.15\times10^3\,\mathrm{Nm^{-1}}$ and $m = 0.18\,\mathrm{kg}$ is the mass of the load mass and the moving element of the shaker. Hence $f_r = 21\,\mathrm{Hz}$, which is between the two rigid body modes of the system and right at the bottom of the measurement range.

Figure 4.4 shows a block diagram of the measurement and control set up used for synchrophasing when three electrodynamic shakers were attached to the elastic beam. The shaker excitation waveforms were generated on the laptop computer within the LabView® software package. This enabled precise phases of waveforms to be generated with respect to the reference waveform. These waveforms were converted into voltages in the digital to analogue converter and then fed to the shakers via power amplifiers.

Although the phases of the signals generated by LabView® were known, the effect of any phase shifts due to the power amplifiers was not known. To mitigate for this, the phases attributed to each control signal was that measured by the accelerometer on the load mass for each shaker. The signals from each of the five accelerometers were conditioned and then fed to the analogue to digital converter then processed in LabView®. The three accelerometers on the load masses were used to determine the applied phases of the control voltages, whilst the signals from the two accelerometers at each end of the beam were used in the calculation of the cost function.

4.3 Experimental measurement techniques

For the set of measurements with two electrodynamic shakers present on the beam, the velocity at each of the 36 grid positions shown in Figure 4.2 was measured using a Polytec PSV400 scanning laser vibrometer. This enabled both the time averaged kinetic energy of the whole system and the magnitude of the velocity at each end of the beam to be determined; hence both methods could be assessed as control cost functions.

To calculate the total time averaged kinetic energy of the structure at each frequency, all twelve of the averaged velocities along the length of the beam were used, averaging the three velocity measurements across the beam to reduce the effects of beam twisting. To calculate this cost function also requires knowledge of the mass of the structure and the machinery mounted on the structure. For the cost function which minimises the sum of the squares of the magnitudes of the velocities at each end, only the averaged velocity at each end is required.

4.3.1 Using the transfer mobility to determine the local and global cost functions

In order to compare the vibration control possible using the global and local cost functions, two electrodynamic shakers were used on the beam. Rather than finding the minimum in the cost function by searching all of the phase angles, the transfer mobilities were measured using the experimental system, and then used in simulations

to find the maximum and minimum values of the cost function and hence calculate a measure of the success of control.

For the investigation with two electrodynamic sources, the beam was excited by a force $f(x_j)$ from each shaker in turn by applying a band limited pseudo random noise as the excitation. This gave the transfer mobilities between each shaker and each measurement point defined by

$$Y_{ij}(\omega) = \frac{\dot{w}(x_i, \omega)}{f(x_j, \omega)} \tag{4.3}$$

at each of the 36 measurement positions x_i along the beam, for each of the two shaker positions x_j given by x_1 and x_2 as shown in Figure 4.1, and where $\dot{w}(x_i, \omega)$ is the velocity of the beam at measurement position x_i and frequency ω. These mobilities were used in the way described in Section 3.3.1 to find the optimum value for the phase angle of the control source in order to minimise the cost function, and also to maximise the cost function.

4.3.2 Minimisation using a full search

A full search methodology was implemented for synchrophasing when three electrodynamic shakers were present upon the structure. The set up used for this series of experiments is shown in Figure 4.4.

LabView® programs were written to change the phase of the voltage applied to each control shaker in turn by a set increment. This increment could take any value, but was typically $1^\circ, 5^\circ$ or 10°. Once the system had settled to steady state conditions, the acceleration at each end of the beam was measured and the value of the cost function determined. Hence for the system comprising three vibrating sources, where two were subject to control, a cost function surface was generated. Once all the required angles

had been measured, the minimum of the cost function surface was determined automatically using LabView® and MATLAB® tools.

Figures 4.5 and 4.6 show the LabView® front panel used for a full search at a single frequency when three shakers were attached to the beam. Figure 4.5 shows the waveform parameters on the left hand side of the figure. At each phase angle increment, three waveforms of 40,960 samples each, at a sample rate of 8192 were generated by the computer and applied to each shaker. This gave a five second signal for each measurement of the cost function at each phase increment. The only difference between the three waveforms is that two were phase shifted with respect to the reference. These were the two voltages that were applied to the control shakers.

Accelerometers 1 to 3 were mounted on the load masses driven by the shakers. These were used in the calculation of the phase of the applied voltage. Measuring the phase directly in this way, rather than using the phase shift generated in the signals meant that any phase shift introduced by the power amplifiers would be taken into account. Accelerometers 4 and 5 were mounted at each end of the beam and the signals from these transducers were used to calculate the cost function.

The waveforms were ramped up for one second, then the amplitude was kept constant for three seconds whilst the amplitude and phase of each signal was measured, then the voltage was ramped down for a second. The ramping of the applied voltage at the beginning and the end was in order to avoid exciting harmonics in the beam, due to starting and ending the applied phase shifted signals at non-zero values. For example, starting a waveform at a peak like a cosine wave, rather than at a zero like a sine wave.

Figure 4.5 shows that the whole signal for each accelerometer was monitored in the five vertical graphs in the middle of the front panel. The uniform amplitude part of the signal, that was used to calculate the amplitude and phase, was displayed in the five vertical graphs on the right hand side of the front panel. To allow sufficient settling time, two seconds of the five second signal were used in the analysis.

The left hand side of Figure 4.6 shows a display of the 'raw' cost function obtained during the measurement. This plot simply shows the cost function varying with time as the control phase angles are changed. Once the cost function had been measured at all the required phase angles, a cost function surface was generated and the minimum found using MATLAB®. The cost function surface as a function of the control phase angles is shown in matrix form on the right hand side of Figure 4.6, and these data were stored to file to allow for any subsequent processing or analysis.

Using the full search method, it was only practical to measure a single frequency at a time. With three shakers mounted on the beam, a search using 10° steps required 1296 measurements of the cost function. Allowing ten seconds for each measurement cycle meant that it took over 3 hours to perform a full search at one frequency.

4.3.3 Propeller Signature Theory based minimisation

As an alternative to the full search methodology, the determination of the transfer function between each shaker and each control sensor was implemented using Propeller Signature Theory [60]. This also used the experimental set up shown in Figure 4.4.

LabView® programs were written to change the phase of each control machine individually as described in Chapter 3. Once the system had settled to a steady state condition, measurements were obtained of the acceleration at each control sensor. These measurements were used to determine the phase independent transfer function between each vibrating source and each control sensor as described in Chapter 3. These transfer functions were used in simulations within MATLAB® to obtain the cost function surface and hence the minimum of the cost function surface and the optimum control angles to obtain the minimum.

This search method requires fewer actual measurements than the full search methodology. Figure 4.7 shows part of the LabView® front panel used to determine the transfer functions. Three measurements were required at each frequency to determine the transfer function. For the experiment with the front panel shown in Figure 4.7, the

first measurement was with all machines in phase. The second was with a phase shift of 90° applied only to shaker 2, and the third measurement was with a phase shift of 90° applied only to shaker 3. A set of measurements of the transfer function from 20 Hz to 800 Hz in 10 Hz steps using three separate phase angles took approximately 50 minutes. Finding the minimum of the cost function at each frequency using simulations in MATLAB® took approximately 5 minutes for all 78 frequencies.

4.4 Results

This section presents results from the experiments performed to validate the conclusions drawn from the numerical simulations, and to test the feasibility of a practical synchrophasing system for vibration control of a simple machinery raft like structure. This section also contains a discussion of the results obtained.

4.4.1 Two electromagnetic vibrating sources on an elastic beam

Both cost functions were investigated by using the measured transfer mobilities in control simulations with two vibrating sources mounted upon the structure. Figure 4.8 and Figure 4.9 show the two cost functions for the system consisting of a compliantly mounted elastic beam with two shakers mounted upon it.

The positions of the shakers were at $x_1/l = 0.33$ and $x_2/l = 0.42$, so the shakers were on adjacent 'mass elements' of the structure, since the beam was divided into 12 elements as described in Section 4.2 and shown in Figure 4.2. The magnitude of the voltage applied to each shaker was the same, so the force that each shaker applied to the beam was nominally the same. The cost functions were calculated by manipulating the experimental transfer mobilities in computer based simulations, rather than searching directly for a minimum and maximum experimentally.

Figure 4.8 shows the variation in the time averaged kinetic energy cost function $\langle T \rangle_t$ with frequency, and Figure 4.9 the variation in the cost function which sums the

magnitude of the velocity squared at each end mounting point *J*. Both figures show the maximum of the cost function as the dotted curve and the minimum of the cost function as the solid curve.

By examining the displacement measured at each of the 36 positions along the beam, at a single frequency, it was possible to recognise the two rigid-body modes of the beam at 14 Hz and 30 Hz and peaks in the forced response due to flexural modes at 110 Hz, 266 Hz, 658 Hz and 990 Hz. These are marked on the figures, with the lowest rigid body mode being the translational mode. Other peaks in the forced response are observable at high frequencies; these are due to vibration of the structure in higher order flexural modes.

The figures show that the translational rigid body mode at 14 Hz has been well controlled in both cost functions, a reduction of 20 dB in each cost function being achieved by synchrophasing. The second rigid-body mode at approximately 32 Hz was not controlled as well, with synchrophasing achieving a reduction of approximately 5 dB. Inspection of the operational deflection shape (ODS) at 32 Hz showed that the shaker at $x_2/l = 0.42$ was near to a vibration minimum in the ODS. This is similar to the node of the second rigid-body mode, when the shaker is in anti-phase with the reference shaker. Hence the shaker was not effective at controlling the vibration. A reduction of approximately 10 dB was then achieved up to 170 Hz including the first flexural mode when using the time averaged kinetic energy cost function. This improvement then reduces with frequency, until at 250 Hz there is practically no improvement.

The cost function minimising the magnitude of the velocity squared at each end of the beam gave an improvement of approximately 10 dB at the first flexural mode. This improvement then dropped rapidly, achieving approximately 2 dB improvement until 250 Hz. A modest improvement of 1-2 dB was achieved for the second flexural resonance at 266 Hz. This improvement was small due to one of the shakers being situated near a vibration minimum of the ODS, hence the applied force was ineffective at reducing the cost function. The reduction then varied between 2 dB and 20 dB until

383 Hz, where there was no improvement by synchrophasing in either cost function. The reason for this lack of improvement is the cost functions that were chosen. Although the energy in each element changes with the phase of shaker 2, the energy in some elements increases and in others decreases hence little overall improvement is obtained for the time averaged kinetic energy across the structure.

Little improvement can be seen in the cost function which minimises the magnitude squared of the velocity at each end of the beam because the energy in the first and last elements varies very little with the phase of shaker 2. The reduction achieved by synchrophasing then increased, until approximately 8 dB reduction was achieved at the mode at 590 Hz, with the kinetic energy cost function performing slightly better. The third flexural mode at 658 Hz was not well controlled, synchrophasing achieving 2 to 4 dB reduction of the peak value. Above 700 Hz the reduction achieved by synchrophasing increased until a 25 dB reduction was obtained for the flexural mode at 990 Hz.

Figures 4.10 and 4.11 show simulations of the variation in the two cost functions, as the phase of the controlling machine is changed. These simulations were generated using the analytical model described in Chapters 2 and 3. These simulations show that the predicted reduction achieved by synchrophasing is very similar for both cost functions. Figures 4.10 and 4.11 both show that the first rigid-body mode was very well controlled, but the second rigid-body mode was not well controlled. Both simulated cost functions predicted a reduction of 8 dB at the first flexural mode, which compared well with the experimental results, where a reduction of 10 dB was achieved.

Figures 4.12 and 4.13 show the measured control source phase angles required to maximise and minimise the cost functions at each frequency. The shaker positions and magnitudes of the applied voltages are the same as for Figures 4.8 and 4.9. The phase angle ϕ was measured with respect to the phase of the reference source. Figure 4.12 and Figure 4.13 show that, away from the natural frequencies of the beam, the optimum

phase is very close to being either in-phase or in anti-phase with respect to the reference source.

From 10 Hz until 170 Hz, which includes the two rigid-body modes and the first flexural mode, the optimum phase for minimising both cost functions varies from $170^\circ - 185^\circ$ with respect to the reference phase. Except at 27 Hz, which is near to the second rigid-body mode at 32 Hz, where it drops to 130° for the time averaged kinetic energy cost function and 95° for the sum of the magnitude of the velocity squared cost function.

The optimum synchrophase angle to minimise the kinetic energy remains in the region $170^\circ - 185^\circ$ up to 250 Hz, whilst the optimum phase angle to minimise the square of the magnitude of the velocity at the mounting positions increases from 180° to 360° between 170 Hz and 190 Hz.

In the frequency range close to the second flexural mode at 266 Hz, the optimum phase for control is close to 0°, although the improvement obtained by synchrophasing is small as the energy in each element is insensitive to changes in the control phase angle.

Above the second flexural mode between 290 Hz and 315 Hz, the optimum phase angle varies over a range of values between $10^\circ - 150^\circ$ with both cost functions showing similar changes in optimum angle. Figures 4.8 and 4.9 show that there are some modes in this region but they are not flexural modes along the length of the beam.

Between 320 Hz and 380 Hz the optimum phase for control is once again close to 0° for both cost functions, then from 400 Hz to 1 kHz, the optimum phase is close to 180°, ranging from $160^\circ - 190^\circ$. The only exception being the flexural mode at 658 Hz, which as previously indicated, is not well controlled.

Figures 4.14 and 4.15 show simulations of the phase to maximise and minimise each cost function. The figures confirm the prediction of Chapter 3 and agree with the

experimental findings that the optimum phase angle for the control source is usually either in phase or in anti-phase with respect to the reference source.

Figures 4.16 and 4.17 show experimental results and simulations of the cost function reduction as a function of frequency for both cost functions. Figure 4.16 shows that both the local and the global cost functions have been successful in reducing the value of the cost function to below its maximum value for most frequencies. For this particular configuration of the shakers on the beam, the reduction in the time averaged kinetic energy cost function was the most successful. The greatest reduction occurs at frequencies between 10 Hz and 300 Hz, corresponding to the frequency band containing the rigid body modes and the first two flexural modes. The simulations shown in Figure 4.17 show a similar reduction to that obtained experimentally, except for near the first rigid-body mode, where the simulated reduction is larger than that obtained experimentally. The cost function reductions obtained experimentally and by simulation, at frequencies corresponding to the two rigid body modes and the first two flexural modes, for each of the two cost functions $\langle T \rangle_t$ (in dB re 1 J) and J (in dB re $1\mathrm{m}^2\mathrm{s}^{-2}$), are summarised in Table 4.2.

Mode	Experimental Results Cost function reduction / dB		Simulation Cost function reduction / dB	
	$\langle T \rangle_t$	J	$\langle T \rangle_t$	J
RBM1	20	20	47	42
RBM2	5	4	3	3
FM1	10	10	8	8
FM2	1	1	4	4

Table 4.2. Summary of the cost function reduction obtained experimentally and using simulations. For the source configuration $x_1/l = 0.33$ and $x_2/l = 0.42$.

To investigate the effect of source location, the two electrodynamic shakers were moved. Figure 4.18 shows the variation in the time averaged kinetic energy cost

function with frequency, and Figure 4.19 the variation in the cost function which sums the magnitude of the velocity squared at each end mounting point, for shakers at $x_1/l = 0.25$ and $x_2/l = 0.58$ i.e. the shakers were on either side of the centre of the beam. The magnitude of the voltage applied to each shaker was the same.

By examining the displacement measured at each of the 36 positions along the beam, at a single frequency, it was possible to recognise the two rigid-body modes of the beam at 14 Hz and 30 Hz and peaks in the forced response due to flexural modes at 110 Hz, 237 Hz, 743 Hz and 976 Hz. These are marked on the figures, with the lowest rigid body mode being the translational mode. Examination of the peak in the forced response at 472 Hz showed that the beam was twisting as well as flexing at this frequency of excitation.

For shakers in these positions upon the structure, both control methods exhibit a similar reduction in levels at and around the rigid body modes, i.e. up to 35 Hz. Approximately 19 dB reduction being achieved around the translational rigid body mode. However, little reduction was obtained between 40 Hz and 120 Hz, which includes the first flexural mode. The first flexural mode at 110 Hz was not well controlled because the shaker at $x_1/l = 0.25$ is near a vibration minimum of the ODS.

Between 120 Hz and 230 Hz, the minimisation of the cost function which sums the magnitude of the velocity squared over each end mount point performed much better giving a reduction of approximately 8-11 dB, compared to the time averaged kinetic energy cost function, which achieved very little reduction until 200 Hz. For this source configuration, the second flexural mode is much better controlled giving a 10 dB improvement at and around the resonance frequency. Between 250 Hz and 400 Hz the cost function which sums the magnitude of the velocity squared over each end mount point performs much better, giving a reduction of approximately 10 dB, compared to the time averaged kinetic energy cost function, which achieves only 1 dB reduction. The mode at 472 Hz and the third flexural mode at 743 Hz are also controlled by synchrophasing, giving a 10 dB reduction for both using the time averaged kinetic

energy cost function, and 25 dB and 10 dB respectively for the velocity cost function. The fourth flexural mode at 976 Hz is reduced by 4 dB by both cost functions.

Figures 4.20 and 4.21 show simulations of synchrophasing using the two cost functions, with simulated shakers at $x_1/l = 0.25$ and $x_2/l = 0.58$. These figures confirm the experimental result that for this configuration of shakers on the beam, a greater reduction in the cost function is obtained at and around the second flexural mode (FM2) by using the cost function which sums the magnitude of the velocity squared over each end mount point.

Figure 4.22 and Figure 4.23 show the variation in the phase of the signal applied to the experimental control source in order to either minimise or maximise the cost functions, when synchrophasing using the same shaker positions as in Figures 4.18 and 4.19. It can be seen again that the optimum synchrophase angles for extrema of the cost function away from the frequencies where the modes occur are close to 0° or 180° i.e. either in phase or in anti-phase with respect to the reference phase signal. Both of the cost functions exhibit a small increase in the response at 154 Hz and 319 Hz. These are not flexural modes along the length of the beam, however it can be seen that the control phase changes rapidly around these frequencies. Figure 4.22 shows that the optimum phase for controlling the time averaged kinetic energy is more variable than the phase shown in Figure 4.23, the cost function which sums the magnitude of the velocity squared over each end mount point at and around these two frequencies. Figure 4.24 shows the measured displacement of the beam, when the phase angle of the voltage supplied to the control shaker is adjusted with respect to the reference shaker. The figure uses experimental data measured at 162 Hz, which is between the first and second flexural modes of the beam. Figure 4.24a shows the case when the control shaker is anti-phase to the reference shaker. As can be seen, element 1 - which is at $x/l = 0.042$ - is vibrating the most and contains a large proportion of the system energy. Figure 4.24b shows that, even when the phase angle is optimised to minimise the time averaged kinetic energy across the whole structure, element 1 still contains a large proportion of the energy. This is why minimisation using the time averaged kinetic energy cost function has not been successful at this frequency, as was shown in Figure

4.18. Figure 4.24c shows the displacement when the cost function which minimises the sum of the magnitude of the velocity squared at each end of the beam is used. This shows that the cost function has reduced the displacement at element 1 but increased it slightly at element 12. Figure 4.19 showed that this cost function was far more successful at this frequency than the global control cost function. However, this cost function does not include vibration of the other parts of the structure. As can be seen in Figure 4.24c, the displacement amplitude in the middle of the structure has increased significantly. This could cause any machinery mounted at these positions to experience much higher vibration levels and consequently more fatigue failure.

Figures 4.25 and 4.26 show simulations of the phase to maximise and minimise each cost function using simulated shaker positions the same as Figures 4.18 to 4.23. Figure 4.25 agrees with the experimental observation that the optimum phase for controlling the time averaged kinetic energy is more variable than the cost function which sums the magnitude of the velocity squared over each end mount point at and around 150 Hz.

Figure 4.27 and 4.28 show experimental data and simulation of the cost function reduction as a function of excitation frequency for this configuration of shakers. The figures show that both the local and the global cost functions have been successful in reducing the value of the cost function to below its maximum value, except at frequencies just below the first flexural mode where minimal reduction has been achieved. For this particular configuration of the shakers on the beam, both cost functions performed similarly over the frequency range including the two rigid-body modes and the first flexural mode. The cost function which minimises the sum of the magnitude squared of the velocity at each end of the beam was the most successful cost function from 120 Hz to 1 KHz, achieving a reduction of approximately 10 dB over the frequency range in the experimental data shown in Figure 4.27. The cost function reductions obtained experimentally and by simulation, at frequencies corresponding to the two rigid-body modes and the first two flexural modes, for each of the two cost functions $\langle T \rangle_t$ and J, using this source configuration are summarised in Table 4.3.

Mode	Experimental Results Cost function reduction / dB		Simulation Cost function reduction / dB	
	$\langle T \rangle_t$	J	$\langle T \rangle_t$	J
RBM1	20	19	38	30
RBM2	1	3	13	13
FM1	2	2	2	2
FM2	9	9	15	15

Table 4.3. Summary of the cost function reduction obtained experimentally and using simulations. For the source configuration $x_1/l = 0.25$ and $x_2/l = 0.58$.

4.4.2 Three electromagnetic vibrating sources on an elastic beam

The system shown in Figure 4.3 was used to investigate variations in the cost function which sums the magnitude of the velocity squared at each end mounting point, when three vibrating sources were mounted upon the beam. The phase of the voltage supplied to two of the shakers was adjusted with respect to the phase of the voltage supplied to a reference shaker. Two methodologies were investigated, the first consisted of a full search through the angles from 0° to 350° in 10° steps, so for two control shakers, this necessitated 1296 individual measurements of the cost function. The second methodology utilised Propeller Signature Theory to determine the phase independent transfer function and required only 3 to 6 individual measurements of the cost function. These phase independent transfer functions were then manipulated in the computer to determine the optimum control angles. The Propeller Signature Theory method is much faster as most of the searching for minima is done by simulation rather than by physically searching by adjusting the phase of the voltage supplied to each shaker. For the experimental results presented in this subsection, the phase reference source was at coordinate $x_1 = 0.45\,\text{m}$ $(x_1/l = 0.375)$, and the control shakers were at coordinates $x_2 = 0.25\,\text{m}$ $(x_2/l = 0.21)$ and $x_3 = 0.85\,\text{m}$ $(x_3/l = 0.71)$ respectively.

Both of these methodologies produce a cost function surface of the form shown in Figure 4.29. The figure shows the variation in the cost function *J* (the sum of the magnitude of the velocity squared at each end of the beam) as a function of the phase of the two control shakers ϕ_2 and ϕ_3. From a control point of view, the surface in Figure 4.29 is good for finding the minimum of the cost function, because it shows the presence of a single, well defined minimum when ϕ_2 and ϕ_3 are adjusted between 0° and 360°. However, a single well defined minimum is not always achievable, as was shown using simulations in Chapter 3 and will be shown experimentally later in this chapter.

The optimum phase to minimise the cost function over the range 0° to 360° for each control source can be determined from the cost function surface by using the MATLAB® MIN function to search the surface for the minimum. Both of these methodologies give similar results for the cost function minima and maxima. This is shown in Figure 4.30, which depicts the minima and maxima of the cost function as a function of frequency. The solid and dotted curves are the cost function minimum and maximum respectively, obtained using Propeller Signature Theory to determine the phase independent transfer functions, whilst the filled and clear dots show the results obtained using a full search over the range 0° to 350°. Because the time taken to determine the optimum control source angles using Propeller Signature Theory is so much less than the time required to perform a full search, Figure 4.30 contains data for Propeller Signature Theory every 10 Hz and data using a full search at a few individual frequencies. Figures 4.30 and 4.31 show experimentally and by simulation respectively, that the cost function can be reduced by 10-20 dB over a large part of the frequency range investigated with this configuration of forces on the beam. This frequency range includes the second rigid body mode of the system and the first three flexural modes.

Figure 4.32 shows experimentally, the phases required of the two control sources in order to minimise the cost function, obtained using both the full search and propeller signature theory. The solid dots and squares show the best phase angle at each

frequency for the machine at x_2 and the clear dots and squares, the best phase angle at each frequency for the machine at x_3. The figure shows that over the frequency band 20 Hz to 90 Hz, which includes the rotational rigid body mode, the phases required from the two control shakers are very similar. At the first flexural mode of 110 Hz, the phases of the control shakers are 7° for the shaker at $x_2/l = 0.21$ and $182°$ for the shaker at $x_3/l = 0.71$. Since the beam is resiliently mounted, the first flexural mode shape is very similar to that of a beam with free end conditions, which has nodes at $x/l = 0.22$ and $x/l = 0.78$. The analytical receptance based model derived in Chapter 2 predicts minima in the operational deflection shape at $x/l = 0.27$ and $x/l = 0.73$. So there is a node between the phase reference shaker at $x_1/l = 0.375$ and the control shaker at $x_2/l = 0.21$. In order to minimise the vibration at the ends, the control shaker at $x_2/l = 0.21$ is virtually in phase with the phase reference shaker. There is no node between the phase reference shaker and the control shaker at $x_3/l = 0.71$, hence to minimise the vibration, the optimum phase for this control shaker is virtually anti-phase with respect to the phase reference.

The optimum phase is very similar for both control shakers over the frequency range 100 Hz to 300 Hz, which includes the second flexural resonance at 220 Hz. Above 300 Hz, both control phases change rapidly, especially the phase of the source at x_3 near to the resonance at 350 Hz. Figure 4.32 shows that the optimum phase in this frequency range is neither in-phase with the reference shaker or in anti-phase, but a range of angles in between.

Figure 4.33 shows a simulation of the minimising control phase angles for the same configuration as was used experimentally in Figure 4.32. This simulation also shows a range of optimum phase angles around the rotational rigid-body mode at 26 Hz, the first flexural mode at 118 Hz, the second flexural mode at 258 Hz and between the second flexural mode and the third flexural mode at 518 Hz.

At 26 Hz, the control source phase angles to minimise the cost function are $\phi_2 = 91^\circ$ and $\phi_3 = 73^\circ$ respectively. Figure 4.34 shows a simulation of the operational deflection shape of the beam at 26 Hz (RBM 2). The dotted line is the ODS when just the reference vibrating source is exciting the beam, although the two control machines are present. The solid line is the ODS when all three sources are driving the beam using the phase angles of the control sources calculated to minimise the cost function. The magnitude of the drive voltage applied to each shaker was the same. As can be seen from Figure 4.34, vibration in the rotational rigid body mode will cause a large value for the cost function, because the cost function is proportional to the sum of the magnitudes of the displacement at each end of the beam, and for the rotational rigid body mode, the displacement is the largest at the ends of the beam. Synchrophasing reduces the vibration in the rotational rigid body mode shape, so that the residual vibration consists of motion in the translational rigid body mode shape, as shown by the solid line in Figure 4.34. The displacement at each end is at a much lower level in this case, and so the cost function is reduced.

Figure 4.35 shows a simulation of the operational deflection shape of the beam at 118 Hz. This is close to the first flexural mode shape of the beam and the dotted line in the figure shows that when the beam is driven by a single vibrating source, then the ODS is very similar to the first flexural mode of the beam. Synchrophasing at 118 Hz reduces the vibration in the first flexural mode, so that the ODS consists of the rotational rigid body mode and some residual flexing, as shown by the solid line of Figure 4.35.

Figure 4.36 shows a simulation of the ODS at 258 Hz, which is close to the second flexural mode shape of the beam. The dotted line in the figure shows the ODS when the beam is driven by a single vibrating source. The cost function is dominated by vibration at one end of the beam so that the sensor at $x = L$ is the most important. Synchrophasing at 258 Hz using $\phi_2 = 25^\circ$ and $\phi_3 = 6^\circ$ respectively reduces the vibration in the second flexural mode and produces the ODS shown as the solid line in Figure 4.36. This operational deflection shape shows that the translational rigid body mode and the first flexural mode are now the main components of the beam motion. Figures 4.34

to 4.36 show that even at operating frequencies very close to a mode of the structure, the cost function will still contain residual contributions due to other modes of the structure.

At any general operating frequency away from the modes, the optimum control source phase angles to reduce the cost function in one mode may well increase the vibration of another mode. This can be seen in Figure 4.37, which shows simulations of the ODS at 80 Hz, which is between the rotational rigid body mode and the first flexural mode. With all three sources vibrating in phase, the displacement is primarily due to the translational rigid body mode, with some bending due to the first flexural mode. This is shown as the dashed line.

In order to reduce the translational rigid body mode, the phases of the control sources can be set to $\phi_2 = 180^\circ$ and $\phi_3 = 180^\circ$ respectively. This reduces the component of displacement due to the translational rigid body mode, but increases the component due to the first flexural mode. This is shown by the solid line.

If $\phi_2 = 0^\circ$ and $\phi_3 = 180^\circ$ then the translational rigid body mode and the first flexural mode are reduced, but the rotational rigid body mode is excited. This is shown as the dotted line.

It is these opposing modal requirements in the control source phase angles which drives and limits the effectiveness of cost function minimisation using synchrophasing at each frequency. This effect where active control of one mode excites other modes of vibration is known as control spillover [22].

Figure 4.38 compares the cost function reduction obtained experimentally by synchrophasing with that obtained from simulations. The solid curve is the reduction achieved experimentally using the cost function which minimises the sum of the magnitude squared of the velocity at each end of the beam. The dotted curve is the reduction of the same cost function obtained by simulation. The positions of the shakers were $x_1/l = 0.375$ (phase reference), $x_2/l = 0.21$ and $x_3/l = 0.71$. The magnitude of the

drive voltage applied to each shaker was the same. These are the data shown in Figures 4.30 and 4.31 respectively. The figure shows very good agreement between the simulations and experimental data between 20 Hz and 120 Hz. This corresponds to a frequency range from just below the rotational rigid-body mode to just above the first flexural mode. The figure shows that synchrophasing can reduce the cost function by greater than 5 dB over this whole range and achieves a greater than 10 dB improvement over most of the range. Above the first flexural mode the experimental results and the simulations do differ because the modal frequencies predicted by simulation are higher than those measured experimentally. However the experimental data and the simulations do show a similar shape and a similar cost function reduction.

Figure 4.39 shows the cost function surface for 200 Hz, obtained by stepping through the control phase angles ϕ_2 and ϕ_3 from 0° to 350° in 10° steps. The shakers were in the same positions as the cost function surface shown in Figure 4.29. For this excitation frequency, the change in the cost function is larger with respect to control phase ϕ_3. Control phase ϕ_2 does not affect the cost function to a great extent and this leads to a shallower, less well defined minimum in the cost function. Because the minimum occurs near to the edges of the phase angle range, this shallow response is better shown by changing the phase range to -180° to 180° as is shown in Figure 4.40 for the same data as depicted in Figure 4.39.

Figure 4.41 shows the experimental cost function surface for 800 Hz generated by using a full search, and stepping the control phase angles generated by the LabView® code from a nominal 0° to 350° in 10° steps. The figure shows the presence of a global minimum at $\phi_2 = 150^\circ$ and $\phi_3 = 80^\circ$. There is another local minimum at $\phi_2 = 270^\circ$ and $\phi_3 = 320^\circ$ but the cost function is not as small at this local minimum as at the global minimum. The figure also shows that the cost function surface is not symmetric in this case. The implications here are that, if symmetry had been assumed and a smaller range of angles had been searched, then it is possible that a local minimum might have been found but not the global minimum.

4.4.3 Synchrophasing for unequal amplitude sources

Figure 4.42 shows a comparison of the cost function reduction obtained experimentally using synchrophasing when the magnitude of the drive voltage applied to each shaker was changed. The cost function reduction was obtained by calculating the difference between the maximum value of the cost function and the minimum value, when the phase of the drive voltage applied to the control sources is adjusted.

The effect of changing the magnitude of the drive voltage is to change the force applied by the shaker to the beam, thus simulating a change in a machine's vibration level. The shaker at position x_1, which was used for the phase reference, was also used for the drive voltage magnitude reference. A scaling factor λ_n is used to denote the magnitude of the n^{th} control source drive voltage with respect to the reference source. For the solid curve, the magnitude of the drive voltage applied to each shaker was the same, i.e. $\lambda_2 = 1$ and $\lambda_3 = 1$. For the dotted curve $\lambda_2 = 2/3$ and $\lambda_3 = 1/3$ and for the dashed curve $\lambda_2 = 1/3$ and $\lambda_3 = 2/3$.

The differences in the curves show that the amount that the cost function can be reduced, depends upon the magnitudes of the applied drive voltages and hence the applied forces on the beam. In practice this means that if the vibration levels of a machine change, either due to fatigue, a change in load conditions, operating speed or a gradual increase in unbalance during the machine's lifetime, then the cost function may also change.

Figure 4.42 shows that over the frequency range 50 Hz to 200 Hz, having the control sources at equal magnitude with the reference machine gave the best cost function reduction for this configuration of shakers on the beam, although the first flexural mode at 110 Hz is not well controlled, as shown by the low level of cost function reduction at 110 Hz. Above 200 Hz a better cost function reduction could be achieved by reducing the magnitude of the control sources. The dashed line in Figure 4.42 shows that at 250 Hz a better cost function reduction is achieved when $\lambda_2 = 1/3$ and $\lambda_3 = 2/3$ than when

$\lambda_2 = 1$ and $\lambda_3 = 1$. This is due to the choice of cost function, and the positioning of the machinery on the structure, with respect to the nodes of the main mode shapes that contribute to the operational deflection shape at any frequency. Figure 4.36 shows a simulation of the ODS at 258 Hz for $\lambda_2 = 1$ and $\lambda_3 = 1$. In this case a large amplitude of displacement is seen at one end of the beam, which was the major contribution to the cost function. When synchrophasing was used to minimise the cost function, the ODS was then primarily composed of translational rigid-body motion. Simulation at 250 Hz using $\lambda_2 = 1/3$ and $\lambda_3 = 2/3$ revealed that synchrophasing can minimise the cost function so that the ODS consists primarily of the first flexural mode, with some contribution from the translational rigid-body mode. In this case, the displacement at the ends – and hence the cost function – is reduced to a greater extent than the case when $\lambda_2 = 1$ and $\lambda_3 = 1$.

Figures 4.43 and 4.44 compare the optimum synchrophase angles ϕ_2 and ϕ_3 respectively, obtained experimentally for the control sources, when the magnitudes of the drive voltages are adjusted. Figure 4.43 shows ϕ_2, the phase required for the control machine at x_2 and Figure 4.44 shows ϕ_3, the phase required for the control machine at x_3 to achieve the global minimum of the cost function at each frequency. For the solid curve, the magnitude of the drive voltage applied to each shaker was the same, i.e. $\lambda_2 = 1$ and $\lambda_3 = 1$. For the dotted curve $\lambda_2 = 2/3$ and $\lambda_3 = 1/3$ and for the dashed curve $\lambda_2 = 1/3$ and $\lambda_3 = 2/3$. The figures show that, below 200 Hz, i.e. below the second flexural mode of the beam, the optimum phases are very similar regardless of the magnitude of the drive voltage. At these frequencies the main modal contributors to the ODS are the two rigid-body modes and the first flexural mode [67, 68].

At the second flexural mode, at 220 Hz, the cost function reduction achieved, as shown in Figure 4.42, is dependent upon the magnitude of the drive voltages applied to the control sources. There is approximately an 18 dB difference in the cost function reduction for the two cases where the magnitudes of the drive voltage applied to the

control sources were adjusted. Figure 4.43 shows that ϕ_2, the optimum phase for the control source at x_2, changes markedly in this region, whereas Figure 4.44 shows that ϕ_3 the optimum phase for the control source at x_3 does not vary as much. The optimum synchrophase angles for different magnitudes of the excitation voltages at 220 Hz are summarised in Table 4.4.

Magnitude of the control source voltage with respect to the reference		Voltage phase to minimise the cost function	
λ_2	λ_3	ϕ_2 / Degrees	ϕ_3 / Degrees
1	1	351	14
2/3	1/3	172	21
1/3	2/3	106	24

Table 4.4. Optimum synchrophase angles at 220 Hz (second flexural mode) obtained experimentally for three different configurations of the excitation voltage magnitude λ.

Figure 4.45 shows that at frequencies over the range 300 Hz to 400 Hz, which is close to the third flexural mode at 350 Hz, synchrophase angle ϕ_2 does not vary by a great deal as the excitation voltage magnitude is changed. ϕ_2 does vary by approximately 79 degrees at the third flexural mode at 350 Hz. Figure 4.46 shows that at frequencies at and around the third flexural mode, ϕ_3 is more variable than ϕ_2, changing by up to 180 degrees as the magnitude of the excitation voltage is changed.

Between 400 Hz and 650 Hz, the magnitude of the control excitation voltages does not have a significant effect on the optimum synchrophase angles, but above 650 Hz, it can be seen in Figure 4.43 that ϕ_2 again changes by more than 100 degrees. The optimum synchrophase angles for different magnitudes of the drive voltages at 750 Hz are summarised in Table 4.5.

Magnitude of the control source voltage with respect to the reference		Voltage phase to minimise the cost function	
λ_2	λ_3	ϕ_2 / Degrees	ϕ_3 / Degrees
1	1	86	19
2/3	1/3	202	53
1/3	2/3	101	44

Table 4.5. Optimum synchrophase angles at 750 Hz obtained experimentally for three different configurations of the drive voltage magnitude λ.

The experimental results presented in Figures 4.42 to 4.46 and Tables 4.4 and 4.5 show that the optimum control source phase angles for minimising the cost function using synchrophasing can be dependent on the amplitude of the sources, as these determine the magnitudes of the forces applied to the beam. In general, this will mean that, in a practical situation, if the vibration levels of the sources change, for reasons such as wear and tear, fatigue or a change in operating load, then the shape of the cost function will change and the optimum synchrophase angles of the control sources to minimise the cost function will also change.

The velocity at each sensor on the beam was given in Chapter 3 in Equation (3.49) and is repeated here for convenience

$$\dot{\mathbf{w}} = f_r \begin{bmatrix} y_{1,r} & y_{1,1} & \cdots & y_{1,P} \\ y_{2,r} & y_{2,1} & \cdots & y_{2,P} \\ \vdots & \vdots & \ddots & \vdots \\ y_{S,r} & y_{S,1} & \cdots & y_{S,P} \end{bmatrix} \begin{bmatrix} 1 & 0 & 0 & 0 \\ 0 & \lambda_1 & 0 & 0 \\ 0 & 0 & \ddots & \vdots \\ 0 & 0 & \cdots & \lambda_P \end{bmatrix} \begin{bmatrix} 1 \\ e^{j\phi_1} \\ \vdots \\ e^{j\phi_P} \end{bmatrix} \tag{4.4}$$

where $y_{s,p}$ are the point and transfer mobilities, λ_n is the magnitude of the n^{th} control force relative to the reference force f_r and ϕ_n is the phase of the n^{th} control source with respect to the reference source. The transfer function between each vibrating source and each control sensor is then defined as

$$\mathbf{\Gamma} = f_r \begin{bmatrix} y_{1,r} & y_{1,1} & \cdots & y_{1,P} \\ y_{2,r} & y_{2,1} & \cdots & y_{2,P} \\ \vdots & \vdots & \ddots & \vdots \\ y_{S,r} & y_{S,1} & \cdots & y_{S,P} \end{bmatrix} \begin{bmatrix} 1 & 0 & 0 & 0 \\ 0 & \lambda_1 & 0 & 0 \\ 0 & 0 & \ddots & \vdots \\ 0 & 0 & \cdots & \lambda_P \end{bmatrix} \tag{4.5}$$

If the relative magnitudes of the control sources change, this will affect the diagonal matrix of λ_n terms and hence the transfer function matrix $\mathbf{\Gamma}$.

If a full search methodology is employed, then this will necessitate running the full search again with the machines under their new load conditions. If the experimentally determined transfer functions are being used to simulate a full search, then in general, these transfer function terms will need to be re-determined for the new load conditions. However if the forces applied by each machine all increase or decrease by the same amount δ such that

$$\mathbf{\Gamma} = f_r \begin{bmatrix} y_{1,r} & y_{1,1} & \cdots & y_{1,P} \\ y_{2,r} & y_{2,1} & \cdots & y_{2,P} \\ \vdots & \vdots & \ddots & \vdots \\ y_{S,r} & y_{S,1} & \cdots & y_{S,P} \end{bmatrix} \begin{bmatrix} \delta & 0 & 0 & 0 \\ 0 & \delta\lambda_1 & 0 & 0 \\ 0 & 0 & \ddots & \vdots \\ 0 & 0 & \cdots & \delta\lambda_P \end{bmatrix} \tag{4.6}$$

then the cost function surface will have the same shape and hence the same control source phase angles will be required to minimise the cost function. Alternatively, if the change in each applied force could be measured locally so $\delta_r, \delta_1, \delta_2 \cdots \delta_P$ are all measurable, such that

$$\mathbf{\Gamma} = f_r \begin{bmatrix} y_{1,r} & y_{1,1} & \cdots & y_{1,P} \\ y_{2,r} & y_{2,1} & \cdots & y_{2,P} \\ \vdots & \vdots & \ddots & \vdots \\ y_{S,r} & y_{S,1} & \cdots & y_{S,P} \end{bmatrix} \begin{bmatrix} \delta_r & 0 & 0 & 0 \\ 0 & \delta_1\lambda_1 & 0 & 0 \\ 0 & 0 & \ddots & \vdots \\ 0 & 0 & \cdots & \delta_P\lambda_P \end{bmatrix} \tag{4.7}$$

then the change in transfer function can be corrected for and used in simulations to find the new cost function minimum without the need to recalculate the transfer function. Calculating the applied forces and mobilities on a large scale installation would, in practice be very difficult, and this is the reason that the transfer function approach was implemented as it does not require exact knowledge of the mobilities and the forces applied by each vibrating source.

Figure 4.47 shows the result of correcting the experimental transfer function data to simulate a different machinery load state. In this figure, the solid lines show the maximum and minimum of the cost function surface at each frequency when the magnitudes of the drive voltages applied were all the same, i.e. when $\lambda_2 = 1$ and $\lambda_3 = 1$. The dotted lines show the maximum and minimum of the cost function for the same vibrating source positions, but when $\lambda_2 = 1/3$ and $\lambda_3 = 2/3$ i.e. the magnitudes of the drive voltages have changed. The dashed lines show the maximum and minimum of the cost function by correcting for the change in drive voltage. These data were acquired experimentally using $\lambda_2 = 1/3$ and $\lambda_3 = 2/3$ but then corrections have been applied to simulate equal drive voltage magnitudes of $\lambda_2 = 1$ and $\lambda_3 = 1$, by using $\delta_2 = 3$ and $\delta_3 = 3/2$.

Figure 4.47 shows that it is possible to use one set of transfer function data to simulate the cost function surface, that will be obtained when different force magnitudes are applied to the beam, and hence predict the likely success of synchrophasing in reducing the cost function with different machinery states.

4.5 Conclusions

The purpose of the experimental investigation into synchrophasing described in this chapter was to compare the experimental results with the numerical simulations and to investigate the practical implementation of a synchrophasing system on a relatively simple structure.

Two control functions were initially investigated. Firstly, a cost function which minimised the total time averaged kinetic energy across the whole structure. This may be considered as a global cost function as it measures the cost function along the structure. Alternatively, a cost function which minimised the sum of the magnitude squared of the velocity measured at each end of the beam was evaluated for comparison and observation. This latter case may be considered as a local cost function as only the extremities of the structure were monitored. The results presented show that each method is able to provide some level of control and that the best cost function to use depends upon the positions of the vibrating sources upon the beam.

The advantage of the local cost function is that it is much easier to implement because it simply requires sensors over the structural mounting points and it does not require any information about the masses of the machinery mounted upon the structure or the structure itself. This information is required to determine the time averaged kinetic energy in each element of the structure when using the global cost function.

The disadvantage of the local cost function is that because only the structural mounting points are considered in the minimisation, the structure may be subjected to high amplitude vibrations at points away from those monitored and this was shown in the experimental data when two vibrating sources were mounted upon the structure. This may have implications for fatigue failure of the structure or may cause additional wear on machinery or rotating shafts.

Two methods of obtaining the cost function were investigated. The first was to simply change the phase of the voltage supplied to each control source so that phase angles from 0° to 360° using a suitable step size were applied, and the resultant cost function measured. This method has the advantage of simplicity as very little additional processing is required to determine the total cost function surface. However this method is very time consuming if the cost function surface is to be determined with any meaningful fidelity.

The second method investigated was to determine the transfer mobility between each machine and each sensor point by operating one machine at a time. As it may not be practical or possible to switch off all but one machine, the method was altered using an established aircraft engine synchrophasing method called Propeller Signature Theory.

Using this theory, a phase independent transfer function between each machine and each sensor point was determined, by introducing a known phase shift to the voltage supplied to each vibrating source in turn. The resulting measured velocities are then used to calculate either a fully determined or over determined solution for the phase independent transfer functions. These phase independent transfer functions can then be used in MATLAB® simulations to determine the whole cost function surface at any fidelity required.

This method is much quicker than physically stepping through all the possible phase angles and would be far more suitable as a form of close to real time adaptive vibration control. The transfer function values are not transfer mobilities as they do not calculate the forces applied by each vibration source. Hence if the load or speed of any machine were to change, it may be necessary to re-determine the transfer functions, because the optimum phase angles for minimising the cost function using synchrophasing could change if the applied forces change.

These experiments have shown that synchrophasing can be an effective vibration reduction technique and is relatively simple to install upon a structure. The main obstacle to overcome is likely to be how the phase of the voltage supplied to each machine can be varied and measured. The experimental results obtained using two and three electromagnetic shakers upon a thin box section beam show that very similar reductions in the cost functions were obtained both experimentally and using numerical simulations.

4.6 Figures

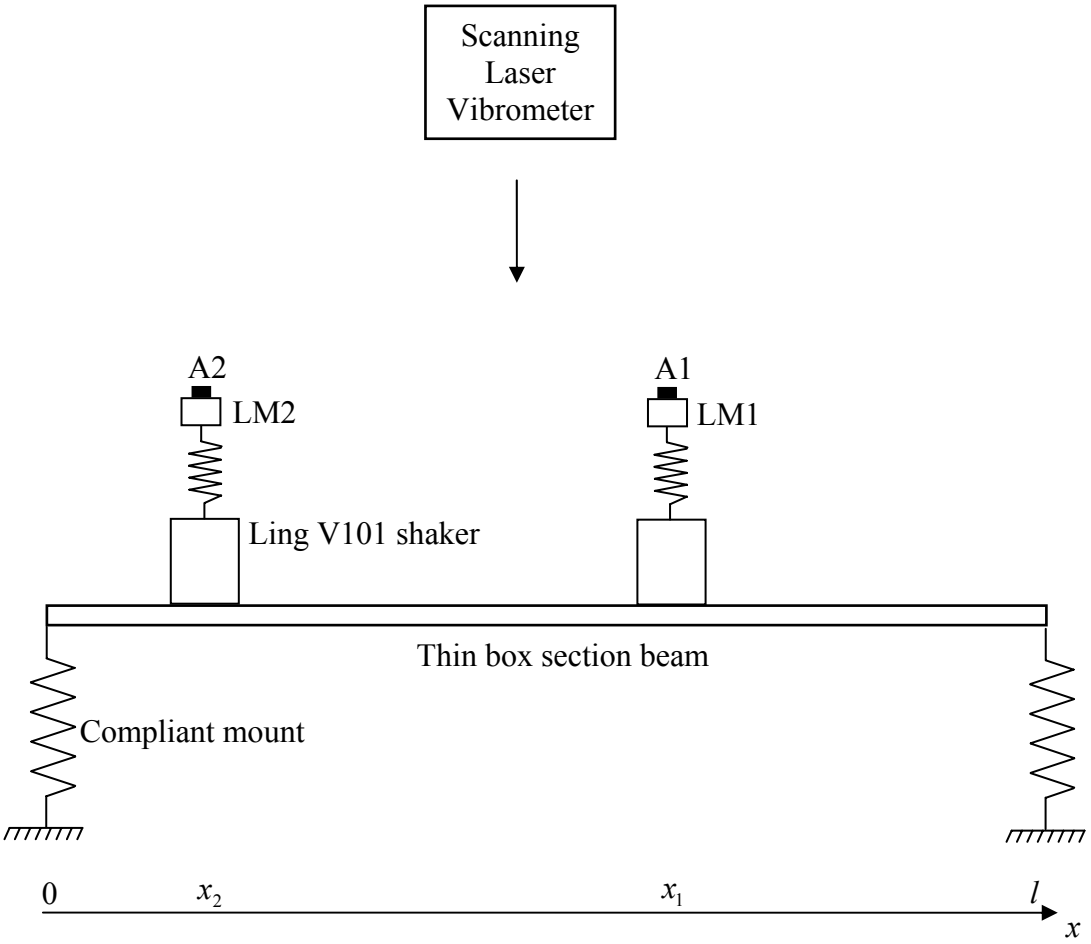

Key

A1-A2 Accelerometers A1 and A2

LM1-LM2 Load mass 1 and Load mass 2

Figure 4.1. Diagram showing the experimental system configuration used when two shakers were located on the thin box section beam. Accelerometer A1 was located on the load mass used as the phase reference. Its position on the beam is defined by coordinate x_1. Accelerometer A2 was located on the load mass of the shaker to which the phase of the applied signals are adjusted. The coordinate of this shaker is given by x_2. The velocity of the beam was measured using a scanning laser vibrometer.

a)

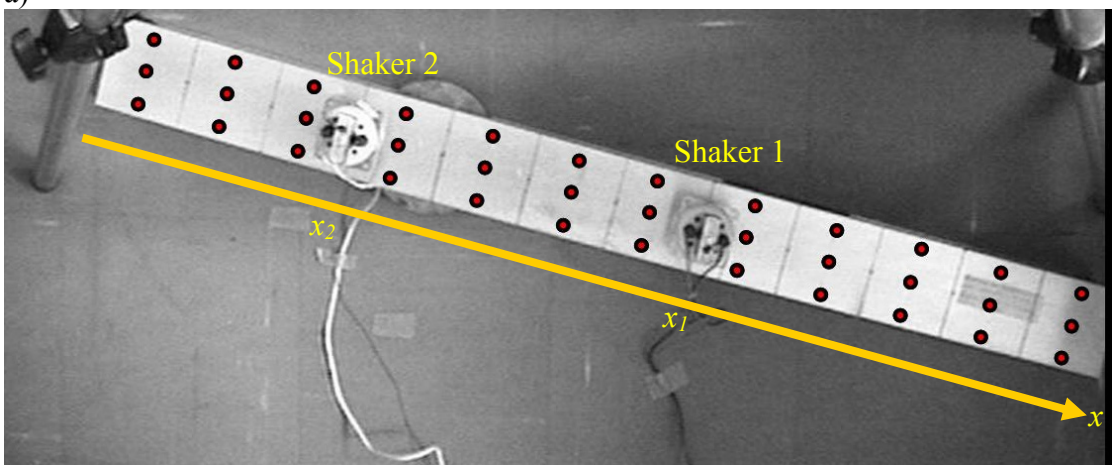

b)

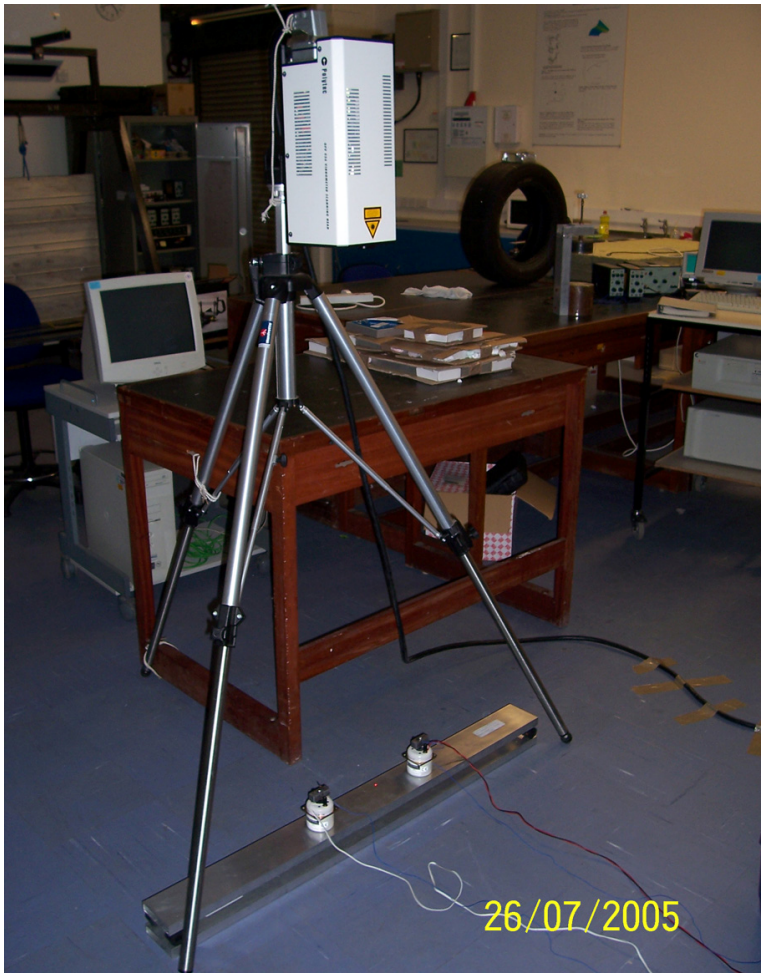

Figure 4.2. Showing a) the arrangement of points where the laser vibrometer was used to measure the velocity on the beam. The beam was divided into twelve sections and each section was measured at three positions across its width, b) the laser vibrometer scanning the beam one point at a time.

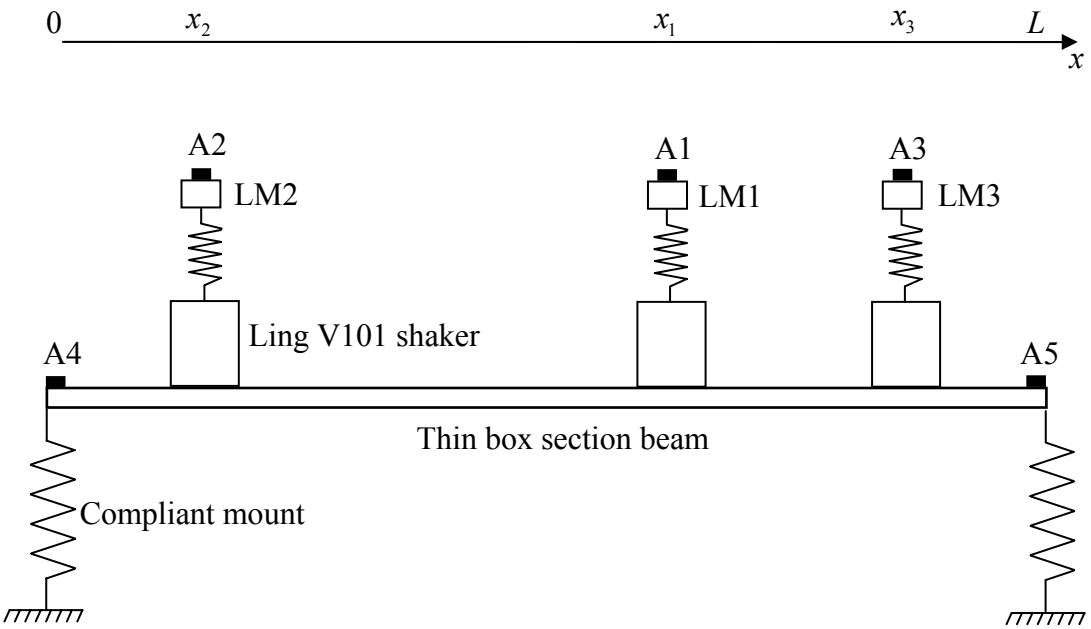

Key

A1-A5 Accelerometers A1 to A5

LM1-LM3 Load mass 1 to Load mass 3

Figure 4.3. Diagram showing the experimental system configuration used when three shakers were located on the thin box section beam. Accelerometer A1 was located on the load mass used as the phase reference. Its position on the beam is defined by coordinate x_1. Accelerometers A2 and A3 were located on the load masses of the shakers to which the phase of the applied signals are to be adjusted. The coordinates of these shakers are given by x_2 and x_3 respectively. A4 and A5 were located over the compliant mounts at each end of the beam.

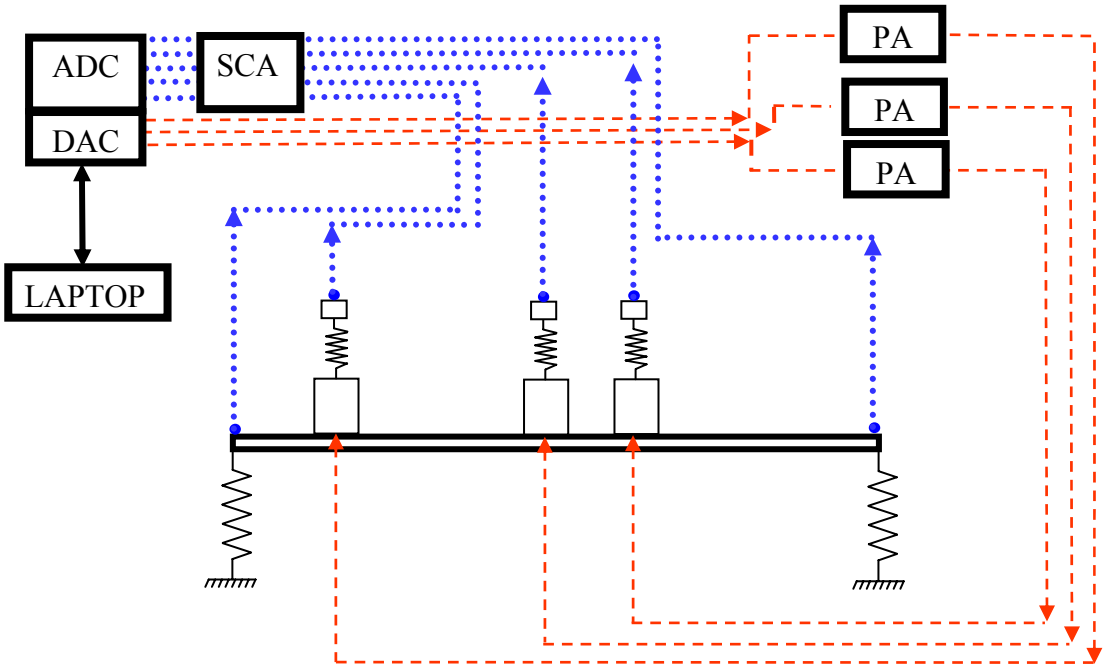

Figure 4.4. Block diagram of the experimental set up used to minimise the cost function of the sum of the magnitude squared of the velocity at each end of the beam. The measurements are stored and processed and the control signals generated by a laptop computer running LabView®. The acceleration responses at the 5 accelerometer positions, shown as dotted lines are fed to an analogue to digital converter (ADC), via signal conditioning amplifiers (SCA). The excitation waveforms are generated in LabView® and are converted to analogue signals in the digital to analogue converter (DAC). These are fed to power amplifiers (PA) which drive the shakers, shown as dashed lines.

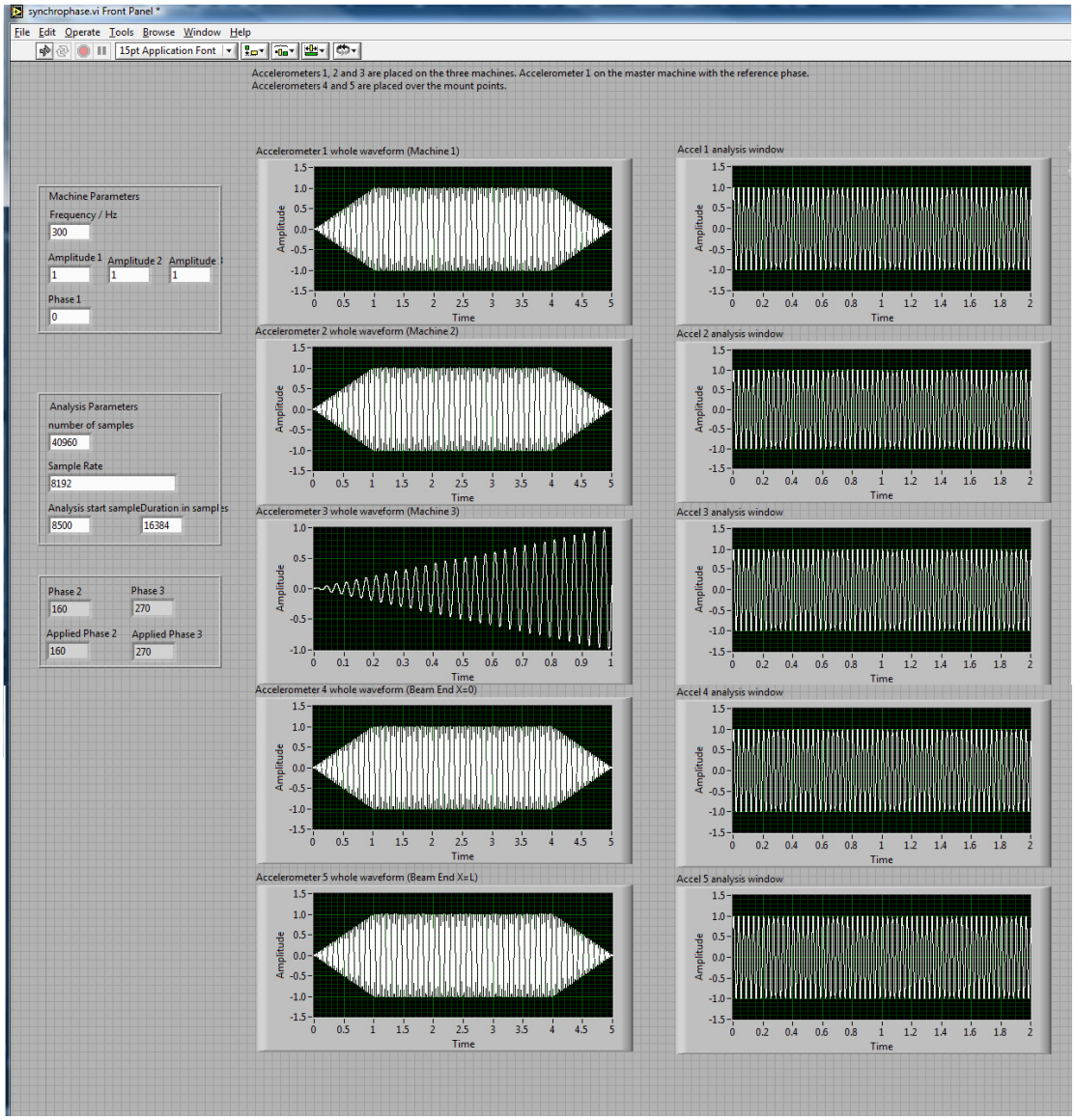

Figure 4.5. The LabView® front panel showing the experimental signals measured on the accelerometers during a full search at a single frequency. Accelerometers 1 to 3 were mounted on the load masses on the shakers, and accelerometers 4 and 5 were mounted at each end of the beam. A voltage was applied to each shaker at a specific phase angle for 5 seconds. For the first second, the signals were ramped up. The analysis was performed over the period 1.5s to 3.5s and this is shown in the Accelerometer analysis windows on the right hand side. After the analysis, the voltage was then ramped down. The time on the LabView® front panel was measured in seconds.

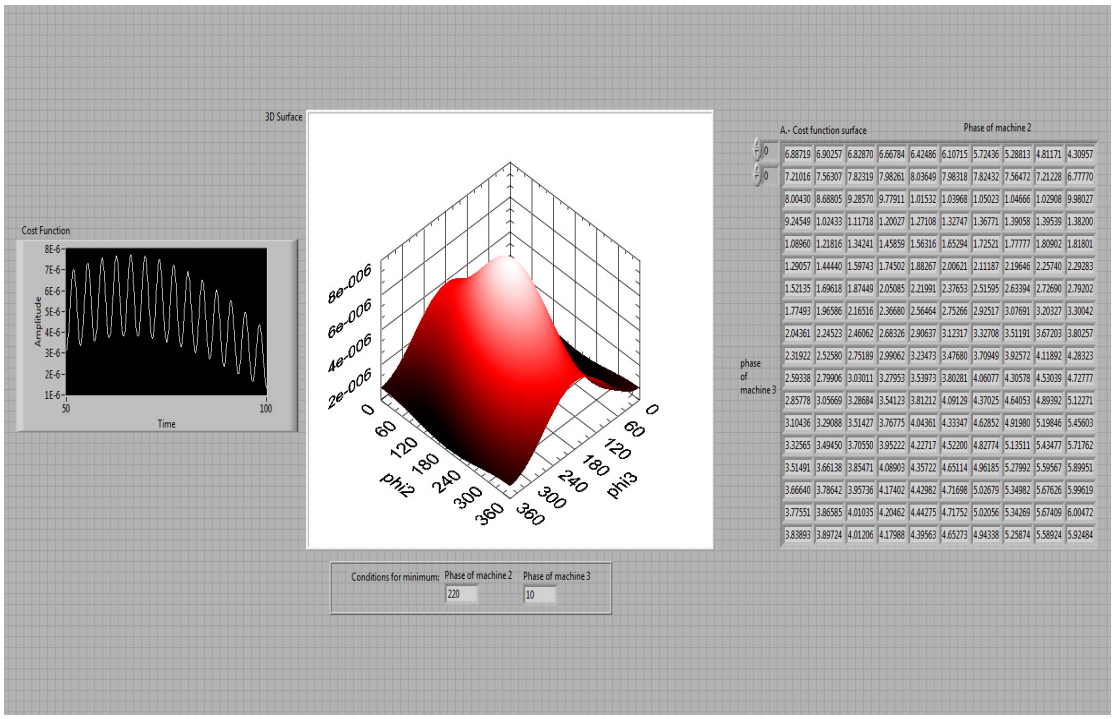

Figure 4.6. The LabView® front panel showing the calculation of the cost function and generation of the cost function surface from the signals measured on the accelerometers during a full search at a single frequency.

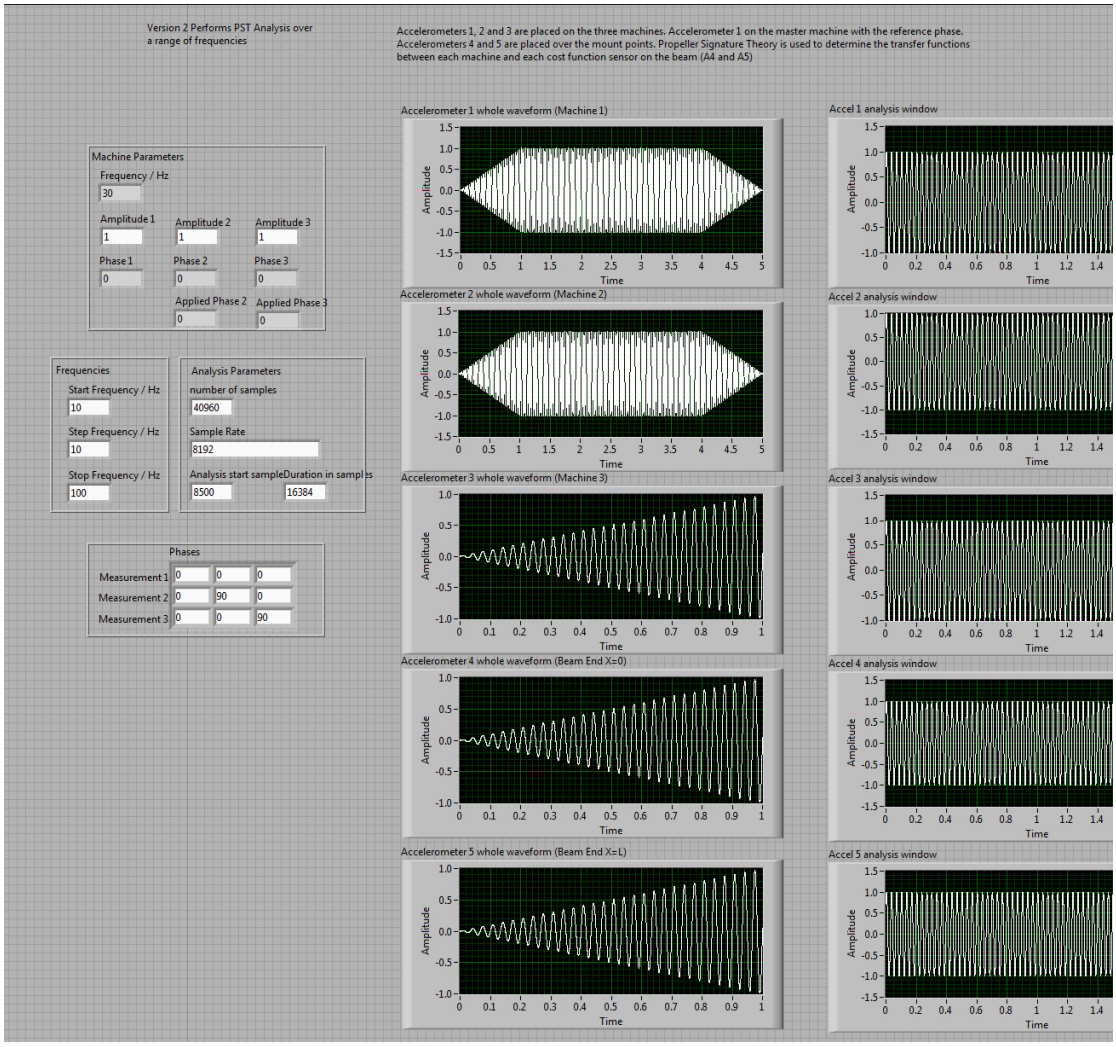

Figure 4.7. The LabView® front panel used to determine the experimental transfer function between each shaker and each control sensor. Accelerometers 1 to 3 were mounted on the load masses on the shakers, and accelerometers 4 and 5 were mounted at each end of the beam. A voltage was applied to each shaker at a specific phase angle for 5 seconds. For the first second the signals were ramped up. The analysis was performed over the period 1.5s to 3.5s and this is shown in the Accelerometer analysis windows on the right hand side. Once the analysis was completed, the voltage was then ramped down. Because only three measurements of phase were required to determine the transfer function, the program ran over a frequency range, rather than at a single frequency. The values of the transfer function at each frequency were stored in a text file and used in MATLAB® simulations to determine the cost function surface at each frequency.

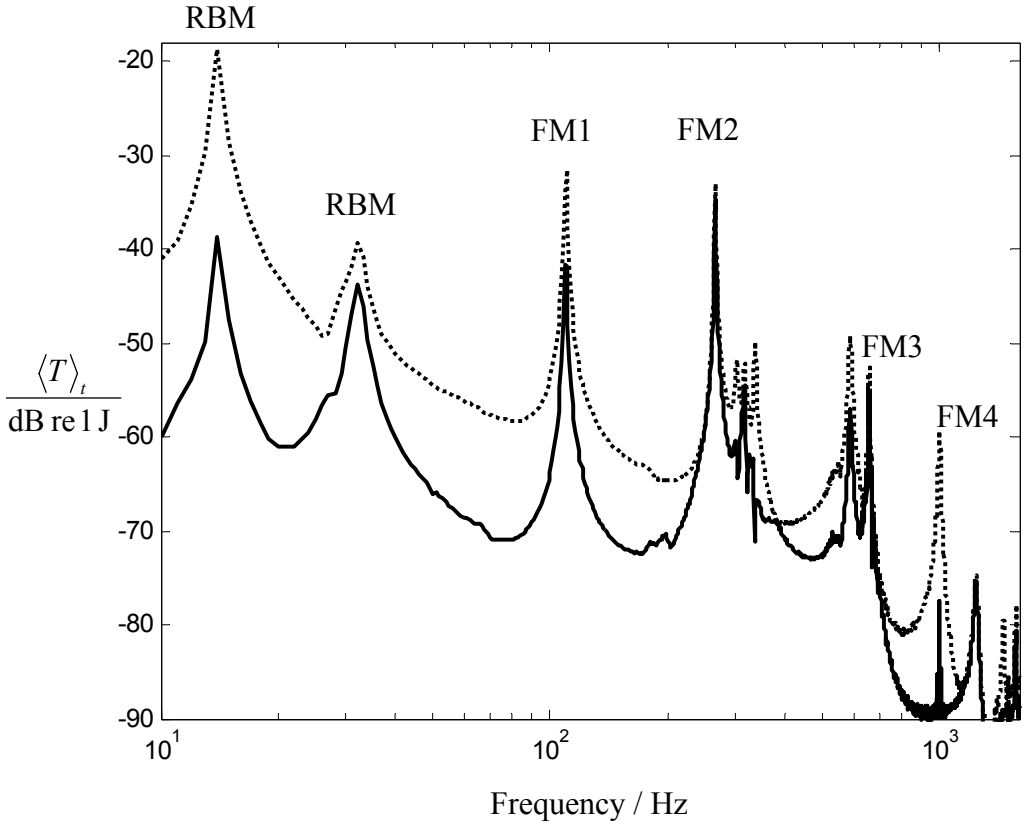

Figure 4.8. Experimental determination of the time averaged kinetic energy of the beam. The dotted curve shows the maximum and solid curve the minimum achieved by synchrophasing. The positions of the shakers were $x_1/l = 0.33$ and $x_2/l = 0.42$, the magnitude of the drive voltage applied to each shaker was the same. The figure shows the two rigid body modes (RBM) of the beam on the elastic end supports and the first 4 flexural modes (FM1 to FM4). Other peaks in the forced response are observable at higher frequencies, but these are not clearly attributable to a particular mode of a beam in flexure.

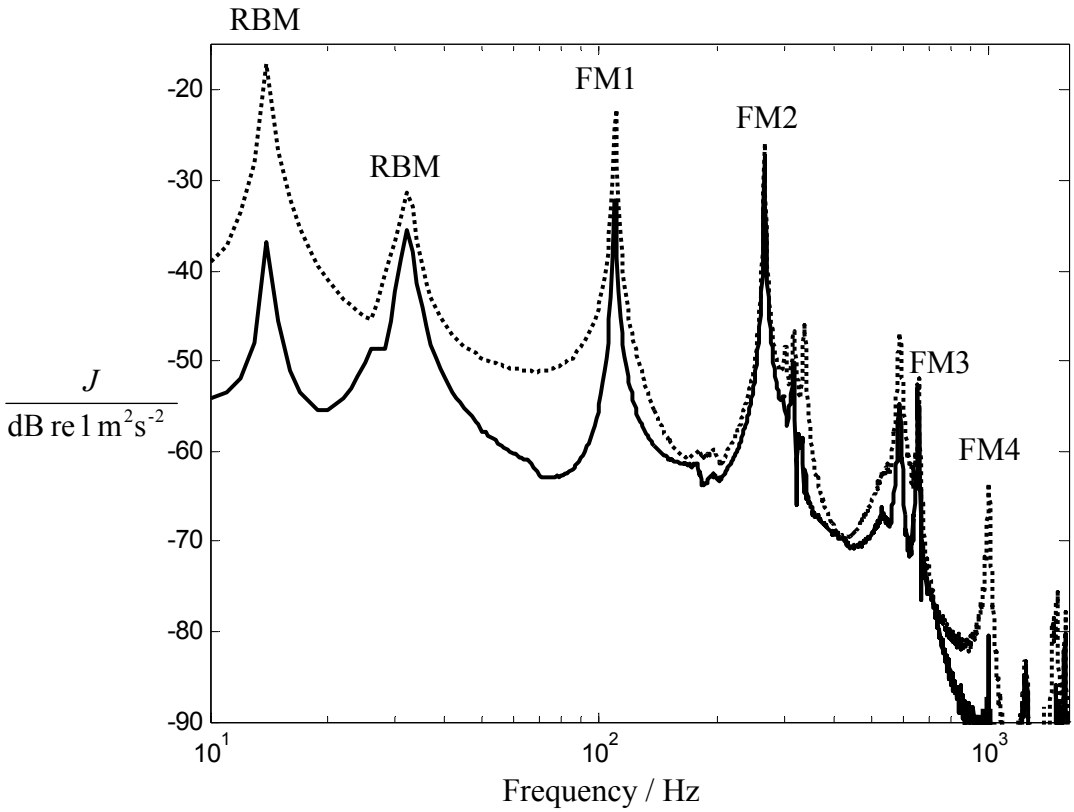

Figure 4.9. Experimental determination of the sum of the magnitude squared of the velocity at each end of the beam. The dotted curve shows the maximum and solid curve the minimum achieved by synchrophasing. The positions of the shakers were $x_1/l = 0.33$ and $x_2/l = 0.42$, the magnitude of the drive voltage applied to each shaker was the same. The figure shows the two rigid body modes (RBM) of the beam on the elastic end supports and the first 4 flexural modes (FM1 to FM4). Other peaks in the forced response are observable at higher frequencies, but these are not clearly attributable to a particular mode of a beam in flexure.

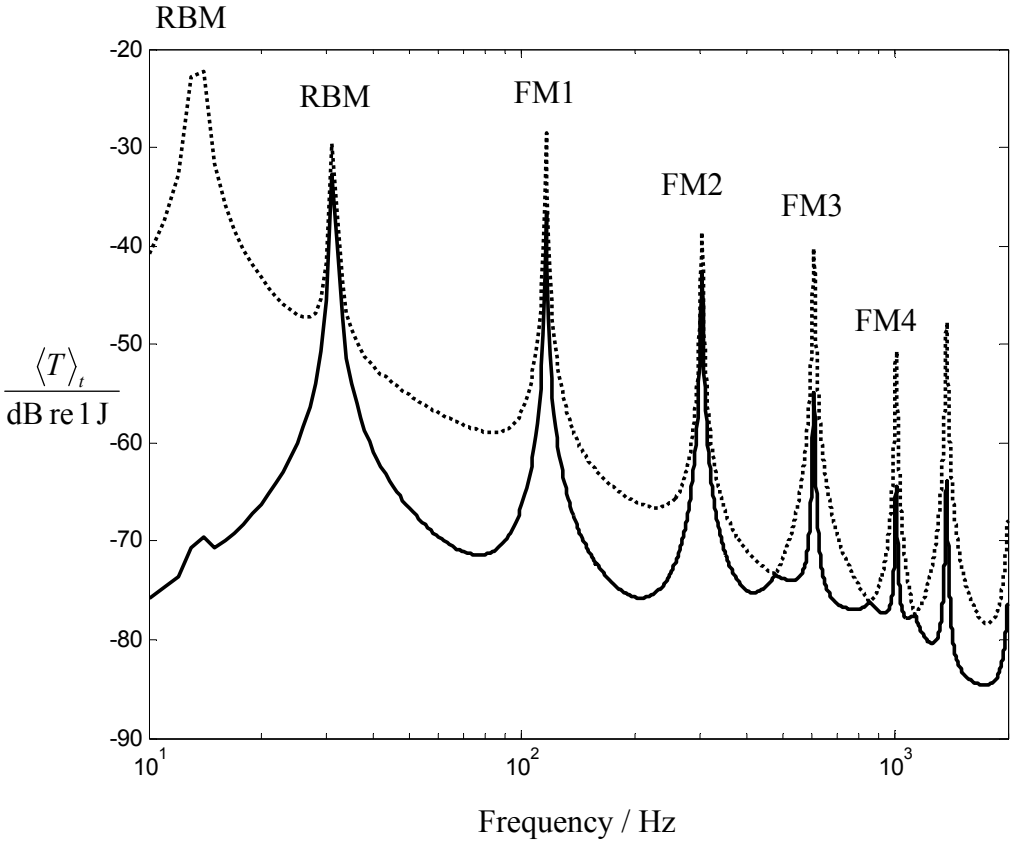

Figure 4.10. Simulations of the time averaged kinetic energy of the beam. The dotted curve shows the maximum and solid curve the minimum achieved by synchrophasing. The positions of the shakers were $x_1/l = 0.33$ and $x_2/l = 0.42$, the magnitude of the drive voltage applied to each shaker was the same. The figure shows the two rigid body modes (RBM) of the beam and the first 4 flexural modes (FM1 to FM4).

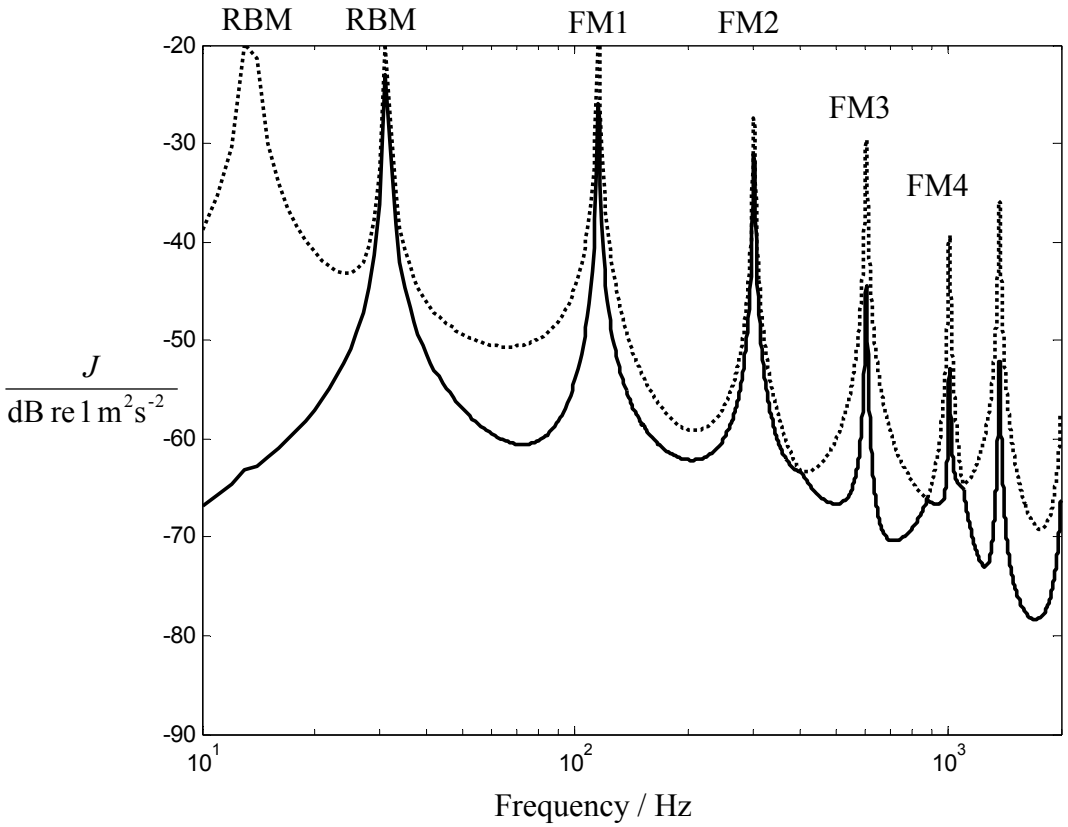

Figure 4.11. Simulations of the sum of the magnitude squared of the velocity at each end of the beam. The dotted curve shows the maximum and solid curve the minimum achieved by synchrophasing. The positions of the shakers were $x_1/l = 0.33$ and $x_2/l = 0.42$, the magnitude of the drive voltage applied to each shaker was the same. The figure shows the two rigid body modes (RBM) of the beam and the first 4 flexural modes (FM1 to FM4).

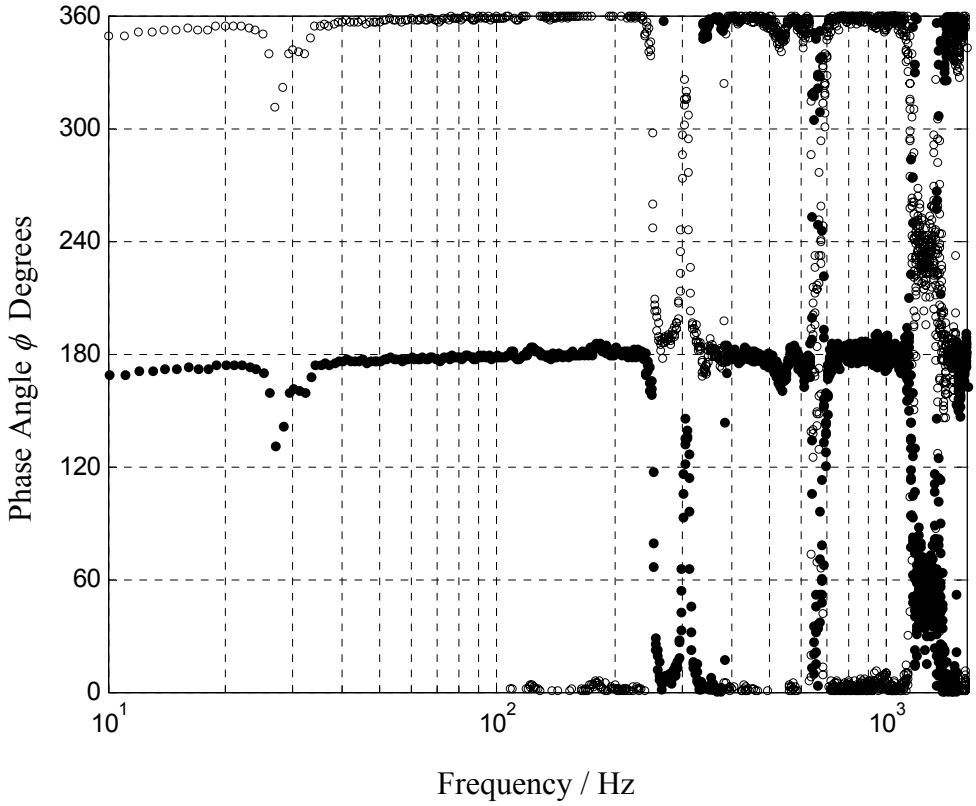

Figure 4.12. Experimental result showing the phase of the control source corresponding to the maximum and minimum of the time averaged kinetic energy. The clear dots show the phase to obtain the maximum kinetic energy and solid dots the phase to achieve the minimum by synchrophasing. The positions of the shakers were $x_1/l = 0.33$ and $x_2/l = 0.42$, the magnitude of the drive voltage applied to each shaker was the same.

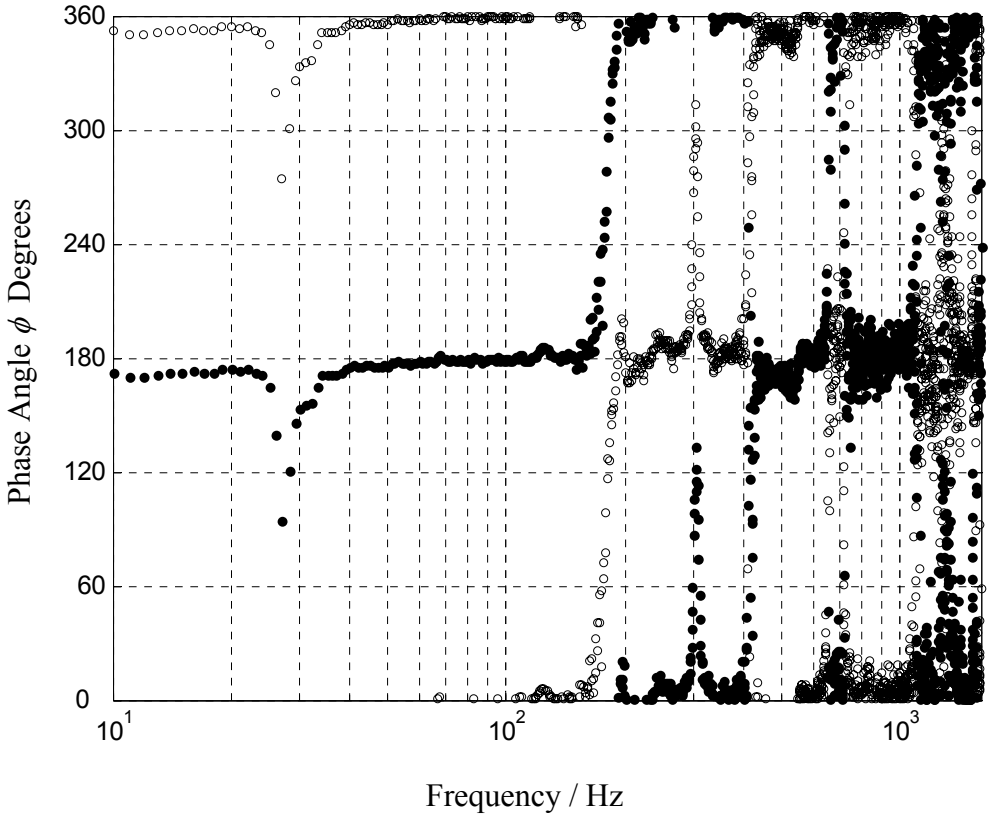

Figure 4.13. Experimental result showing the phase of the control source corresponding to the maximum and minimum of the cost function summing the magnitude squared of the velocity at each end of the beam. The clear dots show the phase to obtain the maximum value of the cost function and solid dots the phase to achieve the minimum by synchrophasing. The positions of the shakers were $x_1/l = 0.33$ and $x_2/l = 0.42$, the magnitude of the drive voltage applied to each shaker was the same.

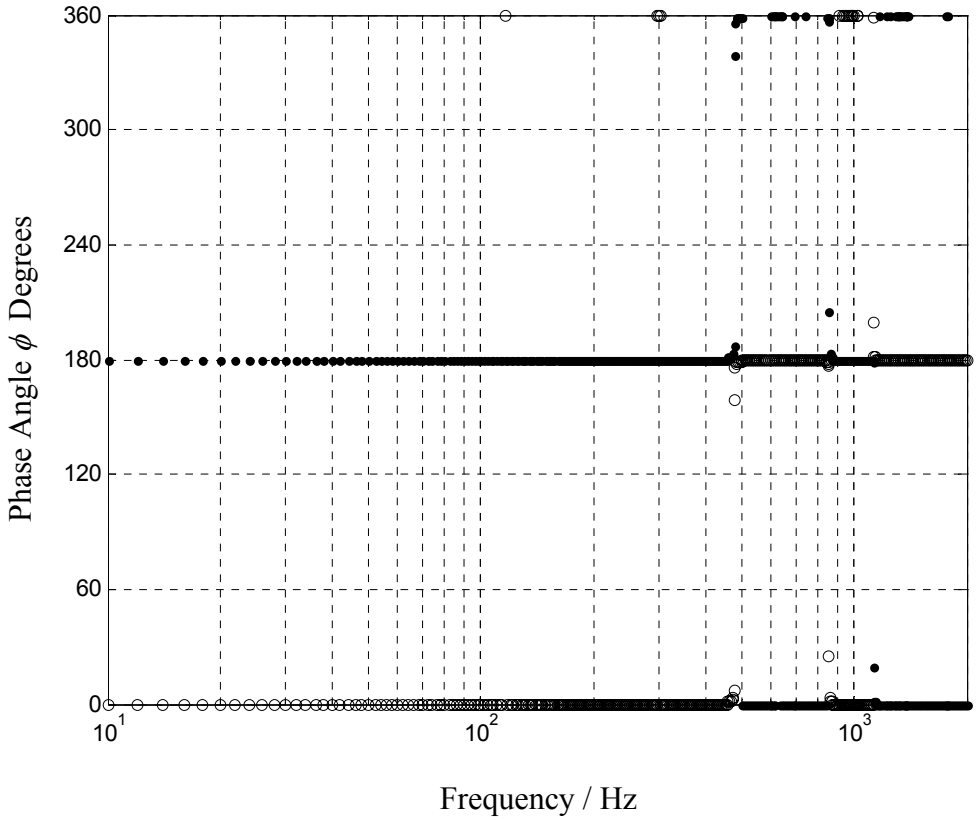

Figure 4.14. Simulations of the phase of the control source corresponding to the maximum and minimum of the time averaged kinetic energy. The clear dots show the phase to obtain the maximum kinetic energy and solid dots the phase to achieve the minimum by synchrophasing. The positions of the shakers were $x_1/l = 0.33$ and $x_2/l = 0.42$, the magnitude of the drive voltage applied to each shaker was the same.

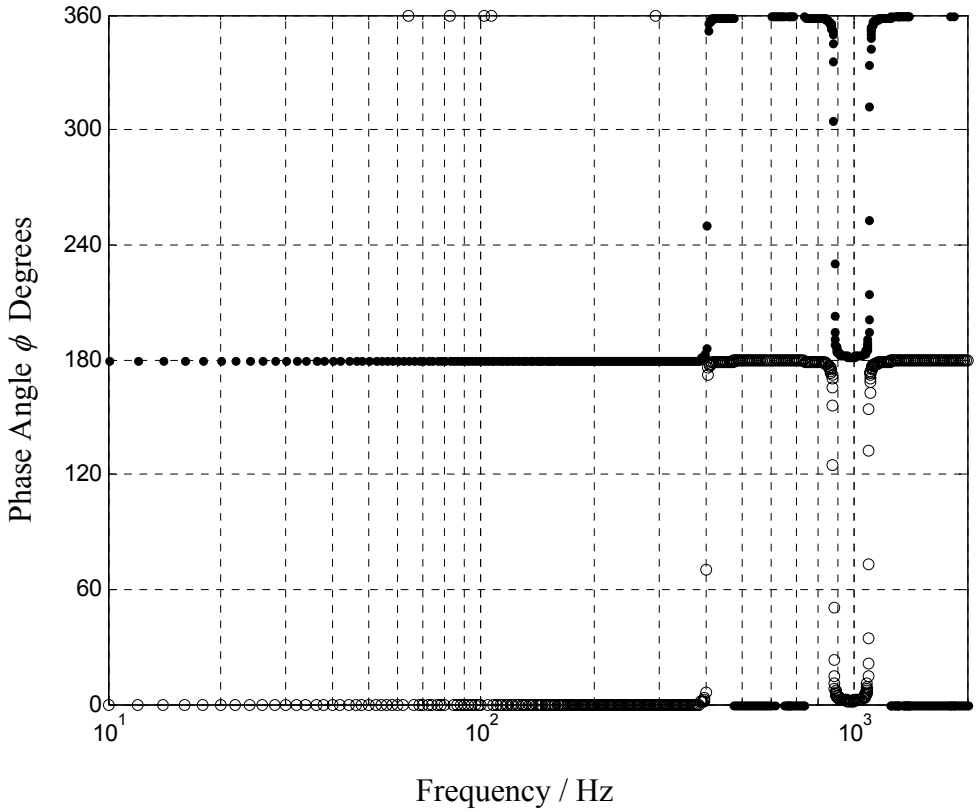

Figure 4.15. Simulations of the phase of the control source corresponding to the maximum and minimum of the cost function summing the magnitude squared of the velocity at each end of the beam. The clear dots show the phase to obtain the maximum value of the cost function and solid dots the phase to achieve the minimum by synchrophasing. The positions of the shakers were $x_1/l = 0.33$ and $x_2/l = 0.42$, the magnitude of the drive voltage applied to each shaker was the same.

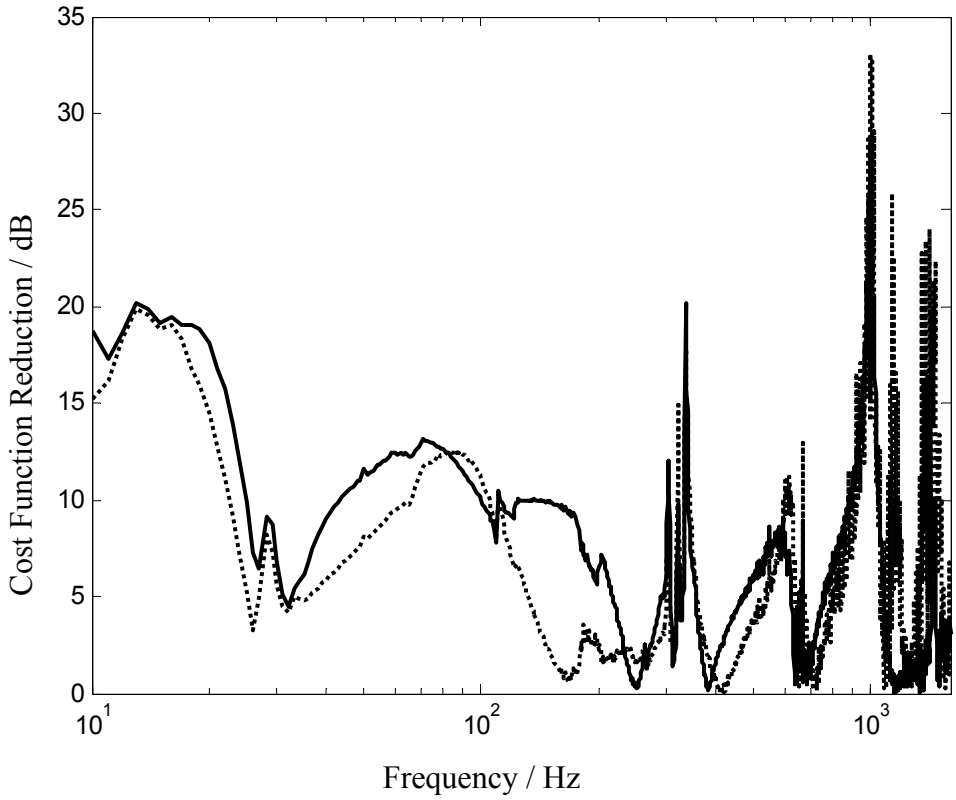

Figure 4.16. Experimental result showing the cost function reduction as a function of frequency of excitation. This was obtained by calculating the difference between the maximum value of the cost function and the minimum. The solid curve is the reduction achieved using the time averaged kinetic energy cost function (in dB re 1 J) and the dotted curve is the reduction achieved using the cost function which minimises the sum of the magnitude squared of the velocity at each end of the beam (in dB re $1\mathrm{m}^2\mathrm{s}^{-2}$). The positions of the shakers were $x_1/l = 0.33$ and $x_2/l = 0.42$, the magnitude of the drive voltage applied to each shaker was the same.

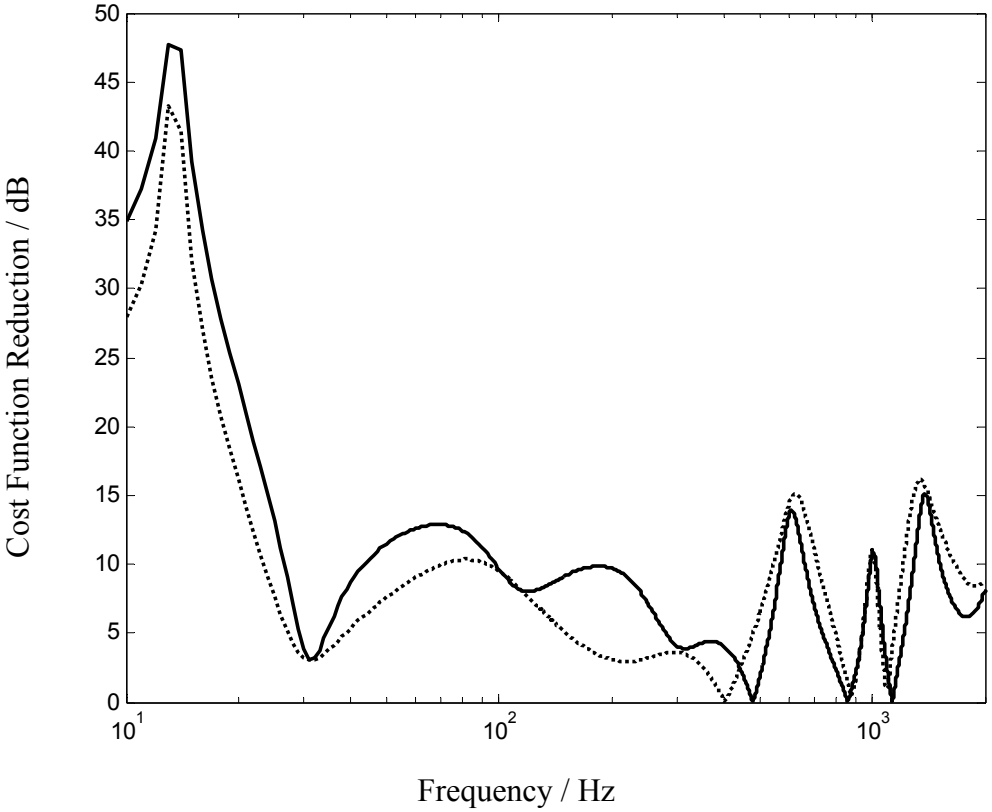

Figure 4.17. Simulations of the cost function reduction as a function of frequency of excitation. This was obtained by calculating the difference between the maximum value of the cost function and the minimum. The solid curve is the reduction achieved using the time averaged kinetic energy cost function (in dB re 1 J) and the dotted curve is the reduction achieved using the cost function which minimises the sum of the magnitude squared of the velocity at each end of the beam (in dB re $1\mathrm{m}^2\mathrm{s}^{-2}$). The simulated positions of the shakers were $x_1/l = 0.33$ and $x_2/l = 0.42$, the magnitude of the drive voltage applied to each shaker was the same.

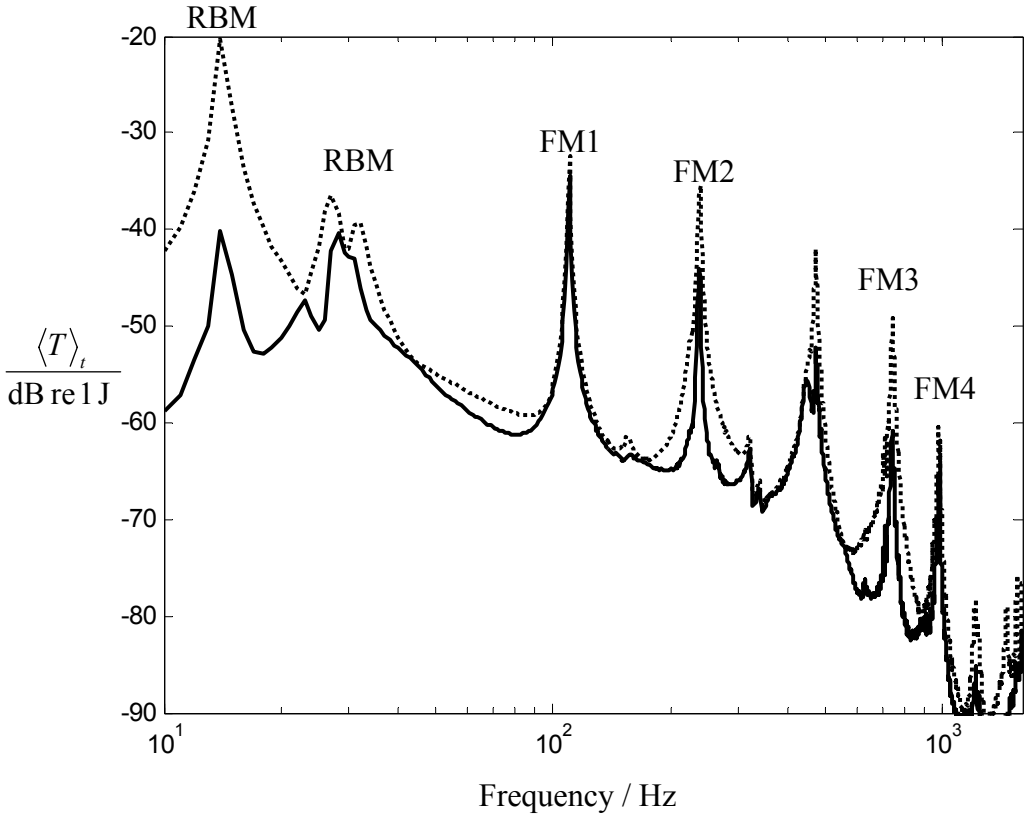

Figure 4.18. Experimental determination of the time averaged kinetic energy of the beam. The dotted curve shows the maximum and solid curve the minimum achieved by synchrophasing. The positions of the shakers were $x_1/l = 0.25$ and $x_2/l = 0.58$, the magnitude of the drive voltage applied to each shaker was the same. The figure shows the two rigid body modes (RBM) of the beam and the first 4 flexural modes (FM1 to FM4).

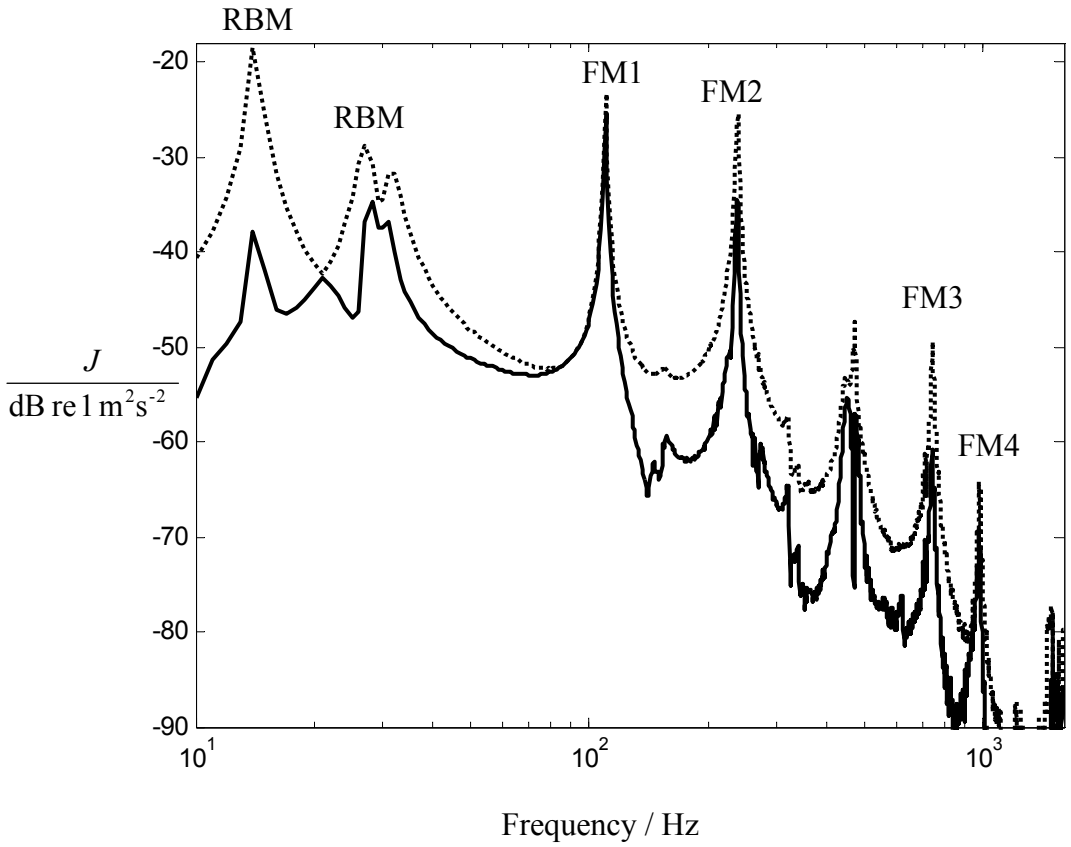

Figure 4.19. Experimental result showing the sum of the magnitude squared of the velocity at each end of the beam. The dotted curve shows the maximum and solid curve the minimum achieved by synchrophasing. The positions of the shakers were $x_1/l = 0.25$ and $x_2/l = 0.58$, the magnitude of the drive voltage applied to each shaker was the same. The figure shows the two rigid body modes (RBM) of the beam and the first 4 flexural modes (FM1 to FM4).

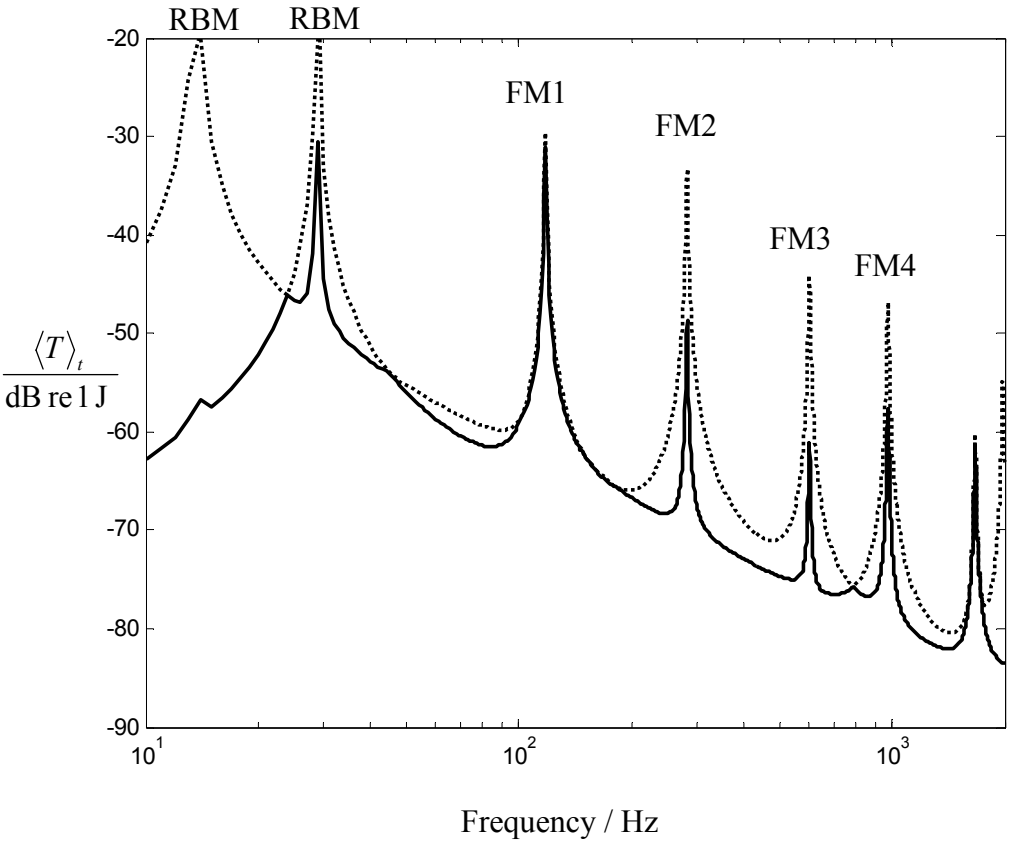

Figure 4.20. Simulations of the time averaged kinetic energy of the beam. The dotted curve shows the maximum and solid curve the minimum achieved by synchrophasing. The positions of the shakers were $x_1/l = 0.25$ and $x_2/l = 0.58$, the magnitude of the drive voltage applied to each shaker was the same. The figure shows the two rigid body modes (RBM) of the beam and the first 4 flexural modes (FM1 to FM4).

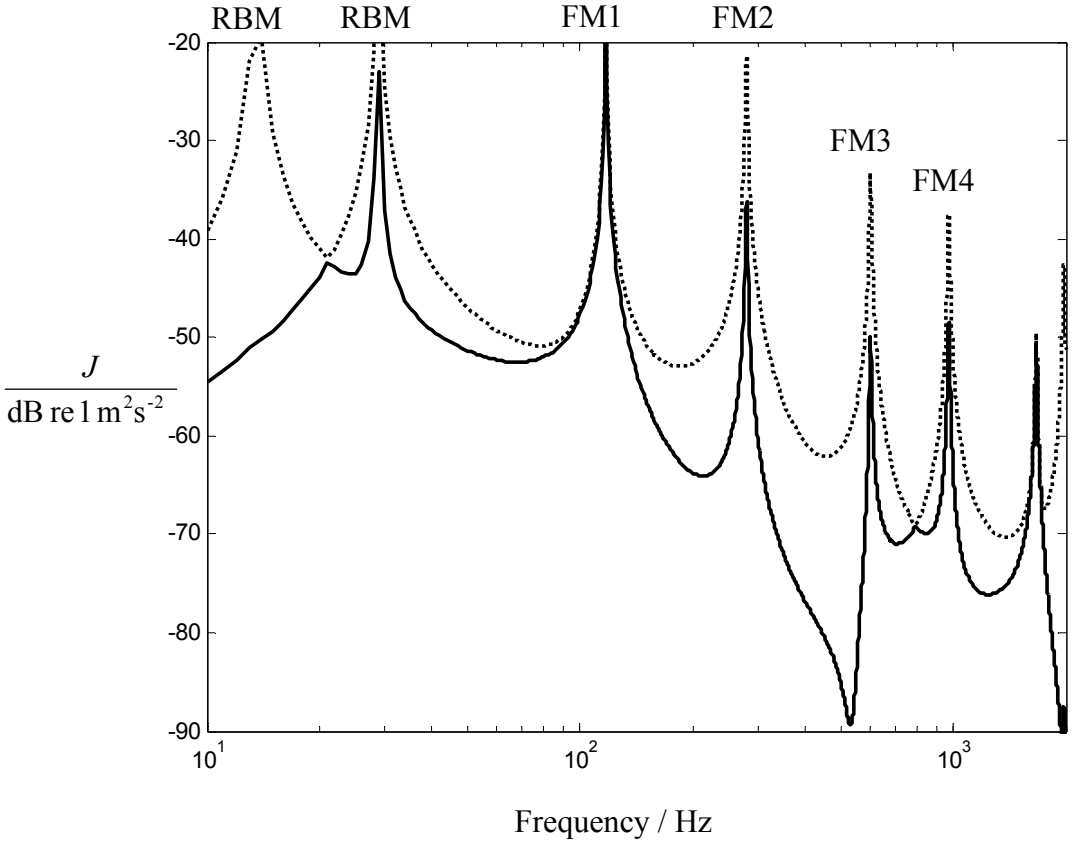

Figure 4.21. Simulations of the sum of the magnitude squared of the velocity at each end of the beam. The dotted curve shows the maximum and solid curve the minimum achieved by synchrophasing. The positions of the shakers were $x_1/l = 0.25$ and $x_2/l = 0.58$, the magnitude of the drive voltage applied to each shaker was the same.

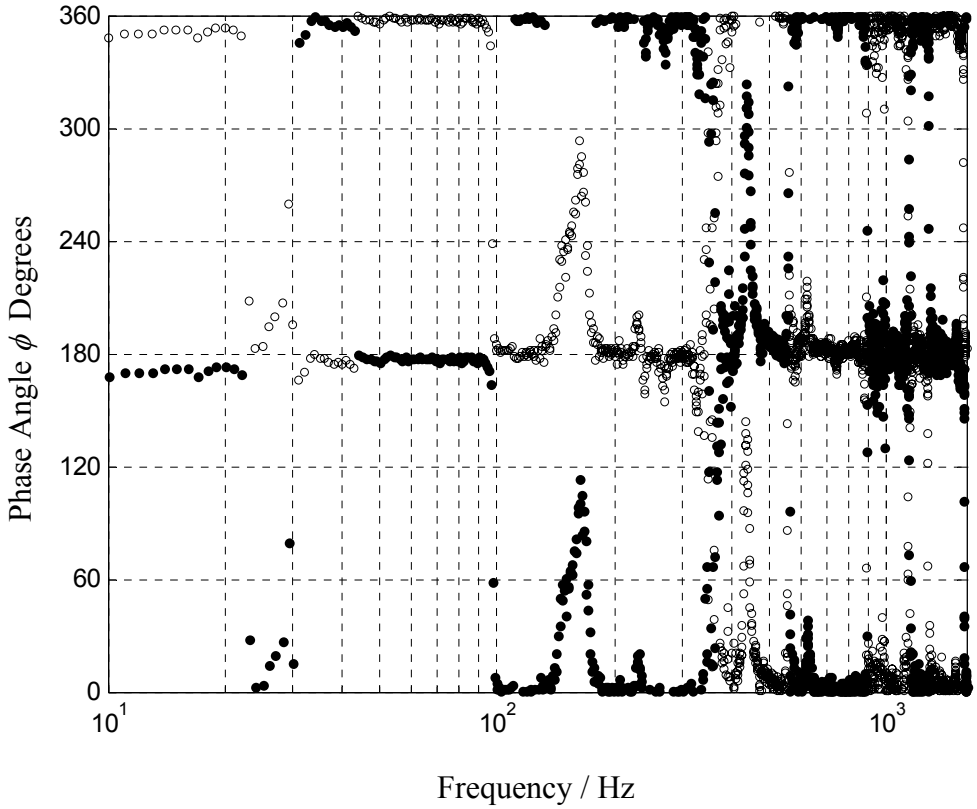

Figure 4.22. Experimental result showing the phase of the control source corresponding to the maximum and minimum of the time averaged kinetic energy. The clear dots show the phase to obtain the maximum kinetic energy and solid dots the phase to achieve the minimum by synchrophasing. The positions of the shakers were $x_1/l = 0.25$ and $x_2/l = 0.58$, the magnitude of the drive voltage applied to each shaker was the same.

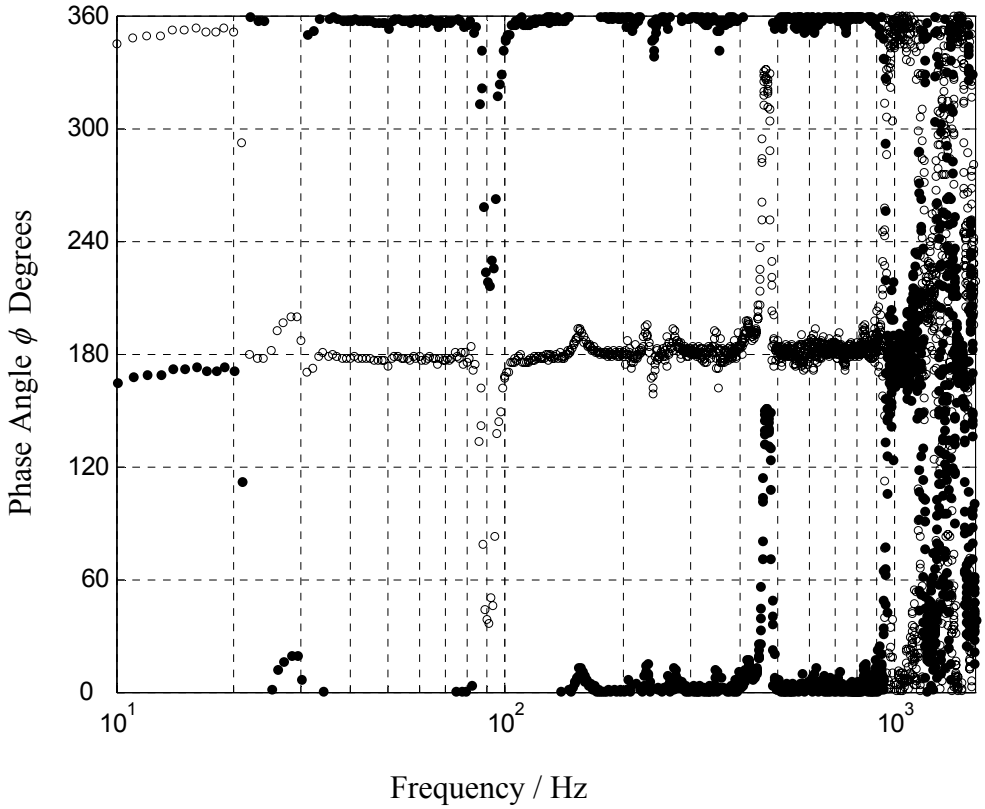

Figure 4.23. Experimental result showing the phase of the control source corresponding to the maximum and minimum of the cost function summing the magnitude squared of the velocity at each end of the beam. The clear dots show the phase to obtain the maximum value of the cost function and solid dots the phase to achieve the minimum by synchrophasing. The positions of the shakers were $x_1/l = 0.25$ and $x_2/l = 0.58$, the magnitude of the drive voltage applied to each shaker was the same.

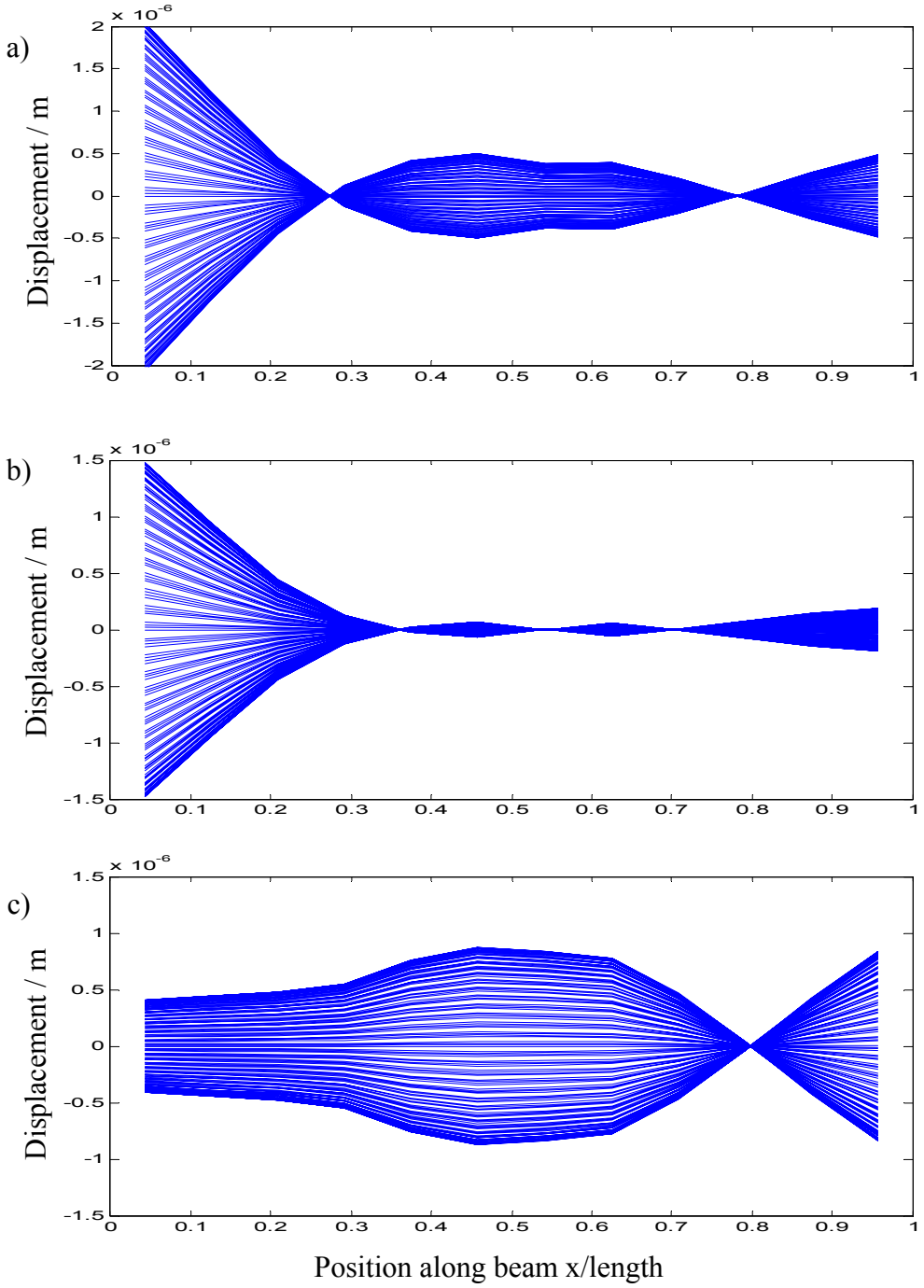

Figure 4.24. The measured displacement of the beam at 162 Hz when the phase of the control shaker was a) anti-phase with the reference, b) optimised to minimise the time averaged kinetic energy cost function, c) optimised to minimise the sum of the magnitudes of velocity squared at each end of the beam. The positions of the shakers were $x_1/l = 0.25$ and $x_2/l = 0.58$, the magnitude of the drive voltage applied to each shaker was the same.

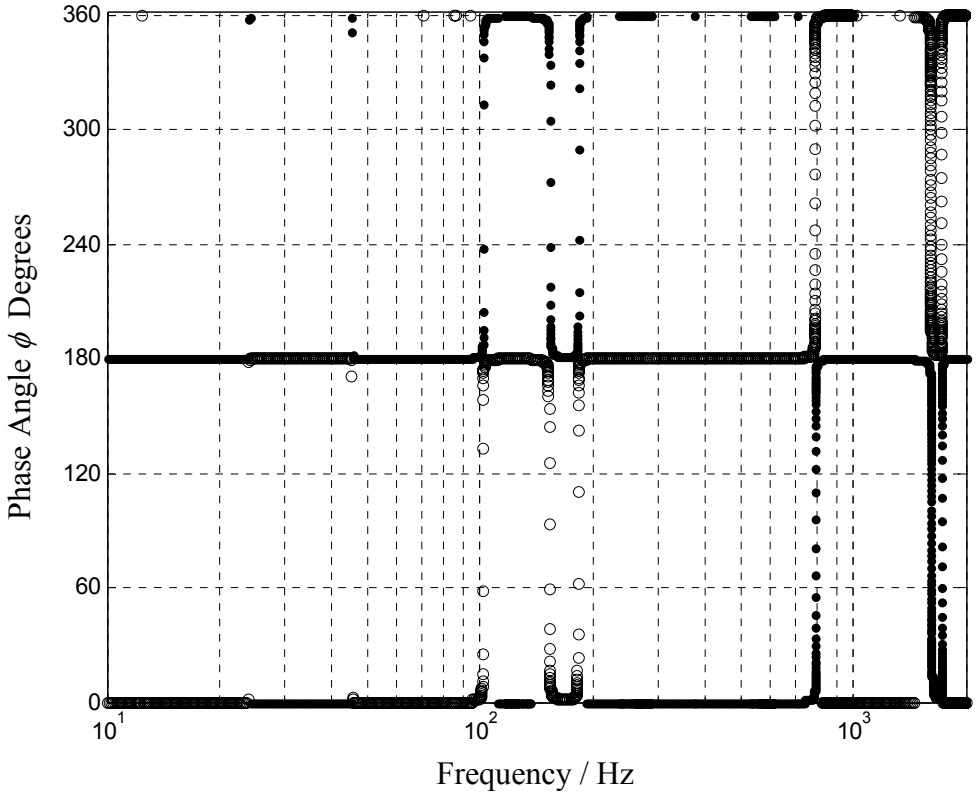

Figure 4.25. Simulations of the phase of the control source corresponding to the maximum and minimum of the time averaged kinetic energy. The clear dots show the phase to obtain the maximum kinetic energy and solid dots the phase to achieve the minimum by synchrophasing. The positions of the shakers were $x_1/l = 0.25$ and $x_2/l = 0.58$, the magnitude of the drive voltage applied to each shaker was the same.

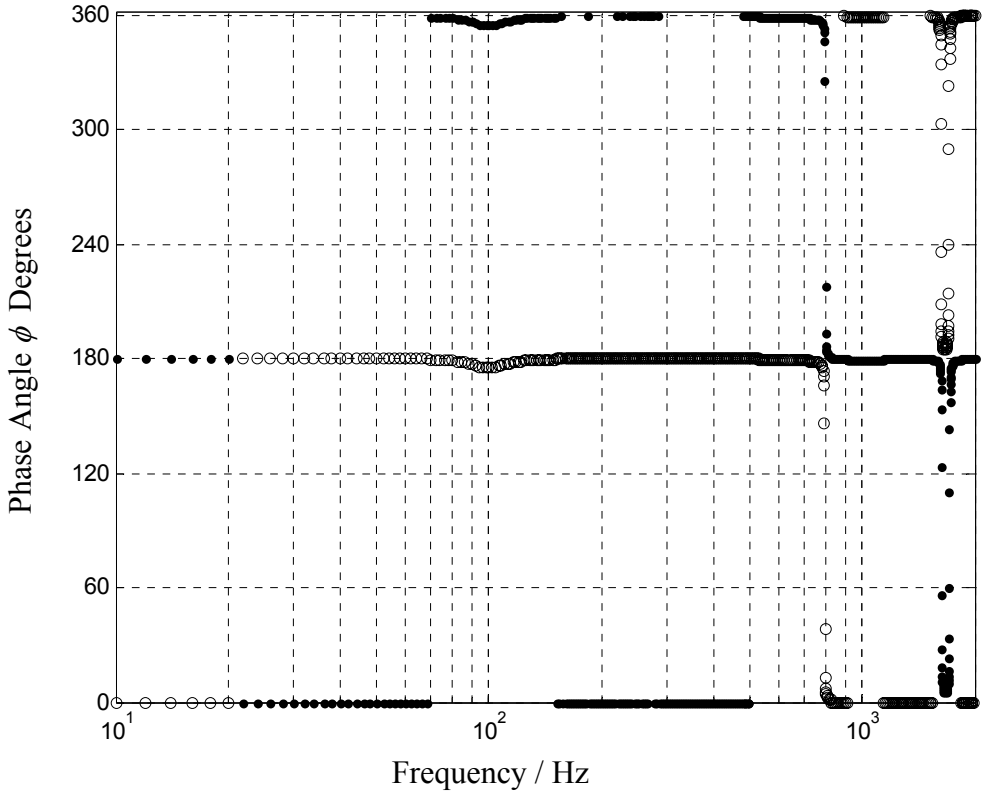

Figure 4.26. Simulations of the phase of the control source corresponding to the maximum and minimum of the cost function summing the magnitude squared of the velocity at each end of the beam. The clear dots show the phase to obtain the maximum value of the cost function and solid dots the phase to achieve the minimum by synchrophasing. The positions of the shakers were $x_1/l = 0.25$ and $x_2/l = 0.58$, the magnitude of the drive voltage applied to each shaker was the same.

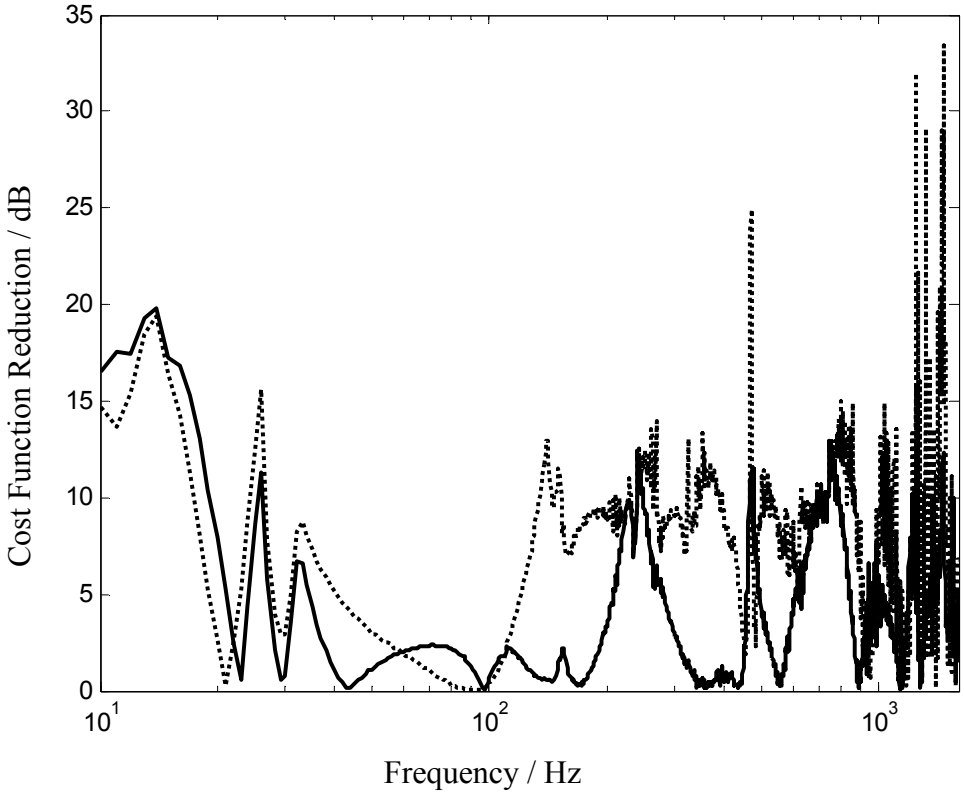

Figure 4.27. Experimental result showing the cost function reduction as a function of the excitation frequency. This was obtained by calculating the difference between the maximum value of the cost function and the minimum. The solid curve is the reduction achieved using the time averaged kinetic energy cost function (in dB re 1 J) and the dotted curve is the reduction achieved using the cost function which minimises the sum of the magnitude squared of the velocity at each end of the beam (in dB re $1\mathrm{m}^2\mathrm{s}^{-2}$). The positions of the shakers were $x_1/l = 0.25$ and $x_2/l = 0.58$, the magnitude of the drive voltage applied to each shaker was the same.

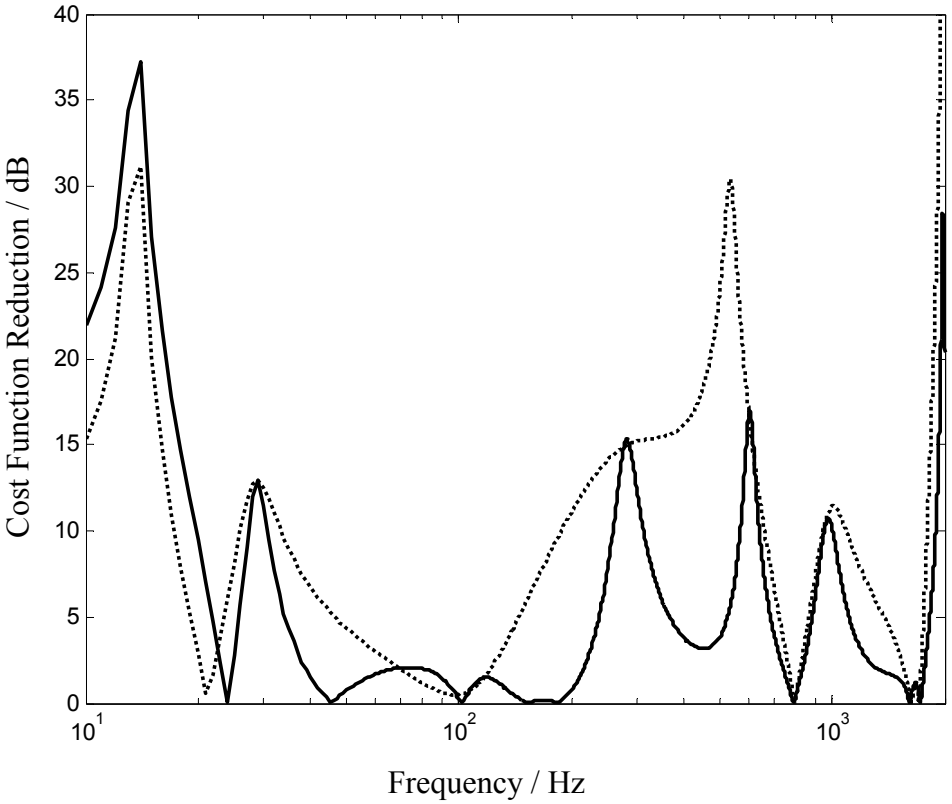

Figure 4.28. Simulations of the cost function reduction as a function of the excitation frequency. This was obtained by calculating the difference between the maximum value of the cost function and the minimum. The solid curve is the reduction achieved using the time averaged kinetic energy cost function (in dB re 1 J) and the dotted curve is the reduction achieved using the cost function which minimises the sum of the magnitude squared of the velocity at each end of the beam (in dB re $1\mathrm{m}^2\mathrm{s}^{-2}$). The positions of the shakers were $x_1/l = 0.25$ and $x_2/l = 0.58$, the simulated magnitude of the drive voltage applied to each shaker was the same.

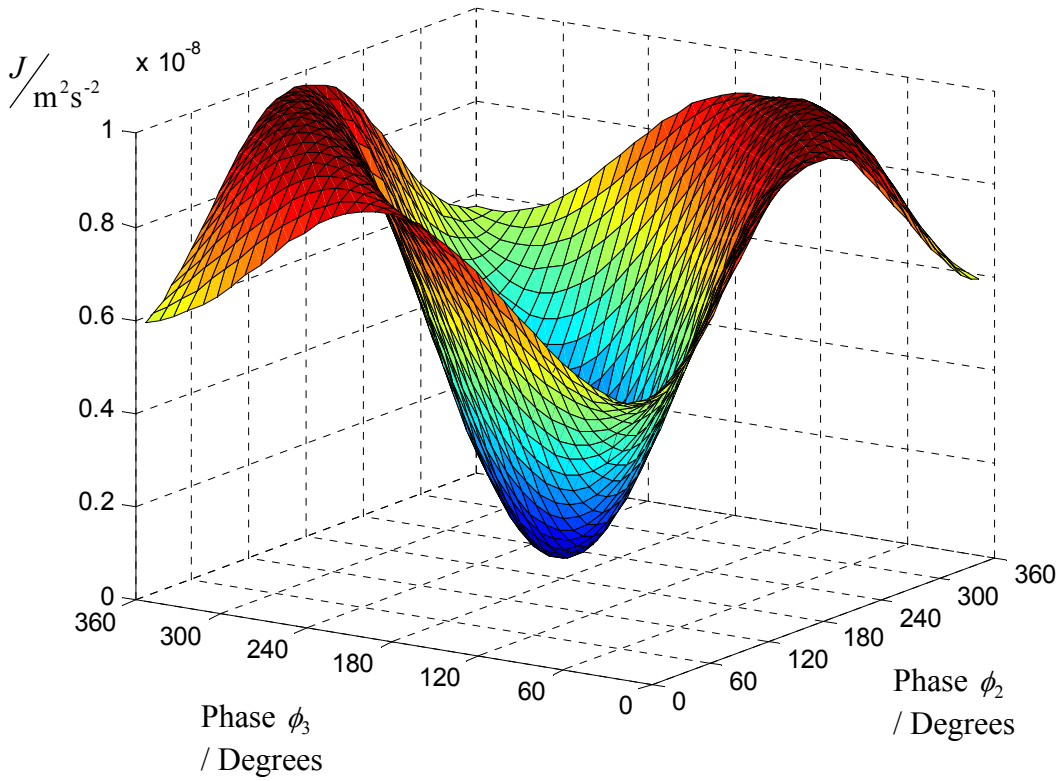

Figure 4.29. Experimentally obtained cost function surface at 70 Hz, using a cost function which sums the magnitude squared of the velocity at each end of the beam. The positions of the shakers were $x_1/l = 0.375$ (phase reference), $x_2/l = 0.21$ and $x_3/l = 0.71$. The magnitude of the drive voltage applied to each shaker was the same. The synchrophasing shaker phases ϕ_2 and ϕ_3 were varied from 0° to 350° in 10° steps.

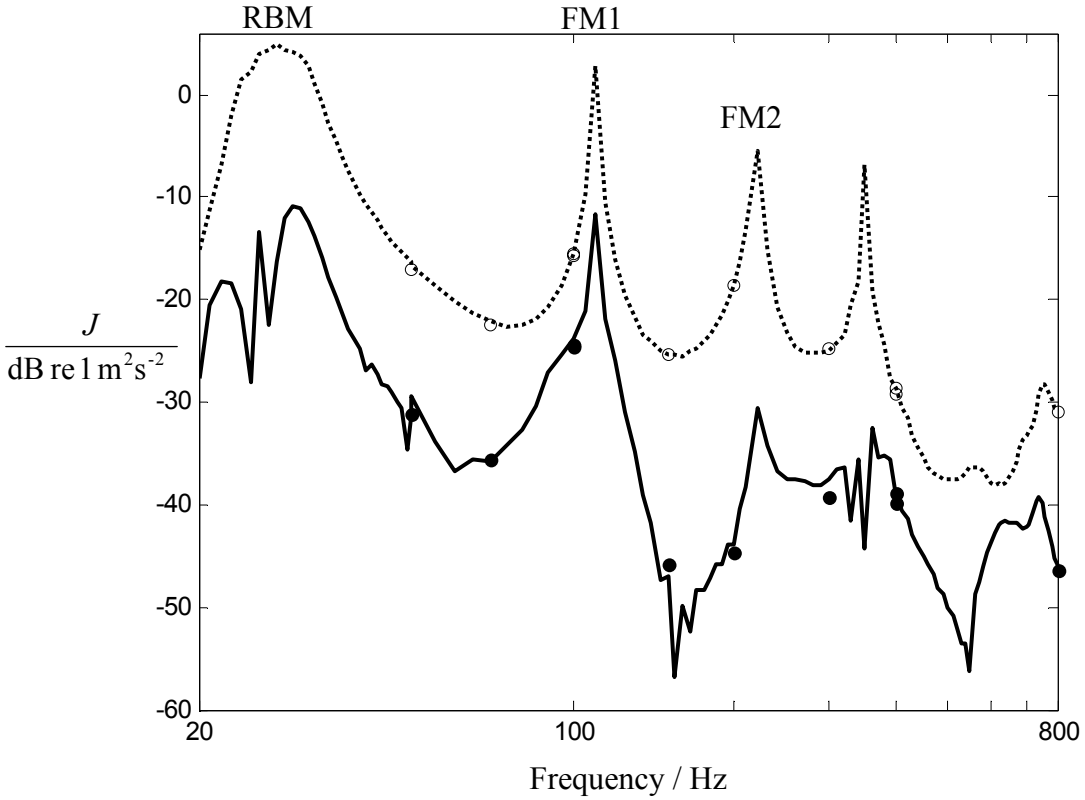

Figure 4.30. Experimental result showing the sum of the magnitude squared of the velocity at each end of the beam. The dotted curve shows the maximum and solid curve the minimum achieved by synchrophasing using Propeller Signature Theory. The dots show the cost function maximum – clear and minimum - solid obtained from searching over a range of angles. The positions of the shakers were $x_1/l = 0.375$ (shaker used as the phase reference), $x_2/l = 0.21$ and $x_3/l = 0.71$. The magnitude of the drive voltage applied to each shaker was the same.

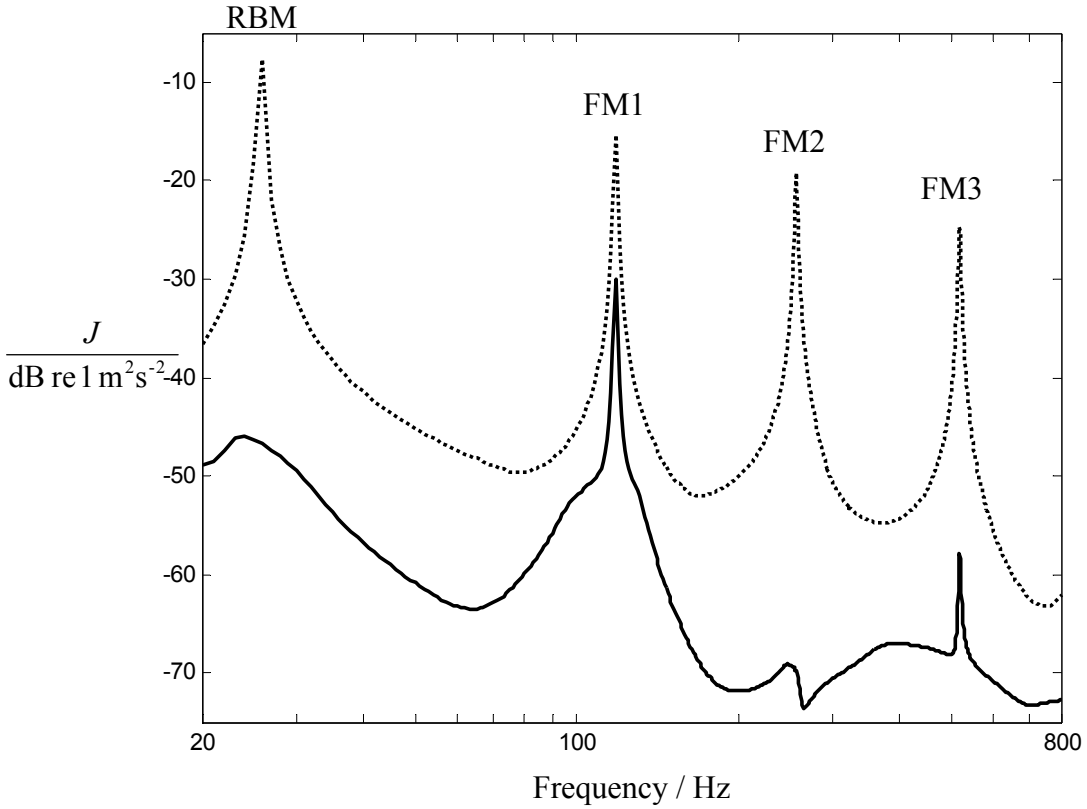

Figure 4.31. Simulations of sum of the magnitude squared of the velocity at each end of the beam. The dotted curve shows the maximum and solid curve the minimum achieved by synchrophasing. The simulated positions of the shakers were $x_1/l = 0.375$ (shaker used as the phase reference), $x_2/l = 0.21$ and $x_3/l = 0.71$, the simulated magnitude of the drive voltage applied to each shaker was the same.

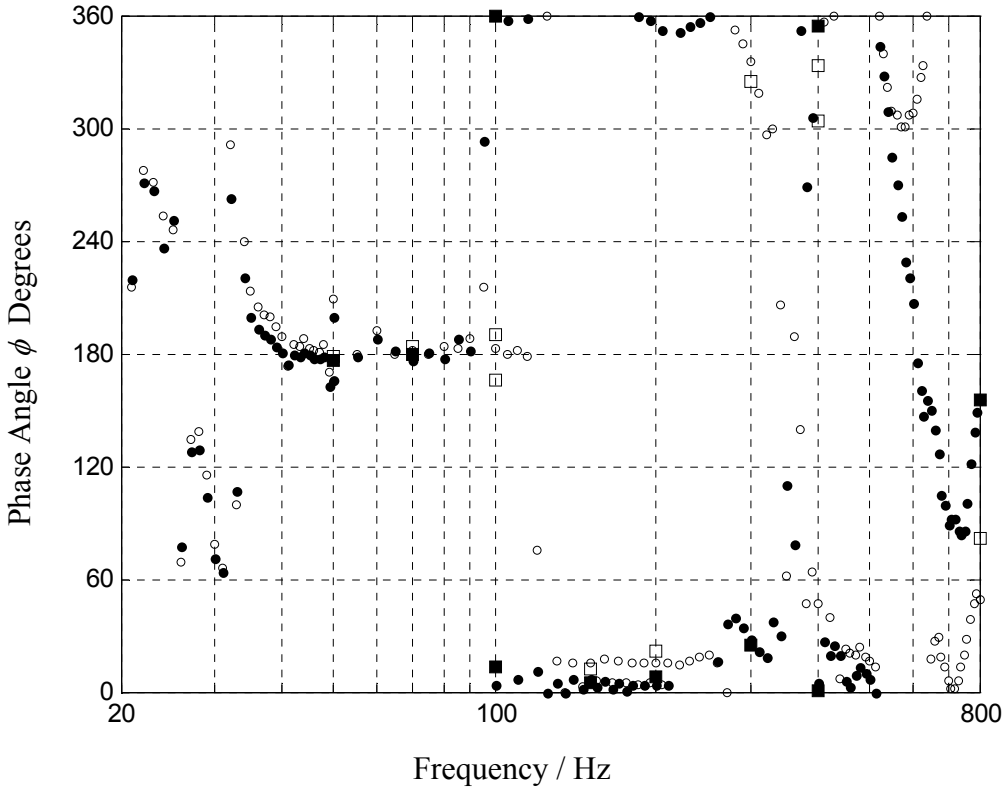

Figure 4.32. Experimental result showing the control phases ϕ_2 and ϕ_3 required to minimise the cost function summing the magnitude squared of the velocity at each end of the beam.

The solid dots show the phase required for the control machine at x_2 to obtain the minimum value of the cost function, and clear dots show the phase required for the control machine at x_3 to achieve the minimum by synchrophasing using propeller signature theory.

The squares show the required phase angles to minimise the cost function obtained by searching over a range of angles. The solid squares are the phases for the control machine at x_2 and the clear squares the control machine at x_3

The positions of the shakers were $x_1/l = 0.375$ (phase reference), $x_2/l = 0.21$ and $x_3/l = 0.71$. The magnitude of the drive voltage applied to each shaker was the same.

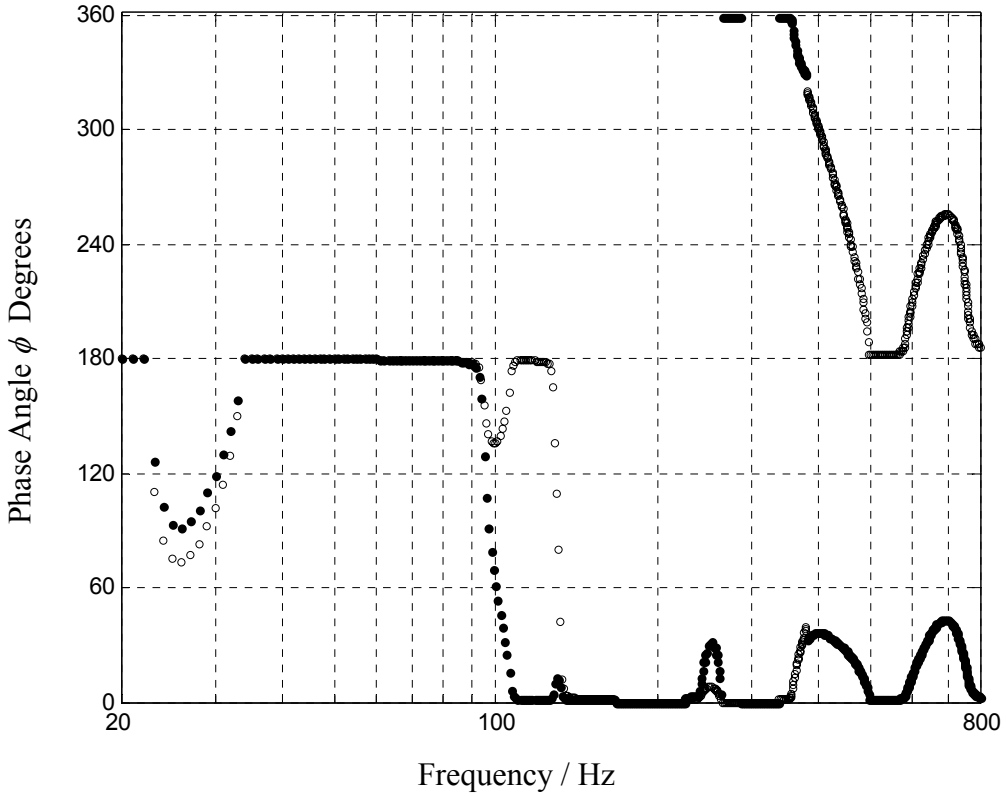

Figure 4.33. Simulations of the control phases ϕ_2 and ϕ_3 required to minimise the cost function summing the magnitude squared of the velocity at each end of the beam.

The solid dots show the phase required for the control machine at x_2 to obtain the minimum value of the cost function, and clear dots show the phase required for the control machine at x_3 to achieve the minimum by synchrophasing using propeller signature theory.

The positions of the shakers were $x_1/l = 0.375$ (phase reference), $x_2/l = 0.21$ and $x_3/l = 0.71$. The magnitude of the drive voltage applied to each shaker was the same.

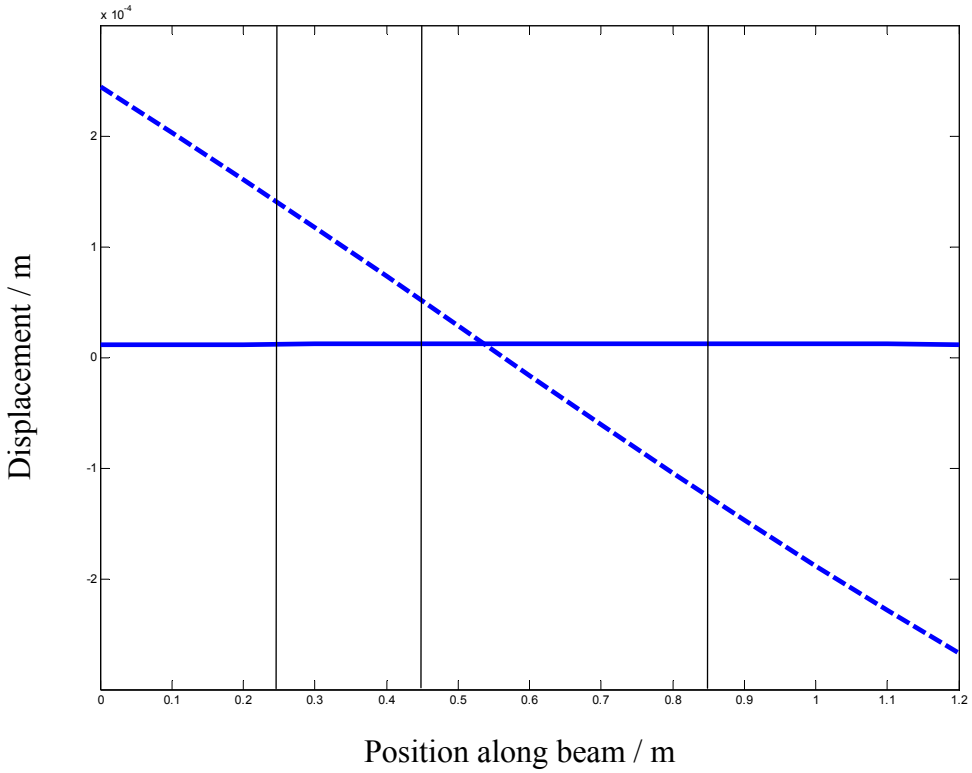

Figure 4.34. Simulations of the Operational Deflection Shape at 26 Hz corresponding to the rotational rigid body mode.

The dotted line is the ODS when just the reference vibrating source is driving the beam, although the two control machines are present. The solid line is the ODS when all three sources are driving the beam. The phases of the control sources are the values calculated to minimise the cost function. The magnitude of the drive voltage applied to each shaker was the same.

The positions of the shakers, shown as lines, were $x_1/l = 0.375$ (phase reference), $x_2/l = 0.21$ and $x_3/l = 0.71$.

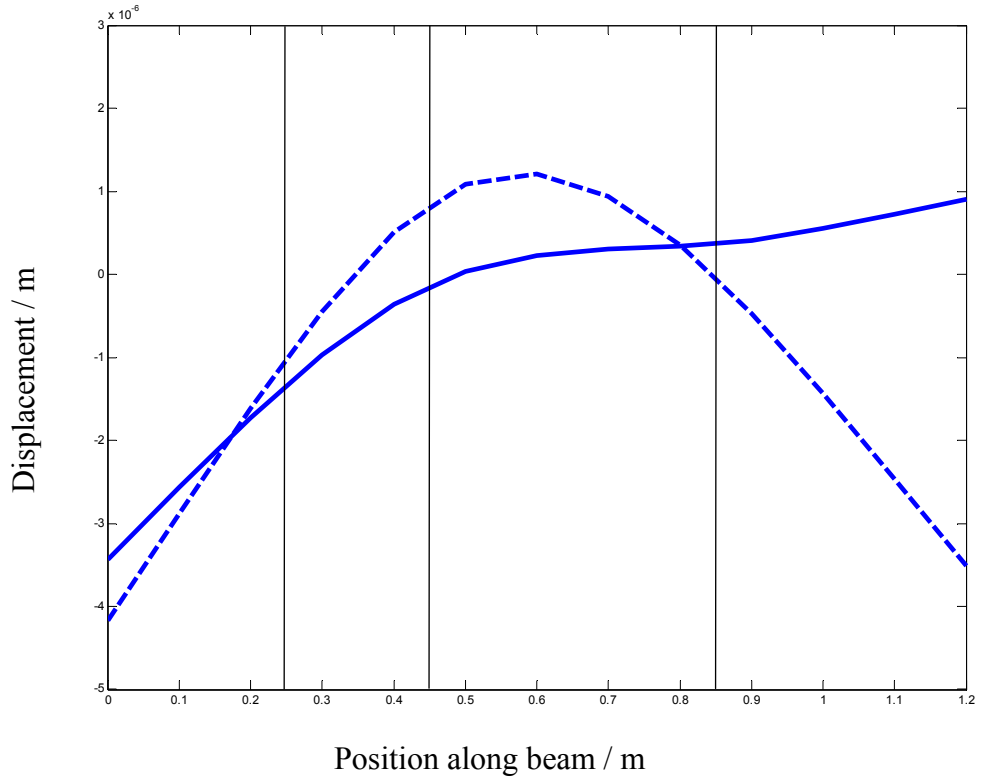

Figure 4.35. Simulations of the Operational Deflection Shape at 118 Hz corresponding to the first flexural mode.

The dotted line is the ODS when just the reference vibrating source is driving the beam, although the two control machines are present. The solid line is the ODS when all three sources are driving the beam. The phases of the control sources are the values calculated to minimise the cost function. The magnitude of the drive voltage applied to each shaker was the same.

The positions of the shakers, shown as lines, were $x_1/l = 0.375$ (phase reference), $x_2/l = 0.21$ and $x_3/l = 0.71$.

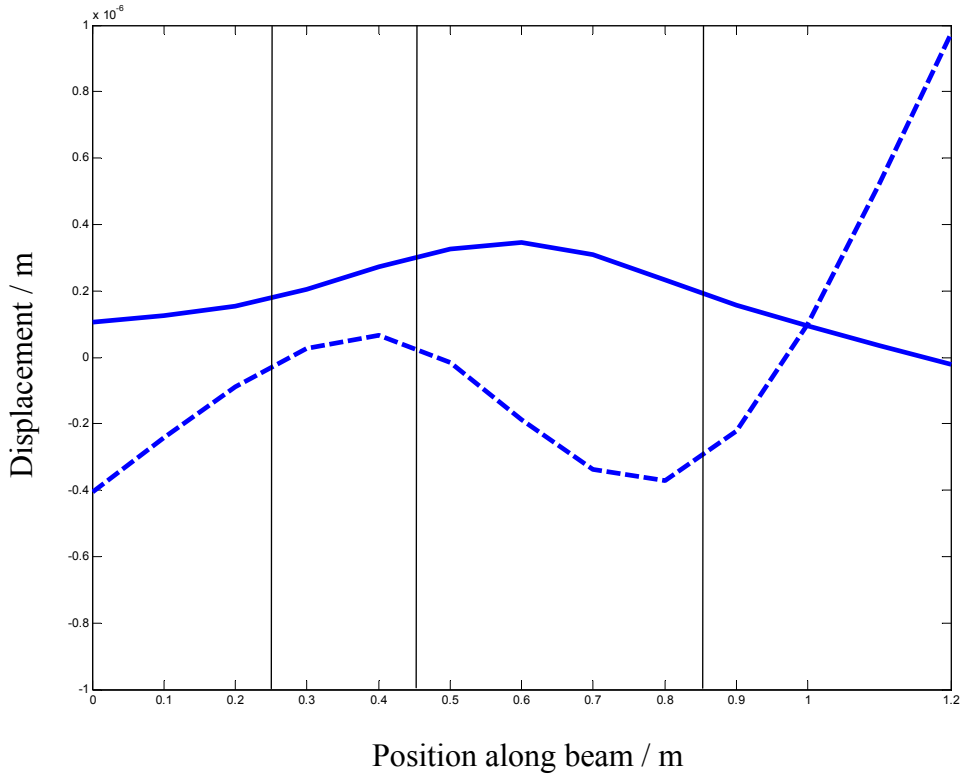

Figure 4.36. Simulations of the Operational Deflection Shape at 258 Hz corresponding to the second flexural mode.

The dotted line is the ODS when just the reference vibrating source is driving the beam, although the two control machines are present. The solid line is the ODS when all three sources are driving the beam. The phases of the control sources are the values calculated to minimise the cost function. The magnitude of the drive voltage applied to each shaker was the same.

The positions of the shakers, shown as lines, were $x_1/l = 0.375$ (phase reference), $x_2/l = 0.21$ and $x_3/l = 0.71$.

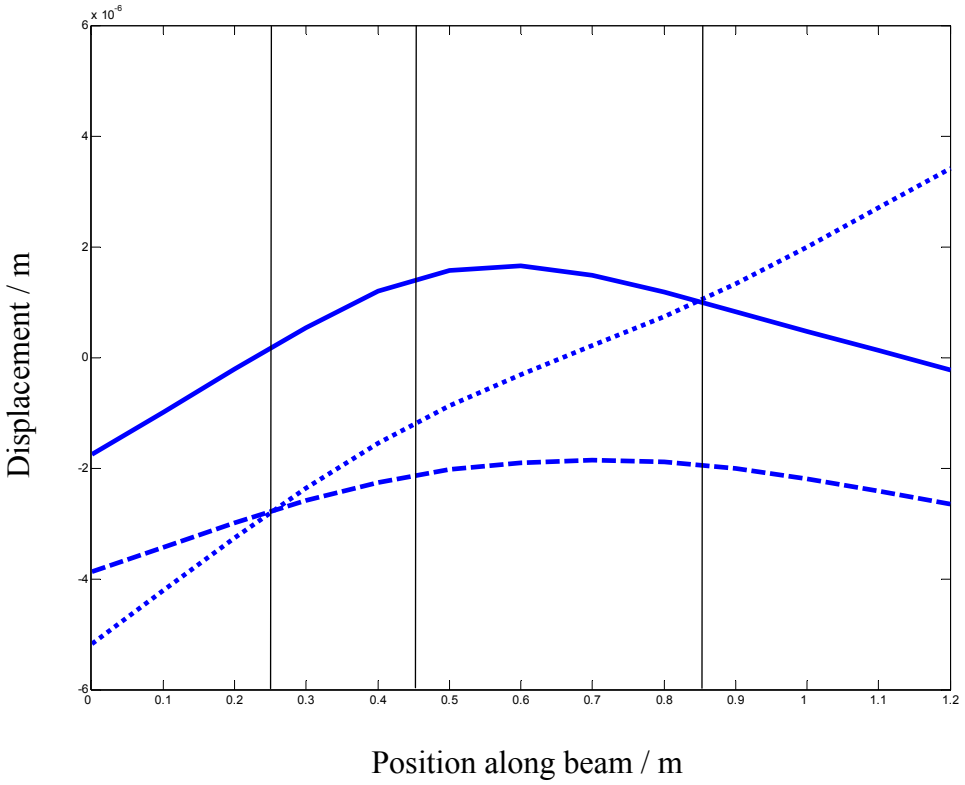

Figure 4.37. Simulations of the Operational Deflection Shape at 80 Hz obtained by changing the control phases ϕ_2 and ϕ_3.

For the solid line $\phi_2 = 180^\circ$ and $\phi_3 = 180^\circ$ respectively.

For the dotted line $\phi_2 = 0^\circ$ and $\phi_3 = 180^\circ$ respectively.

For the dashed line $\phi_2 = 0^\circ$ and $\phi_3 = 0^\circ$ respectively.

The magnitude of the drive voltage applied to each shaker was the same.

The positions of the shakers, shown as lines, were $x_1/l = 0.375$ (phase reference), $x_2/l = 0.21$ and $x_3/l = 0.71$.

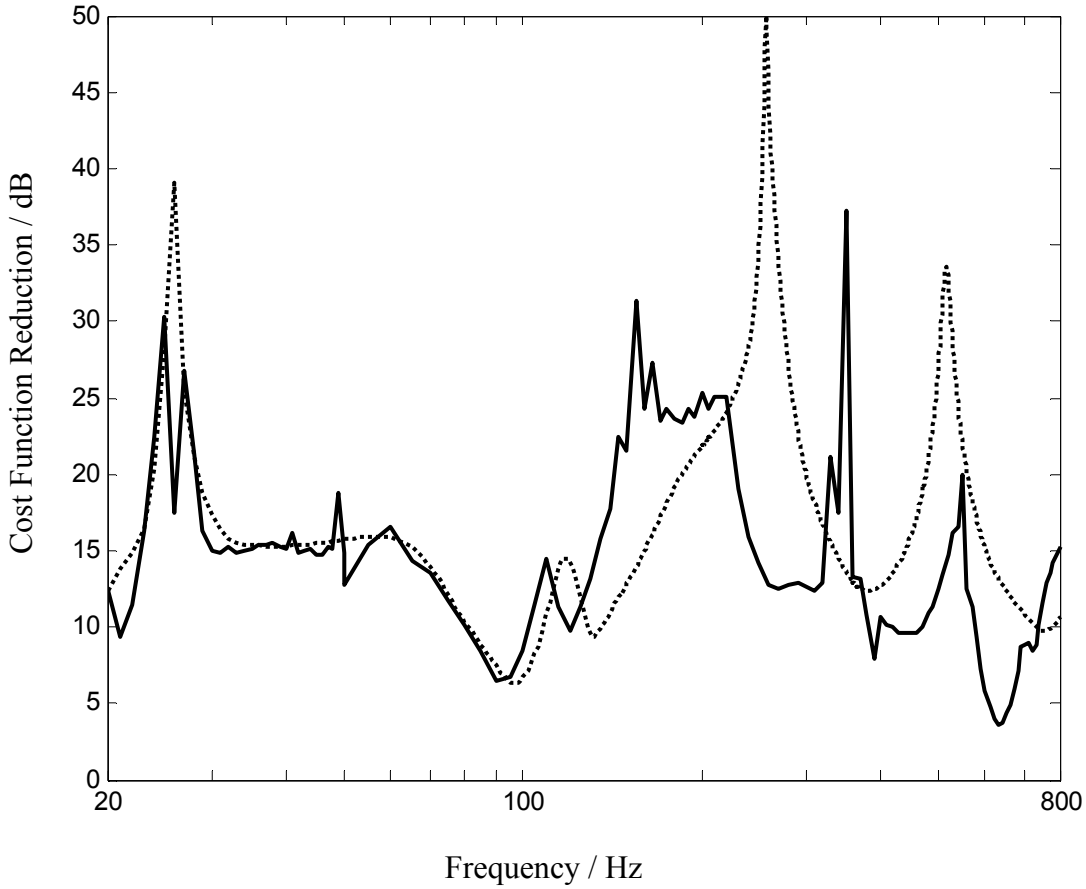

Figure 4.38. Comparison of the cost function reduction obtained experimentally by synchrophasing with that predicted using simulations. The solid curve is the reduction achieved experimentally using the cost function which minimises the sum of the magnitude squared of the velocity at each end of the beam. The dotted curve is the reduction of the same cost function obtained by simulation. The positions of the shakers were $x_1/l = 0.375$ (phase reference), $x_2/l = 0.21$ and $x_3/l = 0.71$. The magnitude of the drive voltage applied to each shaker was the same.

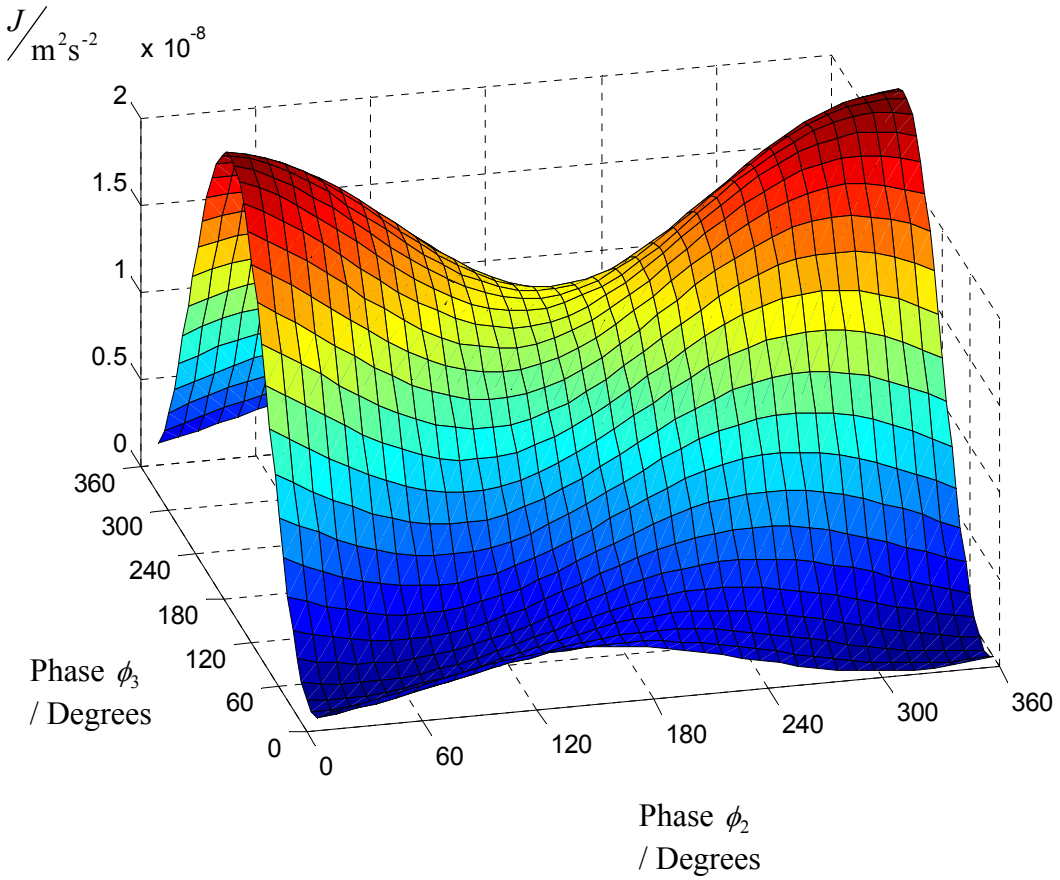

Figure 4.39. Experimental cost function surface at 200 Hz, using a cost function which sums the magnitude squared of the velocity at each end of the beam. The positions of the shakers were $x_1/l = 0.375$ (phase reference), $x_2/l = 0.21$ and $x_3/l = 0.71$, the magnitude of the drive voltage applied to each shaker was the same. The synchrophasing shaker phases ϕ_2 and ϕ_3 were varied from 0° to 350° in 10° steps.

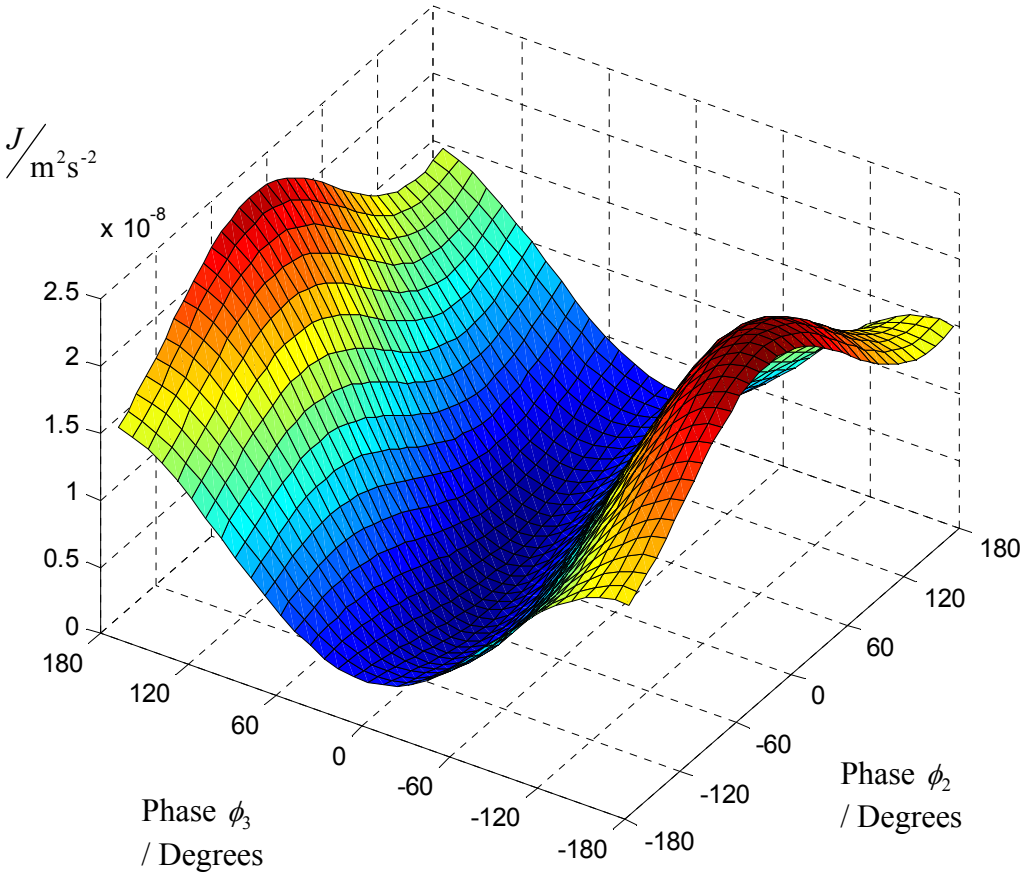

Figure 4.40. Experimental cost function surface at 200 Hz, using a cost function which sums the magnitude squared of the velocity at each end of the beam. The positions of the shakers were $x_1/l = 0.375$ (phase reference), $x_2/l = 0.21$ and $x_3/l = 0.71$, the magnitude of the drive voltage applied to each shaker was the same. The synchrophasing shaker phases ϕ_2 and ϕ_3 were varied from 0° to 350° in 10° steps. For this figure, the data are plotted as if the shaker phases were varied from -170° to 180° to better show the small variation of the cost function with ϕ_2

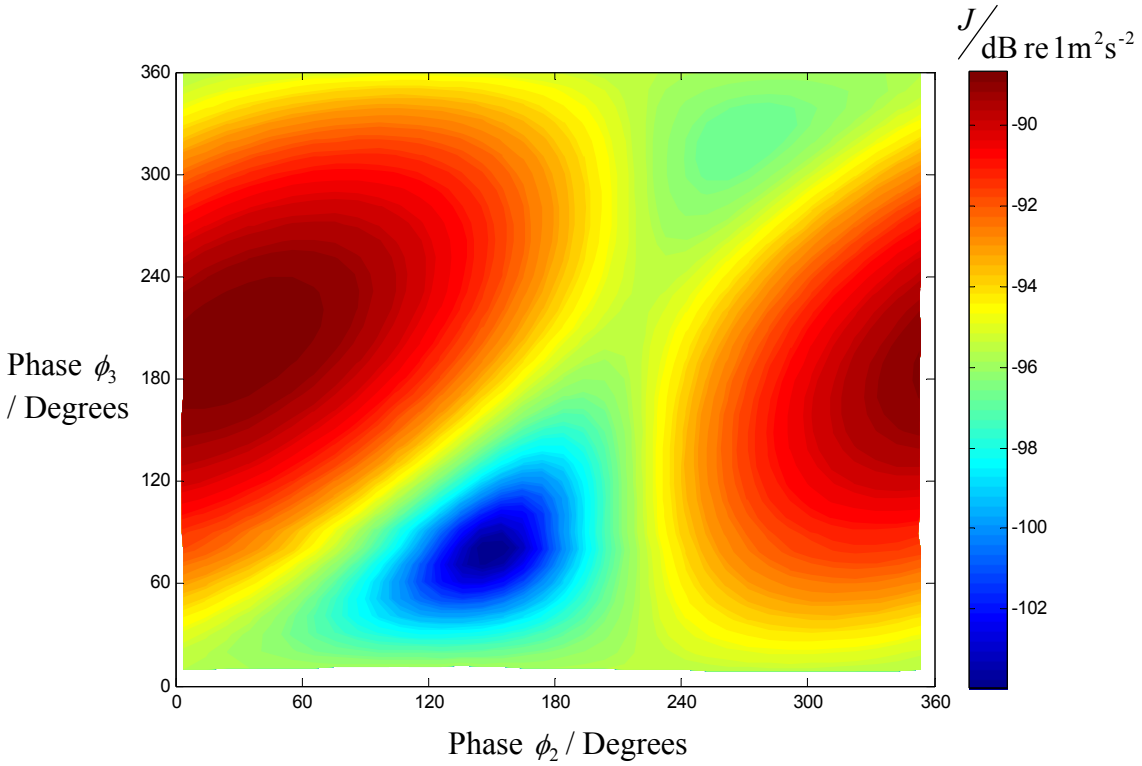

Figure 4.41. Experimental cost function surface at 800 Hz, using the cost function which sums the magnitude squared of the velocity at each end of the beam. The positions of the shakers were $x_1/l = 0.375$ (phase reference), $x_2/l = 0.21$ and $x_3/l = 0.71$, the magnitude of the drive voltage applied to each shaker was the same. The synchrophasing shaker phases ϕ_2 and ϕ_3 were varied from a nominal 0° to 350° in 10° steps.

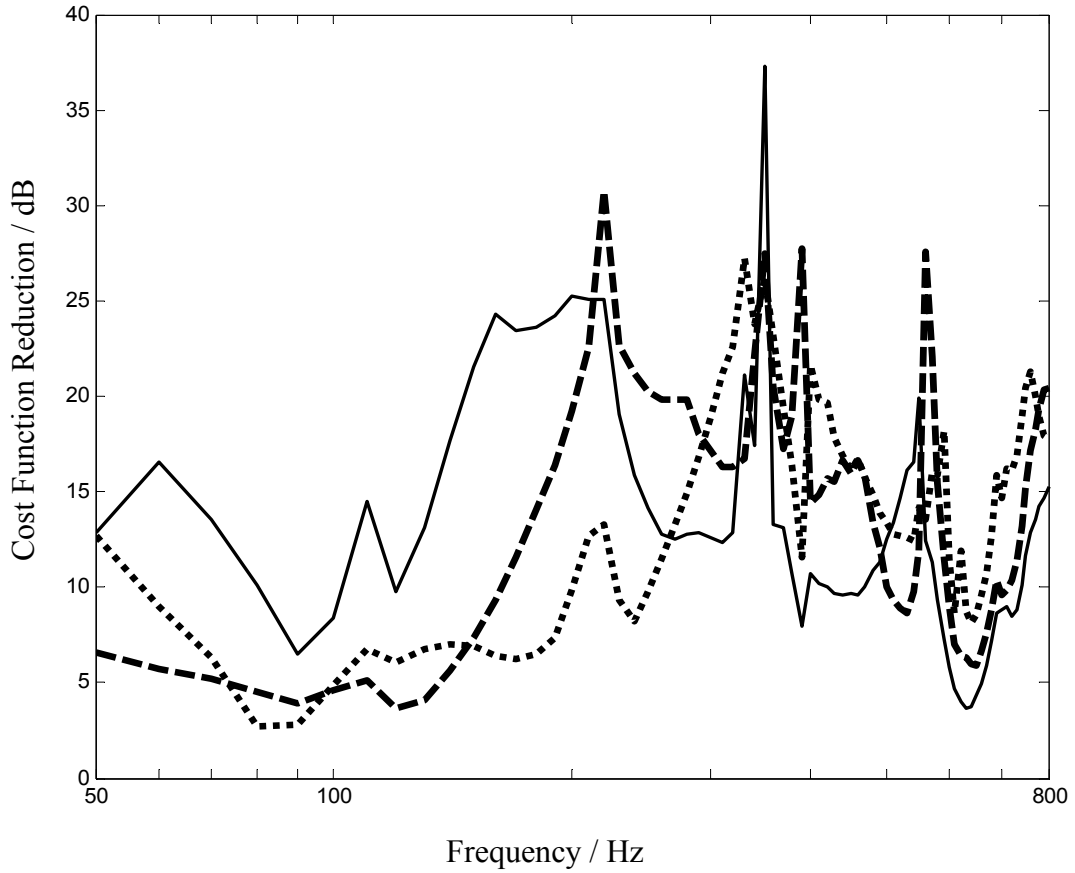

Figure 4.42. Comparison of the cost function reduction obtained experimentally by synchrophasing when the magnitude of the drive voltage applied to each shaker is adjusted. A scaling factor λ_n is used to denote the magnitude of the n^{th} control source drive voltage with respect to the reference source.

The solid curve: $\lambda_2 = 1$ and $\lambda_3 = 1$.
The dotted curve: $\lambda_2 = 2/3$ and $\lambda_3 = 1/3$.
The dashed curve: $\lambda_2 = 1/3$ and $\lambda_3 = 2/3$.

The positions of the three shakers were $x_1/l = 0.375$ (phase reference), $x_2/l = 0.21$ and $x_3/l = 0.71$.

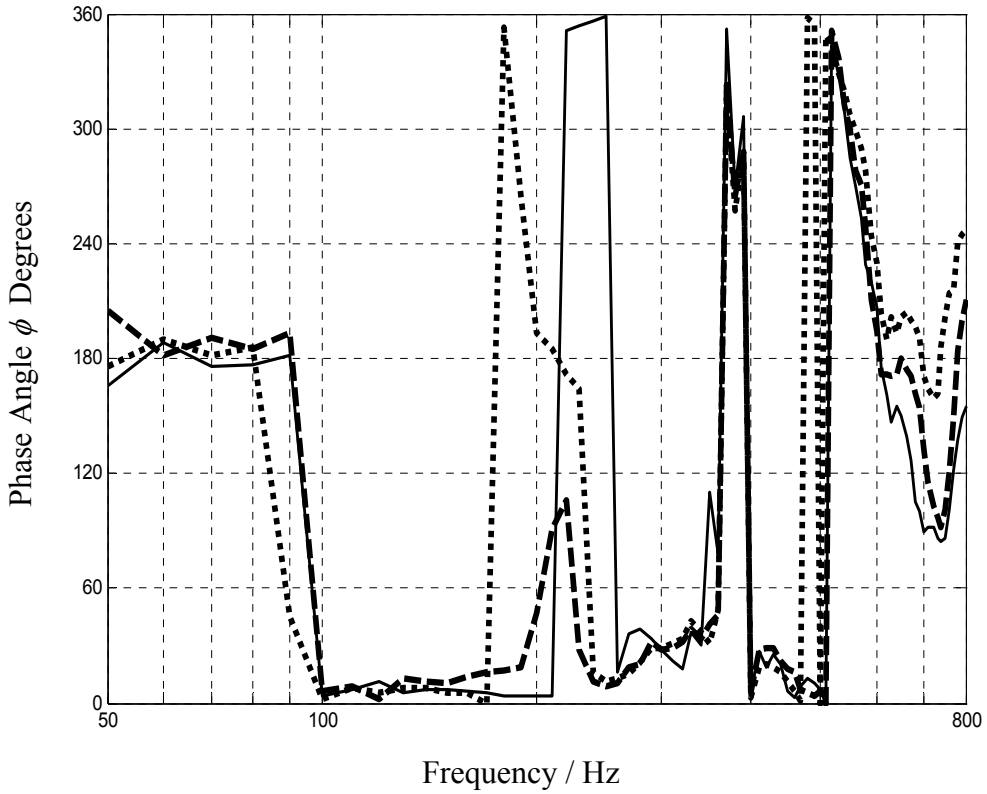

Figure 4.43. Comparison of the optimum synchrophase angles for ϕ_2 determined experimentally for the control machine at x_2, to achieve the minimum value of the cost function, when the magnitude of the drive voltage applied to each shaker is adjusted. A scaling factor λ_n is used to denote the magnitude of the n^{th} control source drive voltage with respect to the reference source.

The solid curve: $\lambda_2 = 1$ and $\lambda_3 = 1$.
The dotted curve: $\lambda_2 = 2/3$ and $\lambda_3 = 1/3$.
The dashed curve: $\lambda_2 = 1/3$ and $\lambda_3 = 2/3$.

The positions of the shakers were $x_1/l = 0.375$ (phase reference), $x_2/l = 0.21$ and $x_3/l = 0.71$.

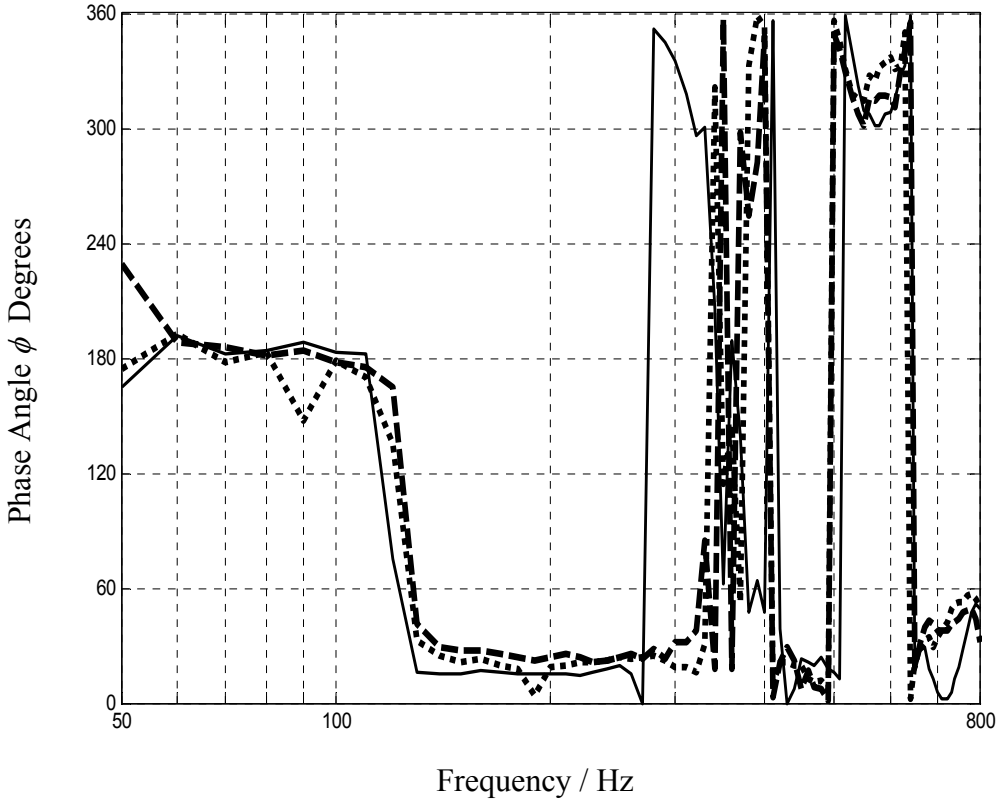

Figure 4.44. Comparison of the optimum synchrophase angles for ϕ_3 determined experimentally for the control machine at x_3, to achieve the minimum value of the cost function, when the magnitude of the drive voltage applied to each shaker is adjusted. A scaling factor λ_n is used to denote the magnitude of the n^{th} control source drive voltage with respect to the reference source.

The solid curve: $\lambda_2 = 1$ and $\lambda_3 = 1$.
The dotted curve: $\lambda_2 = 2/3$ and $\lambda_3 = 1/3$.
The dashed curve: $\lambda_2 = 1/3$ and $\lambda_3 = 2/3$.

The positions of the shakers were $x_1/l = 0.375$ (phase reference), $x_2/l = 0.21$ and $x_3/l = 0.71$.

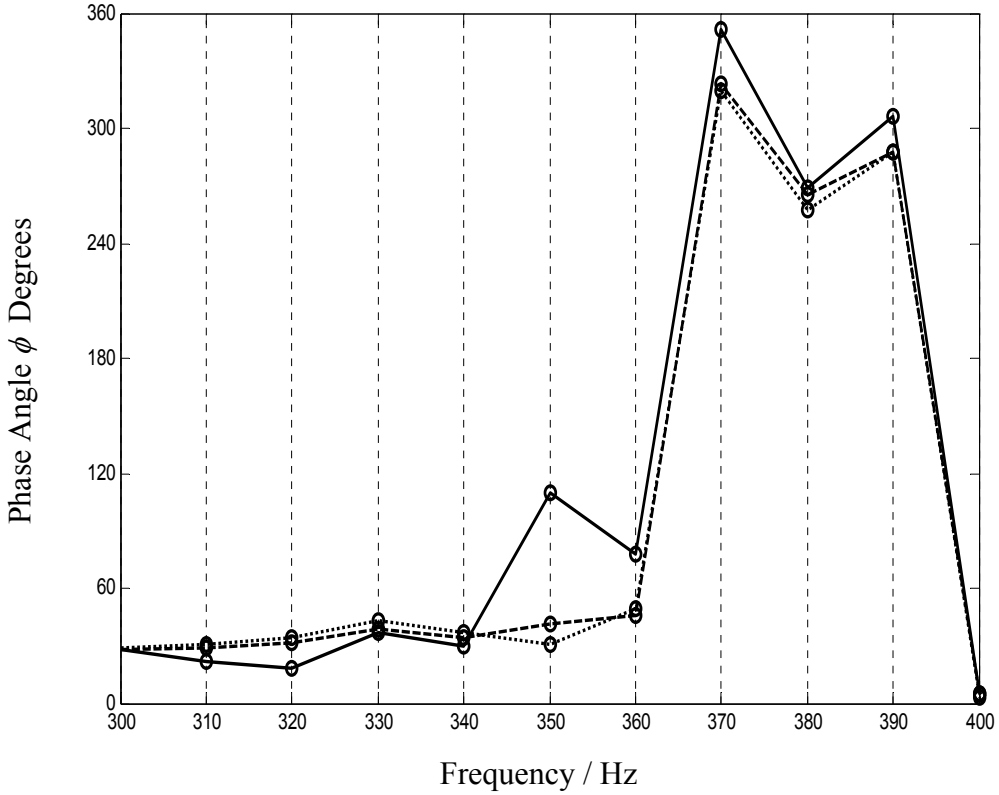

Figure 4.45. Comparison of the optimum synchrophase angles for ϕ_2 determined experimentally for the control machine at x_2, to achieve the minimum value of the cost function, when the magnitude of the drive voltage applied to each shaker is adjusted. A scaling factor λ_n is used to denote the magnitude of the n^{th} control source drive voltage with respect to the reference source.

The solid curve: $\lambda_2 = 1$ and $\lambda_3 = 1$.
The dotted curve: $\lambda_2 = 2/3$ and $\lambda_3 = 1/3$.
The dashed curve: $\lambda_2 = 1/3$ and $\lambda_3 = 2/3$.

The positions of the shakers were $x_1/l = 0.375$ (phase reference), $x_2/l = 0.21$ and $x_3/l = 0.71$.

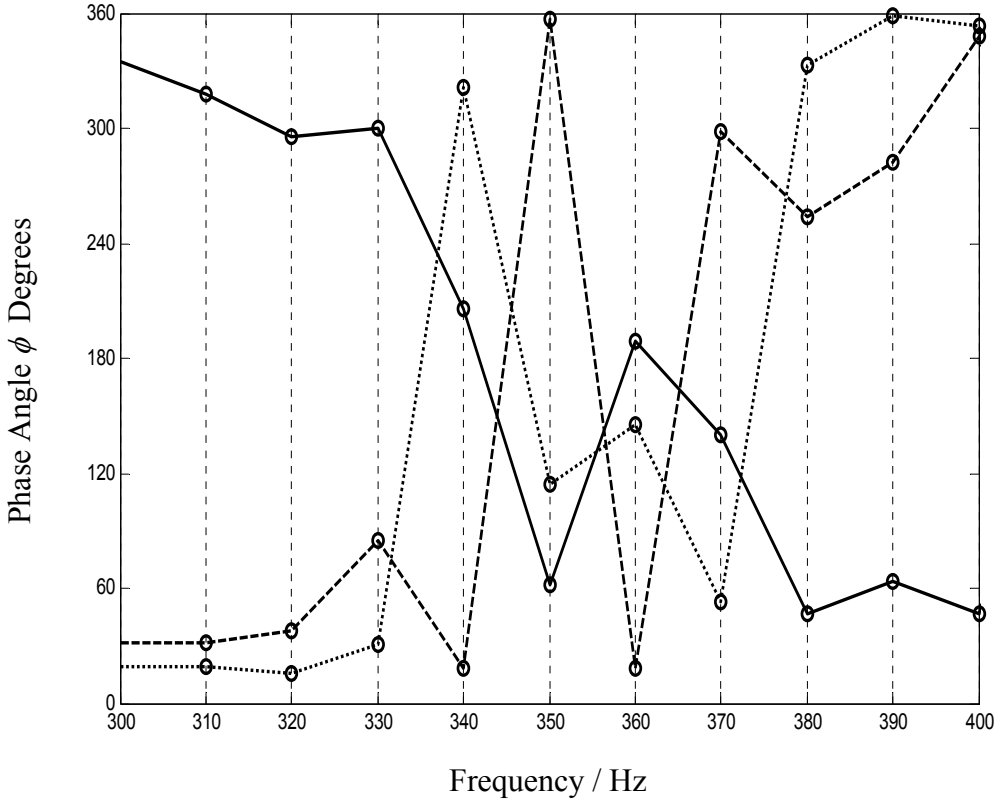

Figure 4.46. Comparison of the optimum synchrophase angles for ϕ_3 determined experimentally for the control machine at x_3, to achieve the minimum value of the cost function, when the magnitude of the drive voltage applied to each shaker is adjusted. A scaling factor λ_n is used to denote the magnitude of the n^{th} control source drive voltage with respect to the reference source.

The solid curve: $\lambda_2 = 1$ and $\lambda_3 = 1$.
The dotted curve: $\lambda_2 = 2/3$ and $\lambda_3 = 1/3$.
The dashed curve: $\lambda_2 = 1/3$ and $\lambda_3 = 2/3$.

The positions of the shakers were $x_1/l = 0.375$ (phase reference), $x_2/l = 0.21$ and $x_3/l = 0.71$.

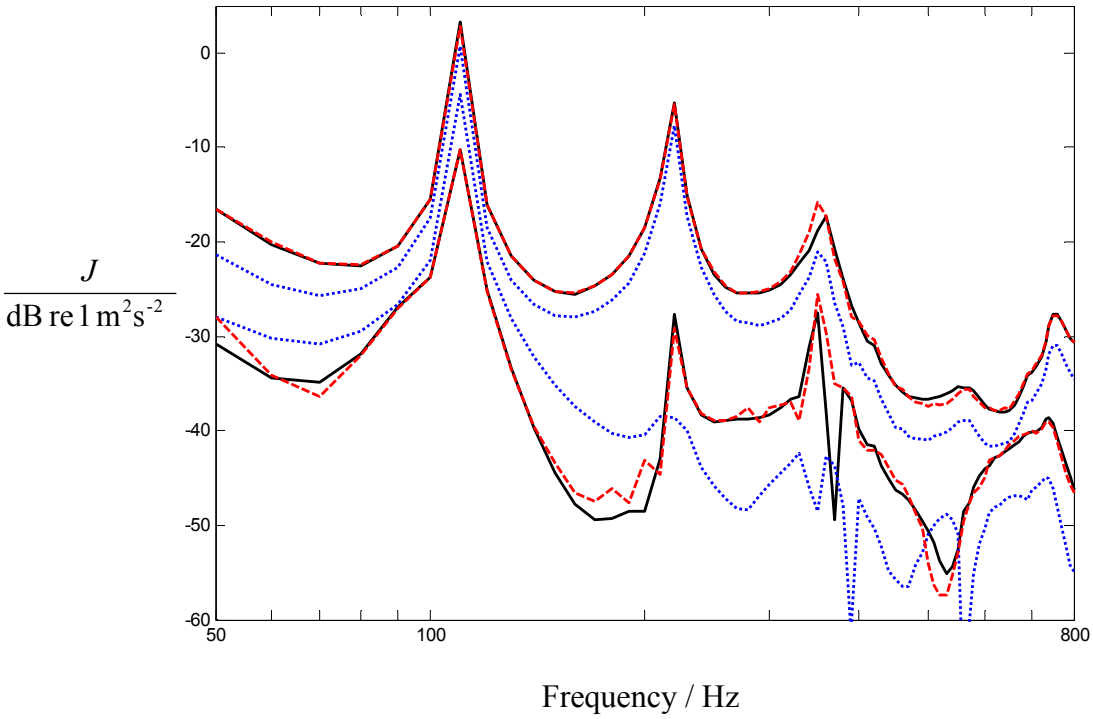

Figure 4.47. The maximum and minimum of the cost function obtained experimentally by synchrophasing when the magnitude of the drive voltage applied to each shaker is adjusted. A scaling factor λ_n is used to denote the magnitude of the n^{th} control source drive voltage with respect to the reference source.

The solid black curves $\lambda_2 = 1$ and $\lambda_3 = 1$.
The dotted blue curves $\lambda_2 = 1/3$ and $\lambda_3 = 2/3$.
The dashed red curves $\lambda_2 = 1/3$ and $\lambda_3 = 2/3$ corrected to simulate $\lambda_2 = 1$ and $\lambda_3 = 1$ by using $\delta_2 = 3$ and $\delta_3 = 3/2$.

The positions of the shakers were $x_1/l = 0.375$ (phase reference), $x_2/l = 0.21$ and $x_3/l = 0.71$.

This page is intentionally left blank

5 Summary and Conclusions

5.1 Summary

Synchrophasing has been investigated as an active vibration control technique for controlling the vibration of a large flexible machinery raft. This type of structure is commonly found on ships, and is used to provide a degree of isolation between the vibrating machinery and the ship's hull. The techniques developed could also be applied to any generalised flexible structure on which vibrating sources are mounted.

Synchrophasing differs from other methods of active vibration control in that no additional vibration sources are added to the structure for synchrophasing. All of the control is achieved by adjusting the phases of the source excitations that are applied to the structure, the magnitudes of the forces are not changed. With AC powered machinery such as pumps, which are commonly found on ship's machinery rafts, this means adjusting the phase of the voltage that is applied to each machine. Other methods of active vibration control commonly use actuators in order to apply additional forces to the structure to achieve an overall reduction. Although the use of actuators can provide a higher degree of active vibration control, because both the magnitude and phase of the additional forces can be adjusted, the system costs and space requirements of fitting additional components can make active vibration control much more costly, and has previously meant that active vibration control is sometimes dropped from the final ship machinery raft build.

Two models of a generalised one dimensional elastic structure have been developed. The first was a receptance based analytical model, and the second was a laboratory scale physical model of a one dimensional thin flexible beam supporting vibrating sources. It was decided to use a receptance based approach to the theoretical modelling because this approach is well established for studying mechanical systems consisting of lumped and distributed parameter components. Receptance techniques can also be used in a physical implementation of synchrophasing, because the point and transfer receptances of the vibrating machinery can be measured experimentally, without requiring detailed

knowledge of the mode shapes of the supporting structure. The analytical model can be used to determine the displacement at any point on the generalised structure caused by vibration due to machinery unbalance forces acting upon the structure, and can be used to investigate synchrophasing. Expressions for the displacement due to multiple vibrating sources were derived and introduced.

The receptance based analytical model was also used to guide the design and development of a physical laboratory model to ensure that each rigid body mode and flexural mode was separated in frequency, so that the vibration control achieved could be quantified for each mode. The analytical model was also used in simulations to ensure that sufficient flexural modes could be excited within the limitations of the experimental equipment available. It was decided that three flexural modes would be sufficiently representative of the most problematic vibrations of a real machinery raft and that the physical model should be constructed so that the first three flexural modes occurred at frequencies under 1 kHz.

The laboratory scale physical model was used to validate the predictions of the theoretical model and to understand the practical requirements of implementing a synchrophasing system onto an existing machinery raft. A PC driven data acquisition and analysis unit was used as the feed forward controller, providing the phase shifted signals to the shakers and processing the sensor signals from the accelerometers on the structure. Software was written in LABVIEW® to generate the phase shifted signals and to collect and analyse the accelerometer signals. Software was also written in MATLAB® to find the minimum of the cost function.

Both models were used as tools to analyse the interactions between the multiple vibrating harmonic sources when they are mounted on a common elastic structure and acting at the same frequency.

Two cost functions were investigated theoretically and experimentally. These were a global control cost function achieved by calculating the total time averaged kinetic

energy in the support structure and a local control cost function achieved by calculating the sum of the magnitude squared of the velocity over each mount point. For global control, the vibration at any point on the structure is regarded as equally important, where as for local control, only certain points on the structure are considered to be important. Mounting points where the machinery raft attaches to the rest of the ships superstructure are important paths for vibration control because vibration can be transmitted from the machinery raft into the superstructure and then radiate into the water.

The best cost function to use depends upon the frequency of excitation and the positions of the machinery upon the supporting raft, with respect to the nodes of the dominant modes of the machinery raft that are excited at the frequency of interest. Global control requires knowledge of the transfer mobilities between the machinery and the mass distribution of the machinery and the supporting structure. Local control only requires vibration at the mount points of the supporting structure to be measured, and so is more suitable to implement and retro-fit onto an existing machinery raft.

Two methods of finding the minimum of a cost function surface have been investigated theoretically and experimentally. The simplest method is a full incremental search, which consisted of changing the phase of each control source in turn from 0° to 360° in suitable steps. This gave a cost function surface for each operating frequency of interest. The minimum of the cost function surface was then found using MATLAB® to analyse the complete data set. The laboratory synchrophase system showed that this type of searching can be very time consuming, as it is necessary to adjust the phase of one control machine, let the vibration settle to its steady state, then calculate the cost function, repeating this process over a range of phase angles. A simple laboratory synchrophasing system consisting of three vibrating sources - one reference source and two control sources - took approximately three hours to perform a full search at a single frequency using a 10° step size.

As an alternative to a full search, the models were used to investigate the application of Propeller Signature Theory in finding the minimum of the cost function. This technique was originally developed for minimising the effects of aircraft propeller noise inside the cabin of the aircraft. Since then it has been successfully used to minimise the vibration inside the cabin of an aircraft. However, this thesis contains the first known work reported using Propeller Signature Theory to determine the signature between vibrating machinery mounted on a thin elastic raft and error sensors placed on the raft, with the aim of minimising a cost function by synchrophasing, based upon the machinery signatures and the modes of the raft structure. Propeller Signature Theory is used to calculate the phase independent transfer function or signature between each machine and each error sensor. A fully determined calculation of the transfer functions on a system comprising P control machines and one reference machine requires (P+1) physical measurements at independent phase angles, i.e. the same number of phase changes as there are control sources. Once the phase independent transfer functions are obtained, they can be used in simulations using a full search to calculate the minimum of a cost function surface and hence find the optimum synchrophase angles for the control machines.

A simple laboratory synchrophasing system consisting of three vibrating sources, one reference source and two control sources, using the method developed from Propeller Signature Theory took approximately one hour to determine the minimum of the cost function at 78 frequencies using a 1° phase angle step size. This was considerably faster than using a full search, because only three measurements on each accelerometer were required at each frequency, and it is the physical process of changing the phase angle of the applied voltage, allowing a settling time and making the measurement that takes the time.

A method for automating the calculation of the cost function in response to changes in the phase angles of the applied voltages was described and implemented in LABVIEW® and MATLAB® for both the full search method and the determination of the transfer functions by using Propeller Signature Theory. The models showed theoretically and

experimentally that the techniques developed for Propeller Signature Theory can successfully be applied for structural vibration control of a flexible machinery raft and are considerably faster than implementing a physical full search and would be more suitable as a form of close to real time adaptive vibration control.

The transfer function values determined using Propeller Signature Theory are not transfer mobilities as they do not calculate the forces applied by each vibration source. Hence if the load or speed of any machine were to change, it may be necessary to re-determine the transfer functions, because the optimum phase angles for minimising the cost function using synchrophasing could change if the applied forces change. The physical model was used to show that if the magnitudes of the applied forces change by a known amount then the transfer functions can be adapted to find the optimum synchrophase angles at the new vibration levels without requiring re-calculation of the transfer functions. However this may not be practical on a real machinery installation as a change in vibration measured locally on a machine may not be proportional to a change in the force applied to the machinery raft.

5.2 Conclusions

This work has shown that synchrophasing can successfully be applied as an active structural vibration control technique for reducing the vibration of a large thin elastic structure such as a machinery raft of the type commonly found on ships. The optimum synchrophase angles, and the amount of control achieved, depend upon the positions of the vibrating sources on the structure and also on the relative magnitudes of the forces that result from the vibration. Of particular importance to ship-borne machinery is the control of any rigid-body modes and the first flexural mode because the main vibrations generated by rotating and reciprocating machinery often lies in this frequency region. It has been shown that the position of the node of the rotational rigid body mode depends upon the positions of the machinery upon the flexible structure.

A one-dimensional receptance based analytical model was developed in order to understand synchrophasing and to guide the development of a laboratory scale physical

model and synchrophasing system. The receptance based model proved to be very successful at predicting the natural frequencies of the two rigid body modes and the first two flexural modes of the laboratory model which were well separated and could always be recognised. Higher order flexural modes were harder to recognise and there was an increasing difference between the theoretical predictions and the physical model. Analysis of the physical laboratory model in vibration showed that the beam twisted when excited at some frequencies above the second flexural mode. Torsional and flexural modes across the width of the beam are not included in the one-dimensional Euler-Bernoulli based receptance model. The receptance based model proved to be very useful in understanding the operational deflection shapes obtained from the physical model and why control was not achieved at certain frequencies and positions of the shakers on the beam.

The analytical model and the laboratory physical synchrophasing system were used to test and compare two different cost functions and two methods of searching for the optimum synchrophase angles necessary to minimise the cost functions. It was shown that local control and global control could both be achieved using synchrophasing and that the most effective method of control depended upon the frequency of excitation and the positions of the shakers upon the beam. Techniques developed in Propeller Signature Theory to determine a phase independent transfer function between each vibrating source and each sensor, enabled much faster calculation of the optimum synchrophase angles for each machine, than the simpler method of incrementally stepping through all combinations of angles.

It was shown analytically that when only two vibrating sources are mounted on the thin beam, then a simple analytical expression can be obtained for the optimum synchrophase angle of the single control source. This angle is often just either in phase or in anti-phase with the reference source. Experimental studies and simulations confirmed that the optimum synchrophasing angle to minimise the cost function depended upon the positions of the vibrating sources on the structure, the positions of

the nodes of the main modes of vibration that are excited at the frequency of interest and the magnitude of the modal forces.

It was shown analytically that when more than two vibrating sources are mounted on the flexible structure, so that there is more than one control source (one reference and P control sources), then interaction terms exist between the control shakers, so that no simple analytical expression for the optimum synchrophase angle for each control source could be found. The effect of these interaction terms are that they can work against each other, the result being that synchrophasing may not be as effective and that local minima of the cost function surface can exist. This highlighted the requirement to perform a search over the whole cost function surface, i.e. over the whole phase range, to ensure that the global cost function minimum is found, hence the best synchrophase angles.

5.3 Recommendations for further research

This research has used simulations where a normal force has been applied to the thin elastic beam. Although a reciprocating machine would be expected to apply normal forces to the supporting structure, rotating machinery would also be likely to apply a torsional moment. To accommodate this, it could be necessary to use a beam theory other than Euler-Bernoulli, such as Timoshenko thick beam theory, when modelling more complex situations where the effects of rotary inertia and shear deformation need to be considered. Controlling and adjusting the phase of the voltage supplied to a laboratory shaker is far simpler than adjusting the phase of the voltage applied to an industrial machine, where larger currents are involved. Follow on work to investigate how the phase could be changed practically on a real machinery installation would be a good next step to further investigate the practicalities and usefulness of synchrophasing.

It is likely that more than one frequency will be generated by the vibrating machine. This is particularly troublesome in a military marine environment where the detection of several ‘tonals’ from ship or submarine machinery can be used to identify the vessel to potential attackers. Further work could be conducted into controlling a cost function

based upon more than one frequency. For example, minimising the magnitude of the velocity squared at each mount point at 50 Hz, 100 Hz, 150 Hz and 200 Hz simultaneously.

A real machinery raft installation on a ship or submarine will have some mounting points situated on or close to the hull and other mounting points situated away from the hull. Previous research has indicated that mounting points that connect directly to the external hull will create larger contributions to the overall radiated noise signature of the vessel and so it is more important to control the vibration at these points. An extension to the work conducted so far would be to weight the magnitude of the velocity squared at each mount point based upon its position on the structure. In this way, the most important points on the structure to be controlled can be given addition weighting or importance on the generation of the cost function surface.

List of symbols used

β_n n^{th} flexural wave number.

ΔM_p A proportion of the mass of machinery which is added to each mass element.

$\mathbf{\Gamma}$ Transfer function matrix relating the out of balance forces applied to the elastic mounting structure by each machine to the velocity at each cost function sensor.

η Proportional damping factor.

θ_n Phase of the complex quantity obtained from a vector multiplication of the form $\mathbf{y}_n^H \mathbf{y}_p$ where $n = 1 \cdots 3$.

λ_n Scalar factor relating the magnitude of the force applied to the structure by the n^{th} control machine to the magnitude of the force applied by the reference phase machine.

$\mathbf{\Lambda}$ Diagonal matrix of scalar factors of the form λ_n.

ρ Density, mass density.

ϕ_n Phase of the force applied to the structure by the n^{th} control machine with respect to the phase of the reference machine.

$\boldsymbol{\varphi}$ Vector of phases of the force applied to the structure by the reference machine and the n control machines.

ψ_n A known phase shift applied to a machine, when determining the transfer function matrix.

$\mathbf{\Psi}$ The matrix of known phase shifts, applied to the machines when determining the transfer function matrix.

ω Angular frequency of oscillation.

ω_n n^{th} natural frequency of oscillation of a structure.

A Cross sectional area of the structure.

E Energy of a structure.

E_y Youngs modulus.

f_r Force applied to the structure due to the reference phase machine.

$\mathbf{f}_c$ Vector of forces applied to the structure due to the control machines.

I Second moment of area of the structure cross section about the neutral axis.

J Cost function based upon calculating the sum of the magnitude squared of the velocities over sensor positions.

k Stiffness of support mounts.

L Length of the structure.

m_n n^{th} mass element of the structure.

$m_{m,n}$ n^{th} modal mass.

$\mathbf{M}$ Diagonal matrix containing the mass of each element on the leading diagonal.

$\mathbf{M_m}$ Matrix of modal masses.

N Number of modes considered in modal summation equations.

N_m Number of mass elements.

P Number of machines used to achieve control.

$\mathbf{q}_r$ Vector of modal receptances.

$\mathbf{Q}_c$ Matrix of modal receptances.

R_n Magnitude of the complex quantity obtained from a vector multiplication of the form $\mathbf{y}_n^H \mathbf{y}_p$ where $n = 1 \cdots 3$.

S Number of sensors used determining the cost function.

T Kinetic Energy.

U Elastic strain energy.

w Displacement.

$\dot{\mathbf{w}}$ Vector of velocities at the sensor positions on the structure.

$\dot{w}_s$ Velocity at sensor s.

W_n n^{th} mode shape of the beam.

$\dot{\mathbf{W}}$ A matrix of velocities, the columns of which correspond to the velocities measured for each particular known phase shift. Used in determining the transfer function matrix.

x_n The position of the n^{th} machine on the structure.

$Y_{i,r}$ Transfer mobility between the reference machine and the i^{th} mass element.

$y_{s,p}$ Transfer mobility between the s^{th} sensor and the p^{th} machine.

$\mathbf{y}_n$ Vector of transfer mobilities between the n^{th} control machine (or the reference machine if $n = r$) and each of the mass elements/sensors.

$\mathbf{Y}$ Matrix of transfer mobilities between each of the machines and each of the cost function sensors.

$\mathbf{Y}_c$ Matrix of transfer mobilities between the control machines and each of the mass elements/sensors.

List of operations

$\langle \Im \rangle_t$ Time averaged value of $\Im$

$\dot{\Im}$ Time derivative of $\Im$ given by $\frac{d\Im}{dt}$

$\Im^H$ Hermitian (conjugate transpose) of matrix $\Im$

Re($\Im$) Real part of complex number $\Im$

Im($\Im$) Imaginary part of complex number $\Im$

$\Im^*$ The complex conjugate of $\Im$

List of references

1. RAO, S.S. Mechanical Vibrations (Fourth Edition), Prentice Hall, 2004.

2. DEN HARTOG, J.P. Mechanical Vibrations, McGraw-Hill Book Company Inc., 1956.

3. HARRIS, C.M. and CREDE, C.E. Shock and Vibration Handbook, Mc-Graw-Hill, 1996.

4. ROSS, D. Mechanics of Underwater Noise, Pergamon Press Inc., 1976.

5. KINNS, R. Some Observations on the achievable properties of Diesel Isolation Systems. *Proceedings of the 2nd International Symposium on Shipboard Acoustics ISSA '86 The Hague, Netherlands*, 1986.

6. SWINBANKS, M.A. Some elementary principles of distributed isolation systems and their relevance to raft mounting, June 1976, *Y-ARD Memorandum No. YM/2561/76.*

7. SWINBANKS, M.A. Measurement and analysis of vibration in ship installations of medium speed diesel engines mounted on very flexible vibration isolators (Part 2), 1977, *Y-ARD Report Number Y-ARD/2365/77.*

8. STREDULINSKY, D.C. Isolation of Structure-Borne Sound from Ship Machinery: A Literature review and possibilities for finite element modelling, May 1991, *DREA Technical Memorandum 91/208.*

9. SNOWDON, J.C. Isolation of Machinery Vibration from Nonrigid Substructures Using Multiple Antivibration Mountings. *Transactions of the American Society of Mechanical Engineers*, 1973, AMD Volume 1, 102-127.

10. STEENHOEK, H.F. On Characterising Structure-Borne Sound Transmission Paths from Resiliently Mounted Ship Machinery. 1990, Proceedings of the 2nd Undersea Defence Technology Conference, London, UK.

11. NORFIELD, D. Practical Balancing of Rotating Machinery, Elsevier, 2006.

12. LEE, K.H., LEE, S.M., and BAE, J.G. Vibration Reduction of Diesel Generator Set by Structure Modification. *Proceedings of the Twelfth international Congress on Sound and Vibration, Lisbon, Portugal*, 2005.

13. ORMONDROYD, J. and DEN HARTOG, J.P. The Theory of the Dynamic Vibration Absorber. *Transactions of the American Society of Mechanical Engineers*, 1928, 49, (APM-50-7), 9-22.

14. DAYOU, J. and KIM, S.M. Control of kinetic energy of a one dimensional structure using multiple vibration neutralizers. *J. Sound and Vibration*, 2005, 281, 323-340.

15. BRENNAN, M.J. and DAYOU, J. Global control of vibration using a tunable vibration neutralizer. *J. Sound and Vibration*, 2000, 232, (3), 585-600.

16. FULLER, C.R., MAILLARD, J.P., MERCADEL, M., and VON FLOTOW, A.H. Control of aircraft interior noise using globally de-tuned vibration absorbers. *J. Sound and Vibration*, 1997, 203, 745-761.

17. ZHUANG LI and CROCKER, M.J. A Review on Vibration Damping in Sandwich Composite Structures. *International Journal of Acoustics and Vibration*, 2005, 10, (4), 159-169.

18. RAYLEIGH STRUTT, J.W., Chapter XIV General Equations, *In*: *Theory of Sound*. Macmillan and Co, 1878, 104-106.

19. LUEG, P. *Process of Silencing Sound Oscillations*, Patent: 2,043,416, 9 June 1936.

20. FULLER, C.R., NELSON, P.A., and ELLIOTT, S.J. Active Control of Vibration, Academic Press Ltd, 1997.

21. OLSON, H.F. and MAY, E.G. The Electronic Sound Absorber. *J. Acoust. Soc. Am.*, 1953, 25, (6), 1130-1136.

22. BALAS, M.J. Active control of flexible systems. *J. Optimization Theory Appl.*, 1978, 25, 415-436.

23. MEIROVITCH, L. and BENNIGHOF, J.K. Modal control of travelling waves in flexible structures. *J. Sound and Vibration*, 1986, 111, (1), 131-144.

24. MEIROVITCH, L., BARUH, H., and OZ, H. A comparison of control techniques for large flexible systems. *J. Guidance, Control and Dynamics*, 1983, 6, (4), 302-310.

25. MEIROVITCH, L. Some problems associated with the control of distributed structures. *J. Optimization Theory and Applications*, 1987, 54, (1), 1-21.

26. BAZ, A. and POH, S. Performance of an active control system with piezoelectric actuators. *J. Sound and Vibration*, 1988, 126, (2), 327-343.

27. CZAJKOWSKI, E.A., PREUMONT, A., and HAFTKS, R.T. Spillover stabilization of large space structures. *J. Guidance, Control and Dynamics*, 1990, 13, (6), 1000-1007.

28. HOWARD, C. Experimental Results of Synchrophasing two axial fans in a duct. September 2004, Proc. Active 04 Conference, Williamsburg, Virginia, Paper A04_29.

29. RISI, J.D., BURDISSO, A., and FULLER, C.R. Analytical investigation of active control of radiated inlet fan noise. *J. Acoust. Soc. Am.*, 1996, 99, (1), 408-416.

30. KIM, I.S., NA, H.S., KIM, K.J., and PARK, Y. Constrain filtered-x and filtered-u least-mean-square algorithms for the active control of noise in ducts. *J. Acoust. Soc. Am*, 1994, 95, (6), 3379-3389.

31. JENKINS, M.D. Active Control of periodic machinery vibrations. PhD thesis, University of Southampton, UK, 1989.

32. WANG, D. and HUANG, Y. Modal space vibration control of a beam by using feedforward and feedback control loops. *International Journal of Mechanical Sciences*, 2002, 44, 1-19.

33. HOWARD, C. Active Isolation of Machinery vibration from Flexible Structures. PhD Thesis, University of Adelaide, April 1999.

34. BAILEY, T. and HUBBARD, J.E. Distributed piezoelectric-polymer active vibration control of a cantilever beam. *J. Guidance, Control and Dynamics*, 1985, 8, (5), 605-611.

35. CLARK, R.L. and FULLER, C.R. Optimal placement of piezoelectric actuators and polyvinylidene fluoride error sensors in active structural acoustic control approaches. *J. Acoust. Soc. Am.*, 1992, 92, (3), 1521-1533.

36. YOUNG, A.J. Active Control of Vibration in Stiffened structures. PhD Thesis, The University of Adelaide, August 1995.

37. COX, D.E. and LINDNER, D.K. Active control for vibration suppression in a flexible beam using a modal domain optical fiber sensor. *J. Vibration and Acoustics*, 1991, 113, 369-382.

38. GAUDENZI, P., CARBONARO, R., and BENZI, E. Control of beam vibrations by means of piezoelectric devices: theory and experiments. *J. Composite Structures*, 2000, 50, 373-379.

39. GIBBS, G.P. and FULLER, C.R. Excitation of thin beams using asymmetric piezoelectric actuators. *J. Acoust. Soc. Am.*, 1992, 92, (6), 3221-3227.

40. YOUNG, A.J. and HANSEN, C.H. Control of Flexural Vibration in Stiffened Structures Using Multiple Piezoceramic Actuators. *Applied acoustics*, 1996, 49, (1), 17-48.

41. MOSHREFI-TORBATI, M., KEANE, A.J., ELLIOTT, S.J., BRENNAN, M.J., ANTHONY, D.K., and ROGERS, E. Active Vibration control (AVC) of a satellite boom structure using optimally positioned stacked piezoelectric actuators. *J. Sound and Vibration*, 2006, 292, 203-220.

42. BRENNAN, M.J., ELLIOTT, S.J., and PINNINGTON, R.J. Strategies for the active control of flexural vibration on a beam. *J. Sound and Vibration*, 1995, 186, (4), 657-688.

43. HALKYARD, C.R., MACE, and B.R. Feedforward adaptive control of flexural vibration in a beam using wave amplitudes. *J. Sound and Vibration*, 2002, 254, (1), 117-141.

44. PINES, D.J. and VON FLOTOW, A.H. Active control of bending wave propagation at acoustic frequencies. *J. Sound and Vibration*, 1990, 142, 391-412.

45. LEE, J.T. Active structural acoustics control of beams using active constrained layer damping through loss factor maximization. *J. Sound and Vibration*, 2005, 287, 481-503.

46. ROCKWELL, T.H. and LAWTHER, J.M. Theoretical and experimental results on active vibration dampers. *J. Acoust. Soc. Am.*, 1964, 36, (8), 1507-1515.

47. ELLIOTT, S.J., JOSEPH, P., NELSON, P.A., and JOHNSON, M.E. Power output minimization and power absorption in the active control of sound. *J. Acoust. Soc. Am.*, 1991, 90, (5), 1453-1459.

48. PAVIC, G. Vibration damping, energy and energy flow in rods and beams: governing formulae and semi-infinite systems. *J. Sound and Vibration*, 2006, 291, (3-5), 932-962.

49. NELSON, P.A. and ELLIOTT, S.J. Active Control of Sound, Academic Press, 1992.

50. MALLOCK, A. A Method of preventing Vibration in Certain Classes of Steamships. *Trans. Inst. Naval Architects*, 1905, 47, 227-230.

51. KALIN, A. *Synchrophasing System*, Patent: US2205265, 18 June 1940.

52. HARADA, I. *Blower noise reducing method by phase control*, Patent: JP54060656, 1977.

53. FULLER, C.R. Analytical Investigation of Synchrophasing as a means of reducing aircraft interior noise, August 1984, *NASA Contractor Report 3823.*

54. JONES, J.D. and FULLER, C.R. Noise Control Characteristics of Synchrophasing - An Experimental Investigation. October 1984, AIAA/NASA 9th Aeroacoustics Conference, Williamsburg, Virginia. Paper Number: AIAA-84-2370.

55. FULLER, C.R. Noise Control Characteristics of Synchrophasing - An Analytical Investigation. October 1984, AIAA/NASA 9th Aeroacoustics Conference, Williamsburg, Virginia. Paper Number: AIAA-84-2369.

56. FULLER, C.R. Analytical model for investigation of interior noise characteristics in aircraft with multiple propellers including synchrophasing. *J. Sound and Vibration*, 1986, 109, (1), 141-156.

57. BLUNT, D.M. and REBBECHI, B. An Investigation into Active Synchrophasing for cabin noise and vibration reduction in propeller aircraft. September 2006, Proc. Active 2006, Adelaide, Australia. Paper 87.

58. BLUNT, D.M. and REBBECHI, B. Propeller Synchrophase Angle Optimisation Study. May 2007, 13th AIAA/CEA Aeroacoustics Conference. Rome, Italy. Paper Number AIAA-2007-3584.

59. MAGLIOZZI, B. *Adaptive Synchrophaser For Reducing Aircraft Cabin Noise and Vibration*, Patent: United States Patent 5,453,943, 26 September 1995.

60. JOHNSTON, J.F., DONHAM, R.E., and GUINN, W.A. Propeller signatures and their use. *AIAA Journal of Aircraft*, 1981, 18, (11), 934-942.

61. PLA, F.G. and GOODMAN, G.C. *Method and apparatus for synchronizing rotating machinery to reduce noise*, Patent: United States Patent 5,221,185, 22 June 1993.

62. PLA, F.G. *Method for reducing noise and/or vibration from multiple rotating machines*, Patent: United States Patent 5,789,678, 4 August 1998.

63. GARDONIO, P. and BRENNAN, M.J. On the origins and development of mobility and impedance methods in structural dynamics. *J. Sound and Vibration*, 2002, 249 (3), 557-573.

64. DALEY, S., JOHNSON, F.A., PEARSON, J.B., and DIXON, R. Active Vibration Control for marine applications. *Control Engineering Practice*, 2004, 12, 465-474.

65. WARBURTON, G.B. The Dynamical Behaviour of Structures (2nd Edition), Pergamon Press Ltd, 1976.

66. BISHOP, R.E.D., GLADWELL, G.M.L., and MICHAELSON, S. The Matrix Analysis of Vibration, Cambridge University Press, 1965.

67. DENCH, M.R., BRENNAN, M.J., and FERGUSON, N.S. Active Control of the Flexural Vibration of a thin beam with free ends, July 2005, *ISVR Technical Memorandum No: 949*. University of Southampton, UK.

68. DENCH, M.R., BRENNAN, M.J., and FERGUSON, N.S. Rigid body modes and their role in the active minimisation of the kinetic energy of a free-free beam. *IX International Conference on Recent Advances in Structural Dynamics,* 2006. Southampton, UK.

69. EWINS, D.J. Modal Testing theory, practise and application. Research Studies Press Ltd, 2000.

70. TYNE, J.R. Simple Bending, Chatto & Windus Ltd, 1974.

71. MAGLIOZZI, B. Synchrophasing for cabin noise reduction of propeller-driven airplanes. 1983, 8th AIAA Aeroacoustics Conference Paper AIAA 83-0717.

72. JONES, J.D. and FULLER, C.R. Noise Control Characteristics of Synchrophasing, Part 2: Experimental Investigation. *AIAA Journal,* 1986, 24 (8), 1271- 1276.

73. LING DYNAMIC SYSTEMS V100 Series Vibrators Installation and Operating Manual, January 1995, *Manual Number 899061, Edition 2, Amendment no. 14.*

74. DUNCAN, W.J. The admittance method for obtaining the natural frequencies of systems. *Philosophical Magazine*, 1941, 32, (7), 401-409.

This page is intentionally left blank